Order Number 9109294

Λ^0 and $\bar{\Lambda}^0$ production in $p\bar{p}$ collisions at $\sqrt{s} = 1.8$ TeV

Wesson, Dennis Keith, Ph.D.

Duke University, 1990

U·M·I
300 N. Zeeb Rd.
Ann Arbor, MI 48106

Λ^0 AND $\bar{\Lambda}^0$ PRODUCTION IN $p\bar{p}$ COLLISIONS AT $\sqrt{s}$ =1.8 TeV

by

Dennis Keith Wesson

Department of Physics
Duke University

Date: February 15, 1990

Approved:

Seog H. Oh, Supervisor

Dissertation submitted in partial fulfillment of
the requirements for the degree of Doctor
of Philosophy in the Department of
Physics in the Graduate School
of Duke University

1990

ABSTRACT

(Physics-High Energy)

Λ^0 AND $\bar{\Lambda}^0$ PRODUCTION IN $p\bar{p}$
COLLISIONS AT $\sqrt{s}$ =1.8 TeV

by

Dennis Keith Wesson

Department of Physics
Duke University

Date: February 13, 1990

Approved:

Seog H. Oh, Supervisor

An abstract of a dissertation submitted in partial fulfillment of the requirements for the degree of doctor of philosophy in the Department of Physics in the Graduate School of Duke University

1990

Abstract

The characteristics of Λ and $\bar{\Lambda}$ production have been studied from data obtained from $p\bar{p}$ collisions at $\sqrt{s}$ =1.8 TeV during the first running period of experiment E735 from January to May of 1987. The experiment was conducted at the Fermi National Laboratory Tevatron collider. Five million triggers from an integrated luminosity of about $\frac{1}{3}$ nb^{-1} were written to tape during this initial run of E735. Using a magnetic spectrometer arm a sample of 413 Λ's + $\bar{\Lambda}$'s were found in these events.

The transverse momentum spectrum, the ratio Λ/(all charged particles) and the ratio Λ/proton were studied from this sample. These were compared to the findings at lower energies and also to the results of a Monte Carlo program from another experiment. The average transverse momentum was found to be $0.77 \pm 0.06 \pm 0.08$, an increase of about 24% from the value found at $\sqrt{s}$ =540 GeV (CERN SPS) and an increase of about 55% from $\sqrt{s}$ =53 GeV (CERN ISR). The Λ/(all charged particle) ratio was also found to increase from 0.009 ± 0.001 at $\sqrt{s}$ =53 GeV (CERN ISR) and 0.019 ± 0.004 at $\sqrt{s}$ =540 GeV (CERN SPS), to $0.026 \pm 0.002 \pm 0.004$ at our energy of $\sqrt{s}$ =1.8 TeV. The lambda/proton ratio was found to be $0.38 \pm 0.03 \pm 0.06$. This ratio shows no increase from lower energies. The lambda/proton ratio was used to find the strangeness suppression factor (λ) from the quark combinatoric model of hadron production. We obtain a value λ=0.34 ± 0.05 in agreement with the values found at lower energies.

The increase in the ratio lambda/all charged particles as a function of center of

mass energy is not inconsistent with the formation of quark-gluon plasma. However, the constant ratio of lambda/proton production is not expected in quark-gluon plasma production. Moreover, our data seem to agree with the UA5 Monte Carlo data, which does not include quark-gluon plasma production. Based on Λ production at $\sqrt{s}$ =1.8 TeV, there is no compelling evidence of quark-gluon plasma production.

Acknowledgements

First, I would like to thank my thesis advisor, Seog Oh, who spent many hours reading and correcting this thesis. From him, I have learned much about the methods of high energy physics and I thank him for his patience and guidance during my time at Duke.

I would also like to thank my collaborators on E735 for their part in the preparation and running of the experiment. At Duke, I want to Al Goshaw and Bill Walker for their help. Special thanks go to Laszlo Gutay, Carlos Hojvat, Frank Turkot, Albert Erwin and Peter Beery.

There are many people in the physics department at Duke who deserve my thanks for making my time in graduate school both enjoyable and educational, although, for the sake of brevity, I won't mention everyone here. I would like to thank the graduate students in High Energy during my time at Duke: Elliot McCrory, Chuck Wild, Tim Turkington, Grace Mendez, Rick Tesarek, Qifeng Shen and Jay Cook. Tom Carter and Cal Loomis, who also worked on E735, deserve special thanks for their friendship, efforts on the experiment and assistance in the preparation of this thesis. Thanks to Pat Hoyt for her conversation and help. And thanks to Mark Godwin for putting up with the abuse he received from an older

graduate student.

Finally, I would like to thank my family. My sister, Melanie, who started my education when I was three years old, has been a major force in many areas of my life. Thank you, Melanie, for your support and confidence in me. Most of all, I would like to thank my parents. Without their love, support and encouragement nothing I have done in my life would have been possible.

Contents

List of Tables

List of Figures

Chapter 1

Introduction and Overview

Strange particles were first observed in cosmic ray studies in 1944 by L. Le Prince-Ringuet. Le Prince-Ringuet observed a delta ray produced by a secondary cosmic ray particle (Le Prince-Ringuet and Lheritier 1944). The mass of this particle was 500 ± 50 MeV/c^2. At the time, the interpretation of this single event was not clear; today, it is obvious that the particle was a kaon. Later, more convincing evidence of the existence of these new particles was found. In 1947, the decay of a neutral baryon heavier than the proton into two charged particles, the decay of a heavy neutral meson and the decay of a heavy charged meson were observed in cloud chambers and in emulsions.

Called "V-particles" at the time because of the shape of their decay, these strange baryons are now known as Λ's. By the early 1950's the existence of other strange baryons such as the sigma and the cascade or "double-V", also because

of its decay, had been established. Collectively this group of particles, heavier than the proton, came to be called hyperons.

The long lifetime of these particles when considered with their copious production was puzzling. It was this fact that led to their being called "strange" particles. This was explained by A. Pais through his theory of associated production, the idea that strange particles must be created in pairs. In 1953, this idea was confirmed with the first "artificially" made strange particles at Brookhaven National Laboratory. R. P. Shutt and his collaborators observed a Λ decay produced in a $\pi^- p$ collision (Fowler et al. 1953). Using the known beam momentum and conservation of energy, they were able to infer the mass of the missing neutral particle, which turned out to be a kaon.

This idea was formalized by Gell-Mann in 1953 (Gell-Mann 1953) and Nishijima (Nishijima 1955) with the introduction of the strangeness quantum number, S. In this picture, any particle with a non-zero strangeness quantum number is a strange particle. Also, the strangeness quantum number is conserved in all but weak interactions.

The baryon decay first observed in these cloud chambers was $\Lambda \rightarrow p\pi$, a weak decay with a branching ratio of 64.1%. Most of the remaining Λ decays proceed via $\Lambda \rightarrow n\pi$ (35.7%). Since its discovery, the Λ has been extensively studied. The Λ mass has since been established as 1.1156 GeV/c^2 and its lifetime as 2.63×10^{-10} sec.

It is generally accepted that at sufficiently high energy densities, hadronic matter undergoes a phase transition to a weakly interacting plasma composed of

deconfined quarks and gluons (Anishetty, Koehler and McLerran 1980; Domokos and Goldman 1981; McLerran and Svetitsky 1981). The plasma is expected to have a lifetime on the order of 10^{-23} seconds (Koch, Müller and Rafelski 1986), so it can only be identified by its decay products. One proposed signature for quark-gluon plasma production is an unusual abundance of strange particles such as the Λ (Rafelski and Müller 1982).

One design feature of E735 was to look for a deconfined quark-gluon plasma state of matter using the Tevatron $p\bar{p}$ collider at the Fermi National Accelerator Laboratory. E735 was an experiment located at the C0 intersection region of the collider. It consisted of a multiplicity hodoscope, a trigger hodoscope and a magnetic spectrometer arm (with charged particle tracking and time of flight measurement) at 90 degrees. This experiment looked in the central rapidity region for signatures of quark-gluon plasma formation.

In January 1987, the Tevatron $p\bar{p}$ collider at the Fermi National Accelerator Laboratory began its first physics run at a center of mass energy of 1.8 TeV, opening the TeV energy region to physics exploration for the first time in a laboratory setting. Experiments at three beam intersection regions around the accelerator took data during the collider's five months of high energy physics operation.

E735 took data during two running periods. The first was from January to May of 1987 and the second started in June of 1988 and ended in May of 1989. Analysis of data from the first running period is almost completed and the preliminary analysis of the data from the second run has started. The data from the second running period are expected to be much better in statistics, not only because this period

was over twice as long as the first running period, but also improvements in accelerator performance led to much higher luminosities for the second run.

In this thesis, we will study the production of Λ's as a possible signature of quark-gluon plasma formation. We will examine the average transverse momentum of Λ's, the ratio of Λ's to all charged particles and the ratio of Λ's to protons produced in $p\bar{p}$ collisions at a center of mass energy of 1.8 TeV. We will compare these to results from lower energy experiments and to results obtained from a Monte Carlo generator.

Document Organization

This dissertation is based on data from the first running period of experiment E735. It deals with the production of the strange particles Λ and $\bar{\Lambda}$ in $p\bar{p}$ collisions at $\sqrt{s}$ =1.8 TeV. Chapter 2 is a review of high energy physics. The ideas in the second chapter are presented as close to chronological order as possible. Some deviation from the true chronological order was required to avoid skipping from topic to topic. Chapter 2 is not only a continuation of the introduction, but also a review of some of the concepts used in the first section of chapter 3.

Chapter 3 deals with experiment E735. Since E735 is a search for quark-gluon plasma, the first section is a survey of the theory underlying the quark-gluon plasma, how it is thought to form, how it evolves with time, how it might be detected and, finally, how strangeness is produced in the plasma. The second section of the third chapter describes the many different components of the E735 detector. Penultimately, the third section contains a detailed discussion of the straw drift chambers which were built as part of the work for this thesis. The construction, testing and performance of these chambers will be described. Chapter 3 ends with a discussion of the data acquisition system and event triggers for E735.

The heart of this dissertation is in chapters 4 and 5. Chapter 4 examines the

offline analysis of the data for E735 and more specifically the method used to identify Λ's. First in chapter 4 the general methods use to reduce the data, reconstruct tracks and remove background are presented. Next the cuts used to increase the signal to noise ratio in the lambda invariant mass plots are described, and finally the technique used to generate the acceptance corrections for Λ's is presented. The results of this analysis are presented in chapter 5 and compared both with results at lower energy and with the results of a Monte Carlo event generator. The final chapter, chapter 6, will provide a summary of this dissertation.

Chapter 2

Review of Particle Physics Concepts

In order to understand the theory behind a search for a quark-gluon plasma, let us first undertake a review of the history and concepts of particle physics. In the following section, the discoveries leading up to the proposal of the quark model will be discussed. This will be followed by a discussion of the quark model itself. Then in the next section the deep inelastic scattering experiments from which the parton model emerged will be examined, leading to a section on the parton model. Next, a brief look at the theory of strong interactions will follow. Finally, the subject of weak interactions will close this chapter.

I. Isospin and Strangeness

Perhaps one of the first steps towards a quark model came in 1932 when Heisenberg suggested that the neutron and the proton might be different charge substates of the same particle called a nucleon. The neutron and the proton were assigned a quantum number, called isospin, with the value 1/2. The proton and the neutron differ in the third component of isospin, I_3 or I_z, with the proton being assigned the value +1/2 and the neutron -1/2. The charge of each is then given by the formula $Q/e=1/2+I_3$. Isospin is conserved in strong interactions.

In 1947 with the discovery of the pion (Lattes et al. 1947) (Perkins 1947) (Occhialini and Powell, 1947), the nucleon lost its unique role as the only particle to be involved in strong interactions. The pion, since it has three different charge states (π^+,π^0, π^-), was assigned an isospin value 1 with $I_3=+1$ for the π^+, $I_3=0$ for the π^0 and $I_3=-1$ for the π^-. The charge for the pion is then given by the formula $Q/e=I_3$. The two different formulae for the charge can be reconciled by assigning a new quantum number called baryon number (B). If the nucleon is assigned a baryon number of 1 and the pion a baryon number of 0, the formula for the charge becomes $Q/e=I_3+B/2$.

Also in 1947, G. D. Rochester and C. C. Butler (Rochester and Butler 1947) observed heavy unstable particles in cosmic ray interactions in cloud chambers. After operating for about a year at sea level, Rochester and Butler obtained two photographs of what were called, due to their appearance, "V-particles". After examining these events, it was determined that the "V" was the decay of a neutral particle formed in the interaction of a cosmic ray particle in the lead plate.

By the early 1950's, the existence of a group of "V-particles" heavier than the neutron or proton had been established. These particles were called hyperons. Also discovered about this time were "V-particles" with a mass between that of the proton and the pion, called kaons. Both types are unstable and are produced in strong interactions. The major difficulty presented by these particles was their long lifetime (10^{-8} to 10^{-10} sec) when considering their production in strong interactions. For this reason, these particles were called "strange".

In order to explain this behavior, A. Pais proposed the hypothesis of associated production (Pais 1952). According to this idea kaons and hyperons must be created and destroyed (via strong interactions) in pairs. Therefore the lightest hyperon would have to decay into a kaon and a proton for the process to be a strong decay. However, this is forbidden by the conservation of energy, since the sum of the masses of the proton and the kaon is greater than the mass of the lightest hyperon (the Λ).

In the isospin formalism, the Λ is an I=0 singlet state, because there are no charged counterparts to this particle. The Λ decays via

$$\Lambda \rightarrow p + \pi^-$$

I	0	1/2	1
I_3	0	1/2	-1

The lifetime of this decay is 2.63×10^{-10} seconds, which is much longer than the typical lifetime for strong or electromagnetic decays, and neither I nor I_3 is conserved, so this is a weak decay. For the isospin of the kaons, we first look at the production interaction:

$$\pi^- + p \rightarrow \Lambda + K^\circ.$$

I	1	1/2	0	I_{K°

So the kaon has half integral isospin with the simplest assignment being $I_K=1/2$. If the K° is assigned $I_3=-1/2$ then for this meson, $Q/e=I_3+1/2$. These two facts imply that the K° is a member of an isospin doublet with the $I_3=+1/2$ K^+. This also prohibits the decay:

$$K^+ \rightarrow \pi^+ + \pi^- + \pi^+$$

I	1/2	1	1	1
I_3	1/2	1	-1	1

except as a weak decay.

In this scheme for the assignment of isospin, the K^- is the antiparticle for the K^+. This implies a second uncharged kaon ($\overline{K}^\circ$), the antiparticle of the K°. There is now a second K-doublet consisting of the K^- and the $\overline{K}^\circ$. Unlike the K^+, K° doublet, for the K^-, $\overline{K}^\circ$ doublet the formula for the charge is $Q/e= I_3-1/2$.

Shortly after this in 1953, M. Gell-Mann (Gell-Mann 1953) and independently

Nishijima (Nishijima 1955), proposed the existence of an additive quantum number, called strangeness. This quantum number would be conserved in the strong production of these particles and in their electromagnetic interactions, but not in the weak decay. In this way the concept of associated production was formalized. Only pairs of particles with opposite strangeness can be produced in collisions involving nonstrange particles. Thus strangeness is conserved in production involving strong interactions and in electromagnetic interactions, but not in the decay of a strange particle to two or more nonstrange particles. Therefore, the decay would be inhibited as compared to the production of strange particles. This would account for their copious production and long lifetime.

With the addition of the strangeness quantum number, the formula for the charge can be generalized to $Q/e = S/2 + B/2 + I_3$. With this choice, the values of the strangeness quantum numbers are already determined. The Λ, a baryon (B=1) has S=-1, as do the K^- and the $\overline{K}^\circ$. The K^+ and the K° have S=+1. Of course, for particles like the proton and other nonstrange particles, the value of the strangeness quantum number is S=0.

II. SU(3) and the Quark Model

With the discovery of more and more "elementary" particles, attempts to find a pattern among them intensified. Grouping particles into isospin multiplets had been natural because of small mass differences between the members of a multiplet. The existence of another additive quantum number, strangeness, implied a larger symmetry group, one of rank two. However, no strange particle is close to the mass of the proton or neutron, so the next step in grouping particles was not as obvious.

In 1961, M. Gell-Mann (Gell-Mann 1962) and independently Ne'emann (Ne'emann 1961) proposed the symmetry group, SU(3), as the pattern among the many "elementary" particles. By grouping particles with the same baryon number, spin and parity, but allowing the strangeness to vary, different isospin multiplets can be grouped into the various SU(3) multiplets. Figure(2-1) shows the baryon octet of spin parity $1/2^+$.

Figure (2-2) shows the ($spin^{parity}$) $J^P=3/2^+$ SU(3) decuplet. At this time only nine members of the this decuplet were known. The tenth member was predicted by SU(3) to have baryon number=1, $J^P=3/2^+$, S=-3, I=0, I_3=0, Q=-1 and a mass of

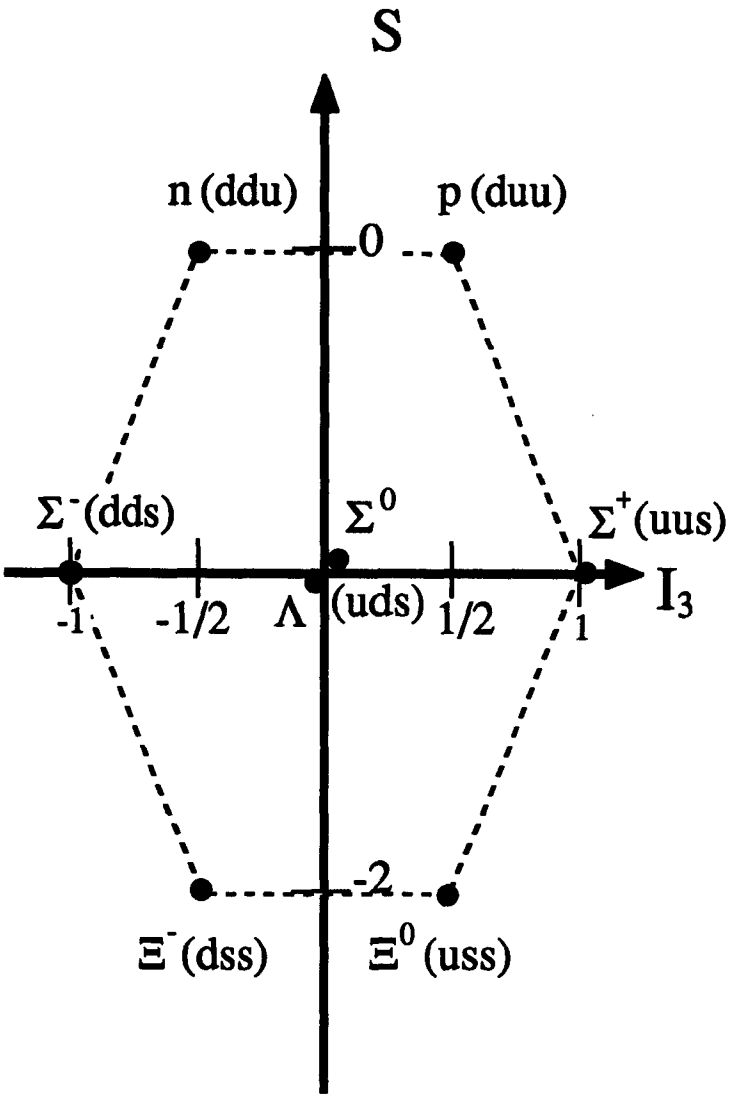

Figure 2-1. Baryon octet with $J^P=1/2^+$ plotted in the I_3-S plane.

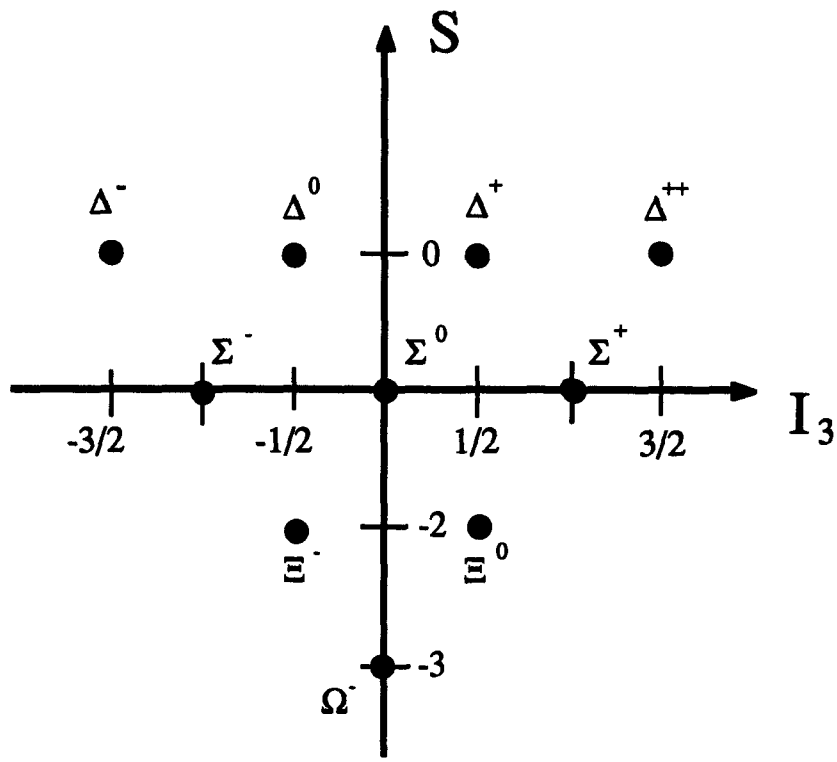

Figure 2-2. Decuplet of $J^P=3/2^+$ plotted in the I_3-S plane.

1675 MeV/c^2. The kinematically allowed $\Delta S=1$ decays, where S is the strangeness quantum number, for this particle would be;

$$\Omega^- \rightarrow \Lambda + K^-$$

$$\Omega^- \rightarrow \Xi^- + \pi^\circ$$

$$\Omega^- \rightarrow \Xi^\circ + \pi^-$$

When, in 1964, the Ω^- was discovered with the above decay modes, the correct quantum numbers and a mass of 1672 MeV (Barnes et al. 1964), it was a major triumph for the SU(3) theory.

In SU(3), the basic multiplet from which all other multiplets are formed is a triplet. This implies that the patterns found in the known hadrons of the time can be explained by postulating three types of fermion constituents (along with their antiparticles). In 1964, M. Gell-Mann (Gell-Mann 1964), and independently Zweig (Zweig 1964), proposed a model based on these constituents. Gell-Mann called these particles quarks. Quarks are fractionally charged particles with either Q=+2/3|e| or Q=-1/3|e|. The three different types or flavors of quarks in SU(3) are the up (u), the down (d) and the strange (s) quark. Figure (2-3) shows the SU(3) quark triplet and table (2-1) lists the quantum numbers of these quarks and their antiparticles.

In the quark model, mesons are composed of a quark and an antiquark ($q\bar{q}$). From SU(3) we expect $3 \otimes \bar{3} = 8 \oplus 1$ states. That is an SU(3) singlet and an octet. Figure (2-4) shows the meson octet in the I_3-Y plane, where Y is defined

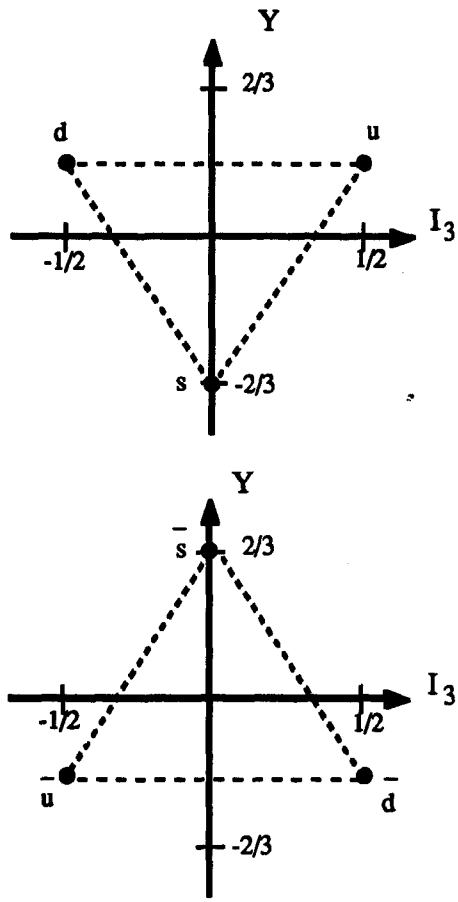

Figure 2-3. The SU(3) quark and antiquark triplets plotted in the I_3-Y plane.

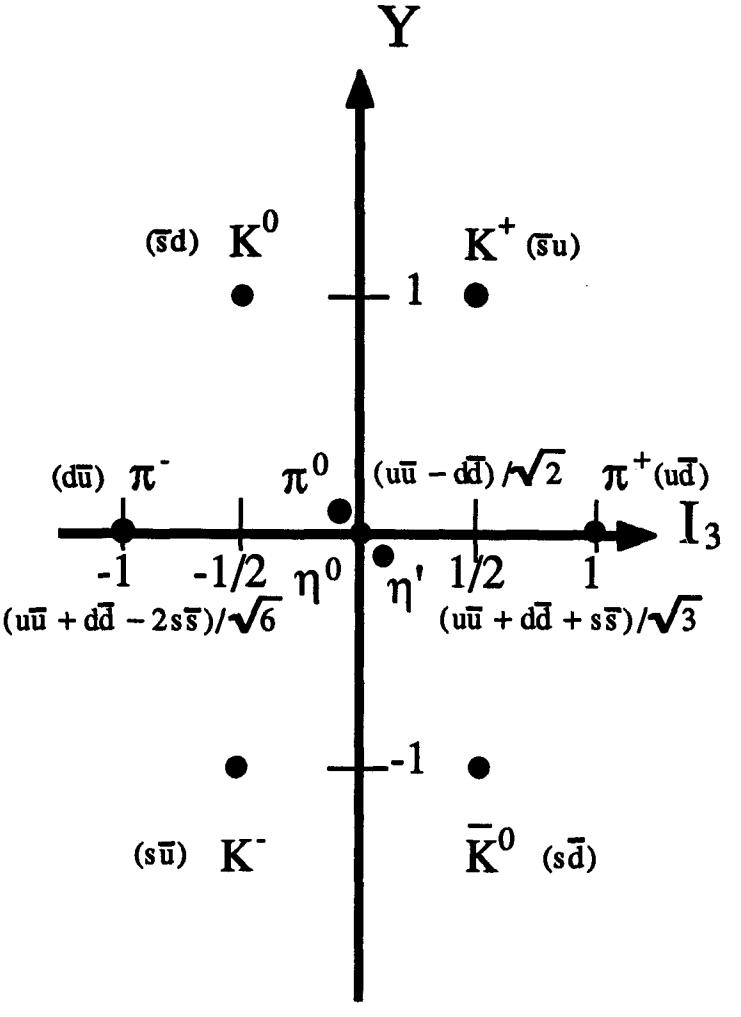

Figure 2-4. The lowest lying meson octet The $J^P=0^-$ pseudoscalar mesons. Also shown is the singlet state, the η'.

Table 2-1

SU(3) Quarks

Quark	B	J	I	I_3	S	Q/e
u	1/3	1/2	1/2	1/2	0	+2/3
d	1/3	1/2	1/2	-1/2	0	-1/3
s	1/3	1/2	0	0	-1	-1/3
$\bar{u}$	-1/3	1/2	1/2	-1/2	0	-2/3
$\bar{d}$	-1/3	1/2	1/2	1/2	0	1/3
$\bar{s}$	-1/3	1/2	0	0	+1	1/3

as B+S and is known as hypercharge; also shown in this figure is the singlet state, η'. These are the $J^P=0^-$ or pseudoscalar mesons. In the figure, the quark content of each meson is given with the meson name.

Baryons in this model, are composed of three quarks (qqq) with the expected SU(3) decomposition being $3 \otimes 3 \otimes 3 = 10 \oplus 8 \oplus 8 \oplus 1$. The decuplet states are totally symmetric under the interchange of two quarks, the octet states are of mixed symmetry and the singlet state is antisymmetric. If we assume that quarks of particles in the lowest mass $J^P=3/2^+$ decuplet are in the spatially symmetric ground state, the value of J is obtained by having the quark spins in a symmetric state. That means the quark spins are parallel, for instance $\Delta^{++}= u\uparrow\ u\uparrow\ u\uparrow$. However this means we have three identical fermions in a totally symmetric state in space, spin and flavor. Since this state is forbidden by Fermi statistics, we are

led to seek an antisymmetric part of the wave function.

This leads to the introduction of a new property or quantum number for quarks, called color. Quarks would then have three possible colors-red, blue and green (R,B,G). Further, it is postulated that all hadrons are colorless combinations of quarks. This means they belong to the SU(3) color singlet, so the color wave function for a baryon is antisymmetric. The overall spin $\times$ space $\times$ flavor part of the baryon wavefunction must then be symmetric. The SU(2) spin decomposition for baryons is expected to be $2 \otimes 2 \otimes 2 = 4 \oplus 2 \oplus 2$. When this SU(2) spin decomposition is combined with the flavor decomposition above, we are left with two symmetric multiplets. A decuplet which is symmetric in both flavor and spin, and an octet with mixed symmetry in flavor and spin independently, but that is symmetric when the two are combined.

When presented in this manner, the concept of color seems plausible, but somewhat contrived. However, this not only clears up the problem with quarks and Fermi statistics, but also reconciles the predictions of the quark model with the results of experiments. For instance, the cross-section ratio

$$\frac{\sigma(e^+e^- \rightarrow \text{hadrons})}{\sigma(e^+e^- \rightarrow \mu^+\mu^-)} = N_C \sum_i e_i^2$$

where N_c is the number of colors and e_i is the charge on a quark of flavor i, requires a value for N_c of three to within 10%. Also, the predicted decay rate for; $\pi^o \rightarrow \gamma\gamma$ was different from the actual rate by approximately a factor of nine. But, this problem is

also solved because with color the rate is proportional to the square of the number of colors.

In November of 1974, a group led by J. B. Richter at the Stanford Linear Accelerator Center (SLAC) discovered a very narrow resonance in e^+e^- collisions at $\sqrt{s}$=3.1GeV (Augustin et al. 1974). This resonance was simultaneously observed in collisions of 28 GeV protons on a beryllium target by a group led by S. Ting at the Brookhaven laboratory (Aubert et al. 1974). The SLAC group named this particle the Ψ, while the Brookhaven group called it the J. It is now normally referred to as the J/Ψ.

The fact that this resonance was so narrow excluded any explanation of it in terms of the three quarks u, d and s. The resonance was explained as a bound state of a new quark flavor and its antiquark. The new flavor is the charm quark; its quantum number is c=1 for a charm quark and c=0 for other quarks. Charm is conserved in strong and electromagnetic interactions in complete analogy with strangeness. The existence of the charm quark had been postulated in 1970 by Glashow, Iliopolous and Maiani (Glashow, Iliopolous and Maiani 1970) to explain the absence of strangeness changing neutral weak currents.

In 1977 another narrow resonance, this time in the mass region 9.5-10.5 GeV/c^2, was found and was called the upsilon (Herb et al. 1977). This was attributed to the lowest bound state of another new quark flavor and its antiquark. This "bottom" quark has a quantum number B*=-1 for bottom quarks and B*=0 for other quarks; again B* is conserved in strong and electromagnetic interactions.

The discovery of the bottom quark has lead to intense searches for an even

heavier quark called top. The existence of top would allow the quarks to be grouped into three doublets as are the leptons:

(e,ν_e) (u,d)

(μ,ν_μ) (s,c)

(τ,ν_τ) (b,t).

All of the properties of the t-quark are easily predicted except for the mass for which only a lower limit is known.

III. Lepton-Nucleon Scattering

None of the evidence presented for the quark model so far has been direct, and in fact in the early 1960's the emphasis was on the symmetries of SU(3) rather than quarks as actual particles. Indeed, quarks were thought to be mathematical fictions used to describe the symmetries among the particles. However, in the late 1960's, experimental evidence began to suggest that quarks might be more than was previously thought.

In 1968 (Bartel et al. 1968), evidence for the existence of quarks started coming from experiments involving deep inelastic scattering of leptons (electrons, muons, neutrinos) off of nucleons. Since the leptons do not interact strongly, they may be used to probe the nucleon through electromagnetic and weak interactions. Using leptons, and in particular electrons, scattered off of an object to determine the charge distribution of the object was already a well proven technique.

Electron-proton scattering is thought to be dominated by single virtual photon exchange; two photon exchange is thought to be unimportant. This is because of the equality between the electron-proton and the positron-proton cross-sections, which have opposite signs for the perturbative second order two photon terms in

Feynman diagrams.

As the four momentum transfer (q) between the incident electron and the target nucleon increases, the nature of the interaction changes. Increasing q^2 is the same as decreasing the wavelength of the virtual photon, or equivalently increasing the resolution of the probe. At small values of q, the wavelength of the virtual photon is too long to 'see' inside the proton and the scattering is mainly elastic.

If the proton had no internal structure, then the scattering would always be elastic. In this case, the cross-section would be given by

$$\frac{d^2\sigma}{dE'd\Omega} = \frac{4\alpha^2E'^2}{q^4}[\cos^2(\frac{\theta}{2}) - \frac{q^2}{2m^2}\sin^2(\frac{\theta}{2})]\,\delta(\nu + \frac{q^2}{2m}) \qquad (2.1)$$

where E' is the energy of the electron after the scatter, ν is defined as the energy transfer and θ is the angle with respect to the incident electron direction through which the electron is scattered. What was revealed by experiments was that as the q^2 increased, the scattering could only be explained as quasielastic scattering off of the nucleon constituents. More quantitatively, in the lab reference frame, the cross-section is given by (Halzen and Martin 1984, 184)

$$\frac{d^2\sigma}{dE'd\Omega} = \frac{4\alpha^2E'^2}{q^4}[W_2(\nu,q^2)\cos^2(\frac{\theta}{2}) + 2W_1(\nu,q^2)\sin^2(\frac{\theta}{2})] \qquad (2.2)$$

The form factors, W_1 and W_2, incorporate the possible longitudinal and transverse polarizations of the exchanged virtual photon.

What was found in the experiments was that W_1 and W_2 do not depend on q^2 and ν independently but are dependent only on the ratio $x = |q^2|/2M\nu$, where M is the mass of the point-like constituent of the proton. That is, for sufficiently large $-q^2$;

$$2W_1 = \left(\frac{Q^2}{2M^2}\right)\delta\left(\nu - \frac{Q^2}{2M}\right) \qquad (2.3)$$

$$W_2 = \delta\left(\nu - \frac{Q^2}{2M}\right) \qquad (2.4)$$

where $Q^2 \equiv -q^2$. When (2.3) and (2.4) are substituted into (2.2), the cross-section has the characteristic form of elastic scattering off of a pointlike particle. By using the identity $\delta(ax)=(1/a)\delta(x)$, equations (2.3) and (2.4) can be rewritten

$$2MW_1 = \left(\frac{Q^2}{2M\nu}\right)\delta\left(1 - \frac{Q^2}{2M\nu}\right) \qquad (2.5)$$

$$\nu W_2 = \delta\left(1 - \frac{Q^2}{2M\nu}\right) \qquad (2.6)$$

so W_1 and W_2 depend only on the ratio $2M\nu/Q^2$. This is known as Bjorken scaling (Bjorken 1967). Bjorken scaling implies that the electrons were scattered off of pointlike constituents of the nucleon. This was put in physical terms by the parton model of Feynman (Feynman 1969).

IV. The Parton Model

The physical interpretation of Bjorken scaling was provided by the parton model of R. Feynman in 1969. In this model the reference frame is that in which $|p|>>M$ (the infinite momentum frame) where p and M are the momentum and mass of the nucleon respectively. In this frame the mass of the nucleon can be neglected. So the nucleon has a 4-momentum P=(p,0,0,ip) and is thought to consist of a parallel stream of partons, where the i^{th} parton has a four-momentum $x_i P$, where $0<x_i<1$. Figure (2-5) shows schematically how deep inelastic scattering occurs in this model.

The nucleon is made up of partons with $\Sigma_i(x_i P)=P$ in this model. The variable x can be thought of as the fractional momentum of the nucleon that the parton carries or as the fractional mass of the nucleon carried by the parton. If one parton of mass m and momentum fraction x is elastically scattered by absorbing the current 4-momentum q from the scattering lepton, then the structure functions become

$$F_1(\omega) = \frac{Q^2}{4mvx}\delta(1-\frac{Q^2}{2mv}) = \frac{1}{2x^2\omega}\delta(1-\frac{1}{x\omega}), \qquad (2.7)$$

$$F_2(\omega) = \delta(1-\frac{Q^2}{2mv}) = \delta(1-\frac{1}{x\omega}). \qquad (2.8)$$

If the results for one parton, (2.7) and (2.8) are summed over the partons making up

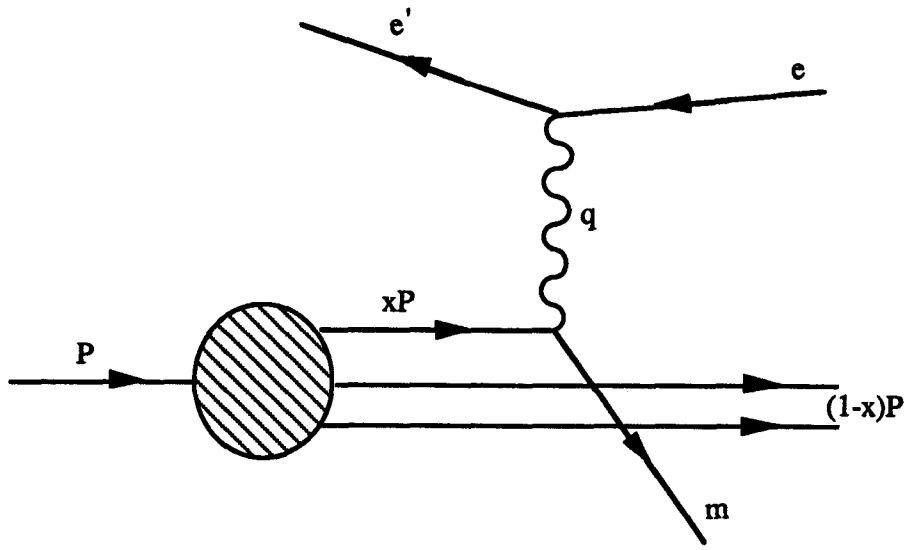

Figure 2-5. Deep inelastic scattering in the parton model.

the proton, we find at large Q^2

$$F_2(x) = \sum_i e_i^2 x f_i(x) \qquad (2.9)$$

$$F_1(x) = \frac{1}{2x} F_2(x) \qquad (2.10)$$

where e_i is the charge on the i^{th} parton and $f_i(x)$ is the probability that the i^{th} parton has a momentum fraction x. From the delta function in equations (2.7) and (2.8), $x=1/\omega=Q^2/2M\nu$. That is the momentum fraction of the parton is found to be identical to the dimensionless kinematic variable ω of the virtual photon. So the virtual photon must have just the right value of ω to be absorbed by a parton of momentum fraction x.

In the infinite momentum frame, relativistic time dilation slows down the rate of interaction between partons. So, during the short time of interaction between the virtual photon and the parton, the parton is essentially a free particle.

Lepton-nucleon scattering is also a good tool to probe the properties of the partons. The experimental parton properties, such as the electromagnetic and weak cross-sections, have proven to be consistent with the proposed properties of the fractionally-charged quarks. However, the quarks account for only about 50% of the momentum of the nucleon. This implied the existence of another type of nucleon constituent, which would not interact with leptons. These new constituents are called gluons and are massless vector bosons. Gluons serve as the quanta of the strong force between quarks.

V. QCD

The concept of color was originally introduced to deal with the Δ^{++}'s apparent violation of Fermi statistics. But color also plays a role in quantum chromodynamics (QCD), the gauge theory of strong interactions between quarks. In this theory, color is the charge of strong interactions. The prototype of renormalizable gauge field theories is quantum electrodynamics (QED). QED describes the interactions of photons with matter, it is the best studied and most successful gauge field theory. QCD was developed along the lines of QED and it is similar in many respects to QED. Color in QCD is analogous to electric charge in QED. In QED, the propagator of force is the photon, a spin 1 massless boson; and in QCD, the propagator of force is also a spin 1 massless boson, the gluon.

However, QED is an Abelian U(1) gauge theory with two charge states and an uncharged mediating boson. QCD is a non-Abelian gauge theory with six types of charge (three colors and three anti-colors) and a charged mediating boson. Quark-quark strong interactions are assumed to be invariant under color interchange, therefore they are described by the symmetry group SU(3) of color. Unlike SU(3)

flavor symmetry, SU(3) color symmetry is exact. This means the mediating boson, the gluon, is massless. Since there are three colors of quarks, the quarks belong to the triplet representation of SU(3). Gluons carry two colors, so there are 9 possible combinations. However the singlet state, $(R\bar{R}+B\bar{B}+G\bar{G})/3$, carries no net color charge. It will not contribute to the strong force and therefore is excluded. So we are left with eight different possible gluons which belong to an SU(3) octet.

There are two aspects of strong interactions that are strikingly different from electromagnetic interactions. The first is the behavior of quarks at very small separations or very large momentum transfers. In this regime, quarks behave as if they were free particles. This is known as asymptotic freedom. At the other extreme is quark confinement, clearly demonstrated by the fact that no quark has ever been detected outside of a hadron.

First we will address the concept of asymptotic freedom. Like QED, QCD calculations are done on a perturbative basis. If the higher order QCD terms, in α_{strong}, are sufficiently small that the series converges rapidly, only first (or possibly second) order terms need to be calculated. Unlike QED, where the running coupling constant is given by:

$$\alpha_{EM} = \frac{c_1}{1 - \frac{c_1}{3\pi}\ln(\frac{q^2}{q_0^2})}$$

the strong running coupling constant, given by:

$$\alpha_{strong} = \frac{c_2}{1 + \frac{c_2}{12\pi}(33 - 2n_f)\ln(\frac{q^2}{q_0^2})} = \frac{constant}{\ln(q^2/\Lambda^2)}$$

increases as the distance between the quarks increases and as the momentum transfer decreases. In fact, perturbation theory is only appropriate for processes with $q>>\Lambda$ also called 'hard' processes. Carrying this further, it is clear that as q^2 continues to grow, $\alpha_{strong} \rightarrow 0$, or the quarks behave as if free. So QCD explains asymptotic freedom.

Quark confinement is not as easy; in fact quark confinement does not necessarily follow from QCD. Since α_{strong} becomes very large in the case $q \approx \Lambda$, perturbative methods are meaningless in this regime. But, since gluons carry the color charge permitting gluon-gluon interactions, one possible explanation is provided. As quarks separate, the color interaction strengthens; squeezing the color lines of force between the quarks into a narrow tube. If the energy density inside this tube is constant, the potential between the quarks will increase to the point where quark antiquark pairs are formed between the separating quarks. These then become the ends of the lines of force, so that there are now two tubes of force. By this mechanism the total energy is lowered despite the cost of the mass of the new quarks.

If this idea is valid, quarks would never be seen as free particles. Separating quarks inside a hadron would only lead to the creation of more hadrons. This is consistent with the experimental evidence to date. Despite this fact, the search for free quarks is vigorously pursued.

VI. Weak Interactions

As was stated earlier, the only way for the decay $\Lambda \rightarrow p + \pi^-$ to proceed is via the weak interaction. The striking feature of this decay is the long lifetime of the particle involved. The lifetime of a decay is inversely related to the coupling strength of the interaction involved, so the relatively long lifetime indicates a coupling strength $\alpha_{weak} << \alpha_{EM} << \alpha_{strong}$, thus the name weak interactions. Both hadrons and leptons experience weak interactions, but they are often hidden by the more dominate strong and electromagnetic interactions. Before proceeding to the discussion of experiment E735 in the next chapter, we will conclude our survey of some of the concepts of particle physics with a brief look at some aspects of weak interactions.

In general, the decays of hadrons can be viewed as a transformation of a single quark while the other quarks play the role of 'spectators'. For example, in the decays;

$$\Lambda \rightarrow p + \pi^- \; ; \; uds \rightarrow uduW^- \rightarrow udu(\bar{u}\bar{d}) \rightarrow udu + \bar{u}\bar{d}$$

$$\Lambda \rightarrow n + \pi^0 \; ; \; uds \rightarrow uduW^- \rightarrow ud(\bar{d}\bar{u})u \rightarrow udd + \bar{u}\bar{u},$$

the s quark transforms into a u quark and a W^- and the u and d quarks in the Λ are

"spectators". For the non-leptonic weak decays of strange particles, it has been found that the selection rules; $\Delta S=1$, $\Delta I=1/2$ are followed. When the strange particle decays are semi-leptonic, the hadrons involved follow the selection rule; $\Delta q=\Delta S=1$. This is expected, if $\Delta I_3=1/2$ from the relation $Q=I_3+[S+B]/2$.

As was mentioned earlier in this chapter, strange particles were named for their long lifetime. Comparing the decay rates for $\Delta S=0$ transitions to the rates for $\Delta S=1$ transitions shows that $\Delta S=1$ transitions are suppressed with respect to the $\Delta S=0$ transitions by a factor of about 20. In 1963 Cabibbo (Cabibbo 1963) proposed a theory to account for the suppression of weak decays of strange particles. In the Cabibbo model, the u, d and s quarks which participate in weak interactions are organized in a doublet with the one member of the doublet being a mixture of the d and the s quarks.

$$u' = u$$
$$d' = d\cos(\theta_c) + s\sin(\theta_c)$$

With the weak coupling constant given by the Fermi constant, G_F. Decays with $\Delta S=0$, for instance $n\rightarrow pe^-\bar{\nu}_e$, occur with a rate proportional to $G_F\cos^2(\theta_c)$, while $\Delta S=1$ decays, for instance $\Lambda\rightarrow pe^-\bar{\nu}_e$, have a rate proportional to $G_F\sin^2(\theta_c)$. So;

$$\frac{\Gamma(\Lambda \rightarrow p^+e^-\bar{\nu}_e)}{\Gamma(n \rightarrow p^+e^-\bar{\nu}_e)} = \tan^2(\theta_C) \approx 0.05$$

where 0.05 arises from the experimental observation, mentioned above, that $\Delta S=1$ decays are inhibited by a factor of about 20 with respect to $\Delta S=0$ decays. This type of comparison of decay rates yields a value consistent with $\theta_c=13°$, after accounting for kinematic factors arising from quark mass effects. When we

generalize to the 6 quark case, there are three mixing angles and a phase. The 3×3 matrix which represents the transformation to the "mixed" quarks in this case is referred to as the Kobayashi-Maskawa matrix (Kobayashi and Maskawa 1972).

The present theory of weak interactions is a version of QED extended to unify electromagnetic and weak interactions, collectively called electroweak interactions. It has come to be known as the Standard Model. The SU(2)xU(1) form of the electroweak interaction was first proposed by Glashow (Glashow 1961) in 1961. Weinberg (Weinberg 1967) and Salam (Salam 1968) extended this model to include massive vector bosons (W^+,W^-, Z°). This theory requires two coupling constants, one for the SU(2) symmetry, denoted g, and one for the U(1) symmetry represented by g'. Adding the constraint that the electromagnetic current must be present in the electroweak interaction gives the relation $g \sin(\theta_W) = g' \cos(\theta_W) = e$ where θ_W is the weak mixing angle.

In this theory, all known fermions are grouped into a left-handed doublet and a right-handed singlet. The concepts of "weak isospin", the SU(2) part of the theory, and 'weak hypercharge', the U(1) part, are introduced. Table (2-2) shows the groupings of the elementary fermions for the weak interaction. The interaction can be separated into three parts, one for weak charged currents, one for weak neutral currents and one for electromagnetic currents. As shown by the relative coupling strength, g^c, charged weak currents act only on the members of the left-handed doublet, all with the same strength. Neutral weak currents, on the other hand, act on both the left-handed doublets and the right-handed singlets with

Table 2-2

Electroweak Particle Families

				I_3	Q	g^c	g^N
			Left-handed lepton doublets				
ν_l	ν_e	ν_μ	ν_τ	1/2	0	1	1/2
l	e	μ	τ	-1/2	-1	1	-1/2+x
			Left-handed quark doublets				
q_1	u_L	c_L	t_L	1/2	2/3	1	1/2-2/3x
q_2	d_L'	s_L'	b_L'	-1/2	-1/3	1	-1/2+4/3x
			Right-handed singlets				
l_R	e_R	μ_R	τ_R	0	-1	0	x
q_{1R}	u_R	c_R	t_R	0	2/3	0	-2/3x
q_{2R}	d_R	s_R	b_R	0	-1/3	0	1/3x

varying strengths, the relative coupling strength given by $g^N=I_3-Q\sin^2(\theta_W)$. Of course electromagnetic currents couple to right-handed and left-handed components equally with a strength which depends on the charge. The primed quarks in table (2-2) are the rotated quarks determined from the Kobayashi-Maskawa mixing matrix.

Like QCD, the electroweak gauge theory is a non-Abelian theory, and

therefore, the intermediate vector bosons (W^+,W^-,Z°) can couple to each other. Unlike QCD, the mediating bosons in this theory are massive. This is due to spontaneous symmetry breaking. This model makes several predictions. First the massive mediating bosons predicted by the theory, the W^+, W^- and the Z°, have been observed (Arnison et al. 1983 Banner et al. 1983, Bagnaia et al. 1983). Second, all electroweak interactions must be consistent with a single value of θ_W, which is true thus far. Also the angular distributions in the reactions $e^+e^- \rightarrow \mu^+\mu^-$ and $e^+e^- \rightarrow \tau^+\tau^-$ must show the effects of interference between the electromagnetic current and the neutral weak current. Experimental evidence for this effect has been seen (Wu 1984). Finally, in order for the bosons to have masses, at least one "isospin" doublet called Higgs scalars has been postulated so that the divergences associated with the boson masses cancel, but they have yet to be discovered. Regardless, the unification of electromagnetic and weak interactions is a very appealing notion.

Chapter 3

Experiment E735

The data which were analyzed for this thesis are from experiment E735, which was located at the C0 intersection region of the Fermi National Accelerator Laboratory (FNAL) Tevatron Collider. In collider mode, the Tevatron uses counter rotating bunches of protons and antiprotons, which collide at six points around the Tevatron ring at $\sqrt{s}$ =1.8 TeV. The data were taken during the first running period of E735, from January 1987 to May 1987. During this period, approximately

five million triggers were written to magnetic tape from an integrated luminosity of about $1/3nb^{-1}$.

It is generally accepted that in central relativistic collisions, enough kinetic energy is converted into heat to create a locally deconfined plasma of quarks and gluons. Less understood is the time development of the plasma. More specifically, the process through which the plasma returns to the normal hadronic state is unclear. This process is important, because it affects the decay products of the plasma through which its production may be detected. One proposed signature of plasma production is increased production of strange particles, especially antihyperons, due to the increased cross section for $gg \rightarrow s\bar{s}$.

In the first part of this chapter, the physics underlying the formation, evolution, hadronization and detection of quark-gluon-plasma (QGP) will be discussed. The second part of this chapter describes the detector for E735 and the data acquisition (DA) system.

I. EXPERIMENTAL MOTIVATION

It is expected that at sufficiently high collision temperatures ($T \approx 200$ MeV) or baryon densities ($\rho_B \approx 1.5$ fm^{-3}), the normal quark confinement in hadrons will give way to a deconfined plasma state. A simple model can be used to understand qualitatively the reasoning behind this theory. Remember that at large distances, the force between quarks becomes very large and therefore effects the nature of the surrounding vacuum; while quarks, at short range, are asymptotically free. Therefore to first order, the QCD vacuum can be thought of as having two states. Outside of hadrons, in the absence of quarks and gluons, is the normal vacuum. In this phase of the vacuum, physical quarks and gluons cannot exist. Inside of hadrons, there exists a state of the vacuum which can be called the perturbative vacuum. In this QCD vacuum phase, quarks and gluons propagate freely.

Normally, at low quark (antiquark) density, the perturbative vacuum, and therefore quarks, exist only inside hadrons. If, however, the quark (antiquark) density is raised, by raising the baryon density or by thermal production of hadrons,

then a phase transition to a QGP can occur. In the language of the two state QCD vacuum model, the spaces of normal vacuum between the hadrons are squeezed out by the increasing volume occupied by the perturbative vacuum (the hadrons). As the hadrons overlap, a region of space is completely filled with the perturbative vacuum. Inside this plasma, quarks and gluons are free to travel over the entire volume.

In high energy collisions, three different regions of QGP formation are expected. Figure (3-1) schematically shows these three regions. The two fragmentation regions are areas of phase space where the particles have most of the longitudinal momentum of the incident particles. In these regions the net baryon number of the particles is close to that of the colliding particles. Formation of QGP in these regions has been predicted mainly for nucleus-nucleus collisions (Anishetty, Koehler and McLerran 1980). In the fragmentation regions, plasma formation would proceed through thermalization of the nuclear fragments by rescattering in nuclear matter.

Connecting the two fragmentation regions is the central region. In this region, the longitudinal momentum of the particles is low. Few fragments of the initial particles are found in this area of phase space and the products are mostly mesons. It has been suggested (Bjorken 1983) that at sufficiently high energy densities, QGP formation in this region of phase space is possible also. In the central region, plasma formation would proceed via the equipartition of the energies of the thermally produced particles through scattering with each other.

In both the fragmentation regions and the central region, the multiple

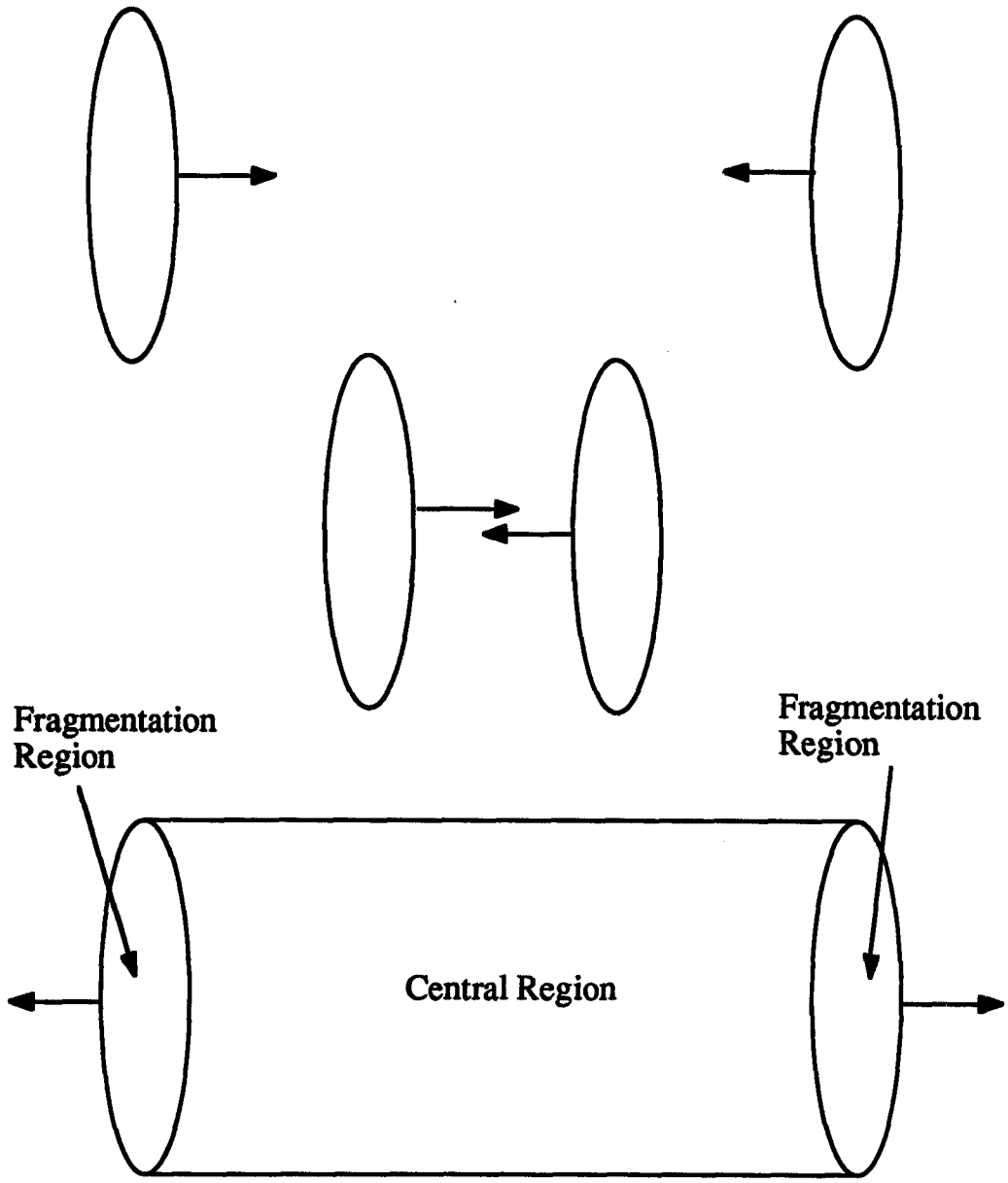

Figure 3-1. Schematic representation of the three regions of quark-gluon plasma formation

scattering would cause hot hadronic matter to form. If the matter were sufficiently dense and hot, a plasma of quarks and gluons would be formed. To describe the evolution of the plasma, statistical thermodynamics is used. In particular, the evolution has been studied in the context of the grand canonical ensemble (Koch, Müller and Rafelski, 1986) and the Landau hydrodynamic model (Bjorken, 1983). In the fragmentation region, the plasma is expected to expand spherically, such that the entropy ($S \approx VT^3$) of the system remains constant. Therefore, the baryon rich plasma of this region would increase in volume according to the relation;

$$V = V_0 (\frac{t}{T_0})^3 \qquad t > T_0$$

where V_0 is the initial plasma volume and T_0 is characteristic formation time. The temperature of the plasma would then follow the form,

$$\tau = \tau_0 \qquad t < T_0$$
$$\tau = \tau_0 (\frac{t}{T_0}) \qquad t > T_0$$

in this region, where τ_0 is the initial plasma temperature. In contrast, the plasma formed in the central region expands mainly in one dimension, longitudinally. The development of the volume and temperature with time for the plasma in this region is given by;

$$V = V_0(\frac{t}{T_0}) \qquad t > T_0$$

$$\tau = \tau_0 \qquad t < T_0$$

$$\tau = \tau_0(\frac{t}{T_0})^{-\frac{1}{3}} \qquad t > T_0$$

So that a plasma in the central region would appear to take longer to reach the critical temperature to change back to a gas of hadrons.

Figure (3-2) shows a phase diagram in the temperature, baryon density plane. Marked on this plot are the routes taken to reach QGP in the fragmentation region and in the central region. The point marked T_c in the figure is the temperature at which the phase transition would take place at vanishing baryon number. At present, the best estimates of this temperature are obtained from Monte Carlo calculations of QCD on a lattice. Lattice Monte Carlo techniques are the only known way to preform nonperturbative calculations in QCD from first principles. Calculations for SU(2) lattice gauge theory indicate T_c=160-200 MeV (McLerran and Svetitsky, 1981; Kuti, Polonyi and Szlachanyi, 1981; Engels et al. 1981). While SU(3) lattice gauge theory yields T_c also on the order of 200 MeV (Kajantie, Montonen and Pietarinen, 1981; Montvay and Pietarinen, 1982). The major problem with these predictions is the absence of quarks, real or virtual, in the model. The inclusion of quarks in the model would require a modification to the linear force law used in the model at large separation below T_c.

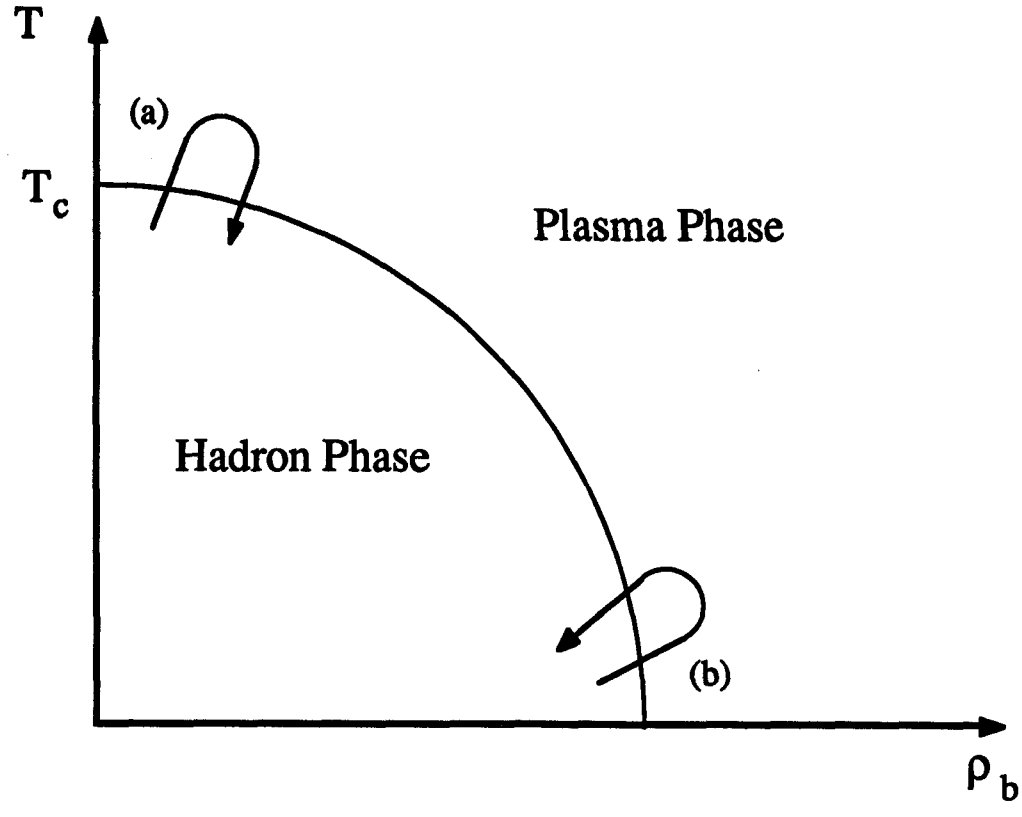

Figure 3-2. Phase diagram in the temperature-baryon number density plane showing the paths taken from hadronic matter to quark-gluon plasma in (a) proton-antiproton collisions and (b) heavy ion collisions.

If the QGP were created, how would it be detected. Because of the small size ($\approx$ 10 fm) and the short lifetime ($\approx$ 10 fm/c), the plasma could not be directly detected. Detection would have to depend on indirect measurements of the decay products of the plasma. Among the suggested experimental probes are correlations between the average transverse momentum ($<p_t>$) and the multiplicity density in rapidity space (dN/dy), correlations in the production of pions, and enhanced strangeness production. Since $<p_t>$ may be interpreted as a measure of the temperature of the matter formed in the collision and dN/dy is proportional to the energy density, structure in the plot of $<p_t>$ versus dN/dy could signal a phase transition in hadronic matter.

Correlations in pion production, the Hanbury-Brown-Twiss effect, arise from interference of the matter waves of identical particles. These correlations are a consequence of Bose-Einstein statistics and can be described by the ratio of the probability of joint pion production, $P(k_1,k_2)$, to the product of single pion production probabilities $P(k_1)P(k_2)$, where k_i is the four momentum of the i^{th} pion. For a thermal source, the ratio is given by;

$$C(k_1,k_2) \equiv \frac{P(k_1,k_2)}{P(k_1)\,P(k_2)} = 1 + \left|\hat{\rho}(k_1 - k_2)\right|^2$$

where $\hat{\rho}(k_1 - k_2)$ is the Fourier transform of the source distribution (Juricic et al. 1989). So, information about the space-time structure of the pion source is contained in the term $\left|\hat{\rho}(k_1 - k_2)\right|^2$. Since it is not possible to calculate $P(k_i)$ accu-

rately for most experiments, the distribution of like sign pairs is usually compared to a normalized reference sample of pairs. The reference pairs (for example opposite sign pairs) should be free of Bose-Einstein correlations. The distribution of the ratio of the two samples can be parameterized by $R(Q^2) = 1 + \lambda e^{-r^2 Q^2}$, where $Q^2 \equiv -(k_1 - k_2)^2 = M_{12}^2 - 4m^2$.In this formula, M_{12} is the invariant mass of the pair and m is the pion mass. The parameters λ and r are obtained from fits to the data. It has been claimed that λ is a measure of the coherence of the source (Fowler and Weiner, 1977) and that r is a measure of the size of the emitting region (Juricic et al. 1989). Figure (3-3) shows a plot of R versus Q^2 in e^+e^- collisions showing the Hanbury-Brown-Twiss effect at $Q^2<0.2$ GeV/c^2. So, in principle, by looking at the correlation of like sign pion pairs, information about the space-time structure of the plasma near the transition back to hadrons may be obtained.

Production of direct photons may also provide information about the QGP. Prompt photons are produced, to lowest order in α_s, by $qg \rightarrow q\gamma$ in the plasma. Arguing on the basis of high quark density in the plasma ($\rho_q \approx 7$ quarks/fm^3), it has been suggested that an enhancement of photon production may signal the presence of QGP. A γ/π ratio as high as 20% has been predicted for prompt γ's from a plasma (Halzen and Liu, 1982). Halzen and Liu also point out that at high temperature (T), prompt photons produced in the plasma have an average energy proportional to T. So, by the measuring the prompt photon spectrum, it is, in principle, possible to find the plasma temperature.

Another proposed probe of QGP is dilepton production. In the plasma phase, dileptons are produced by $q\bar{q} \rightarrow \gamma^* \rightarrow l^+ l^-$ while in the hadron phase, $\pi^+\pi^- \rightarrow l^+ l^-$

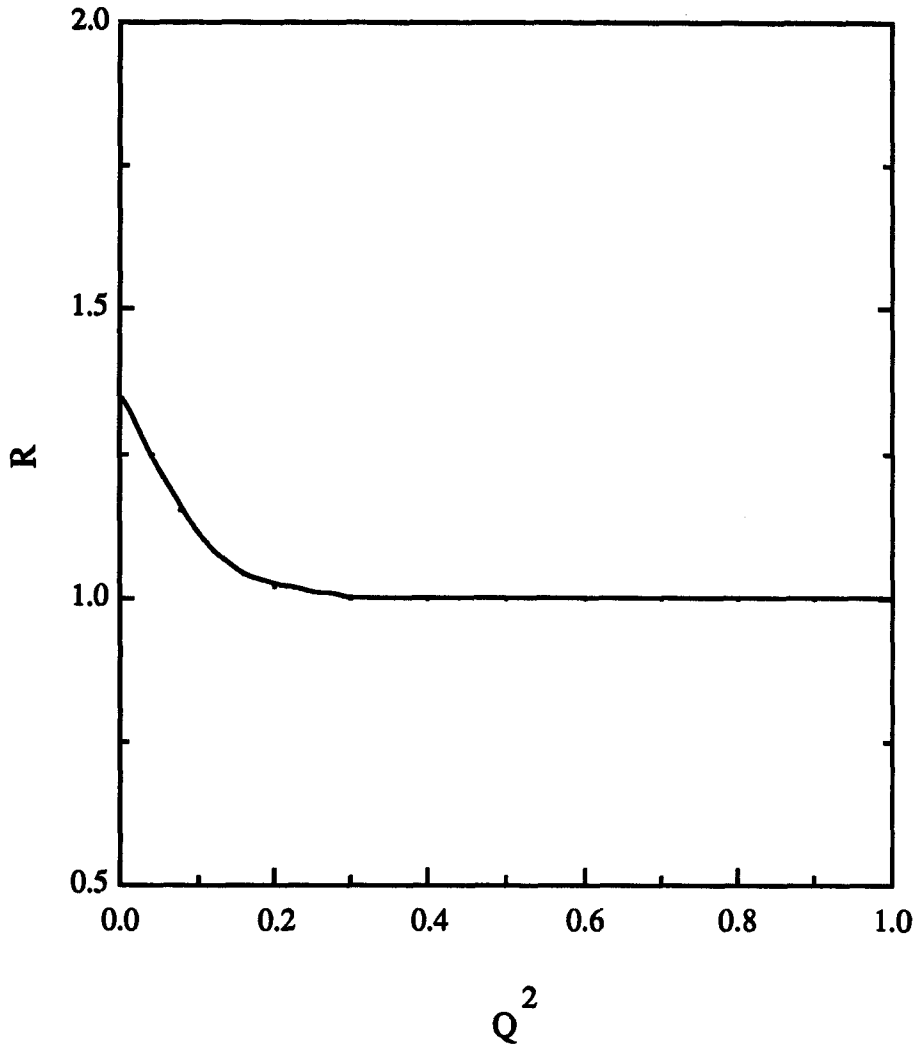

Figure 3-3. Typical plot of the ratio of same sign pion pairs to a reference sample of pairs versus Q^2, showing the Hanbury-Brown-Twiss effect for $Q^2<.2$ GeV/c^2 (Juricic et al. 1989).

produces dileptons. Again, the fact that the two quarks which interact are locally free rather than confined inside separate hadrons leads to an enhancement. In this case the production of dileptons is increased with the creation of the plasma (Domokos and Goldman, 1980). A correlation is suspected between regions of the dilepton mass (M) spectrum and stages during the evolution of the plasma. For $1<M<3$ GeV/c^2 the rate is thought to be sensitive to the initial plasma temperature because of the early time of emission of these pairs. For the same reason, transverse flow effects should not be present for pairs in this region. For events having large multiplicity density (dN/dy), the dilepton rate should be proportional to $(dN/dy)^2$ (Kajante and McLerran, 1987). Pairs with $M \approx 1 GeV/c^2$ are emitted after the plasma has cooled to the temperature at which the transition back to hadrons takes place. So, these pairs should show transverse flow effects. While pairs with $M>3$ GeV/c^2 are from the nonthermal single-collision Drell-Yan mechanism and the rates are determined by the structure functions of the quarks inside the hadrons. So dilepton pairs with $M<3$ GeV/c^2 may be good probes of the plasma.

We now turn to the topic of enhanced strangeness production in the QGP. In the QGP, strange hadrons are created in three steps. First $s\bar{s}$ quark pairs are created in the plasma. Second, these strange quarks and antiquarks become part of hadrons as the plasma breaks up. Finally, in strange hadrons they continue to interact through (confined) strangeness creation, annihilation and exchange processes. To lowest order in perturbative QCD, $s\bar{s}$ quark pairs are created in two gluon collisions (figure 3-4) and in light quark-antiquark annihilation (figure 3-5). For well separated individual hadrons, the process $gg \rightarrow s\bar{s}$ can only occur during the

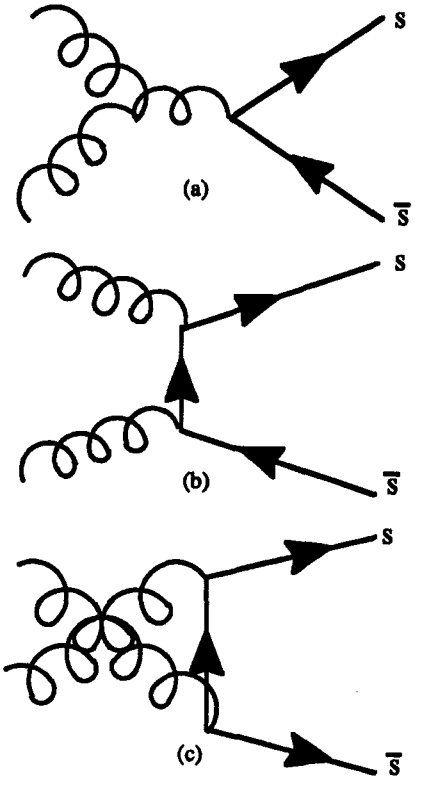

Figure 3-4. Lowest order QCD diagrams for strange quark pair production via two gluon collisions.

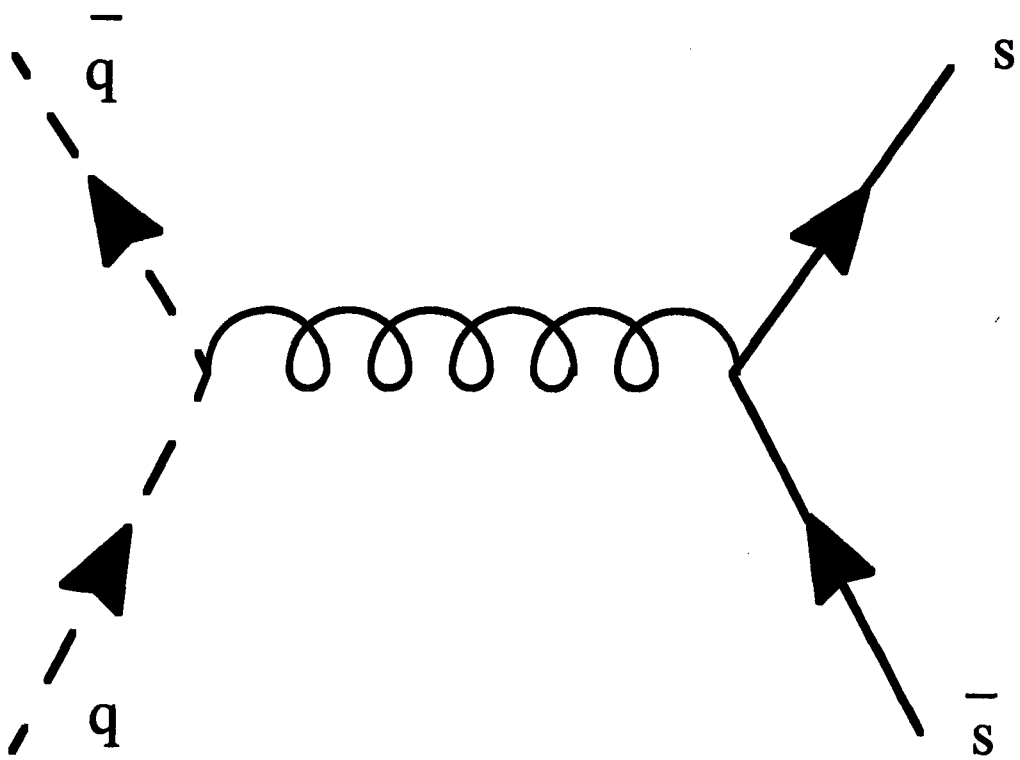

Figure 3-5. Strange quark pair production via light quark-antiquark annihilation, lowest order QCD diagram.

actual collision of two hadrons. However, due to the high gluon density, in a QGP this process occurs at a much faster rate. It has been shown (Rafelski and Müller, 1982) that strange quark production in a QGP is dominated by the gluonic production rate. Also it has been suggested that in a QGP (and only in one) the strangeness abundance saturates for a sufficiently excited plasma, $T \geq 200$ MeV and energy density ≥ 1 GeV/fm^3, because of the high gluon density and the fact that the strange quark mass is comparable to the temperature.

As the plasma cools, the quarks and gluons must recombine to form hadrons. The process of hadron formation from a cooling QGP is not well understood. Several hadronization scenarios have been proposed. The plasma may revert to the hadron phase by forming bubbles of hadronic matter, so that the two phases would coexist during the expansion of the system (Kapusta and Mekjian, 1986). Kapusta and Mekjian have also studied the possibility that the plasma may cool below the critical temperature ($T<T_c$) without a phase transition, then make a sudden transition to a superheated hadron vapor ($T>T_c$) (Kapusta and Mekjian, 1986). Another process that may be present in the hadronization of the plasma is the radiation of mesons. Due to thermal motion, quarks would cross the boundary of the plasma causing a color field flux tube to form. If the quark momentum were high enough, the tube would split by creating a $q\bar{q}$ pair. Half of this pair would join with the escaping quark to form a meson, while the other half would retract into the plasma. Mesons created in this manner would indicate the evolution of the plasma. Hadronization by formation of bubbles of hadronic matter and hadronization by radiating mesons are thought to give approximately equal lifetimes for the plasma

state, so they may be competing processes.

Using a model which is suited to hadron formation in bulk Koch, Müller and Rafelski (Koch, Müller and Rafelski, 1986) argue that abundant production of strange particles is a good signal for the presence of a QGP state. This model is based on a combinatoric distribution of the quarks and gluons into the mesons and baryons formed from the plasma. If only the quarks and gluons present when the plasma begins to hadronize are combined to form the hadrons, then the number of particles is reduced by about a factor of four. For the relativistic particles which make up the QGP and the hadron gas, a reduction in the number of particles is accompanied by a corresponding decrease in the entropy of the system. Quark and gluon fragmentation in this model are introduced so that, during the phase transition, the entropy of the system increases, as required by the second law of thermodynamics.

When a quark-antiquark pair from the plasma combine to form a meson, only one pair in nine will be in a color singlet state ($q\bar{q} \rightarrow \pi$). In the other eight cases, the pair must first radiate a gluon before a meson can be formed ($q\bar{q} \rightarrow \pi g$). Also gluons will fragment into quark-antiquark pairs ($g \rightarrow q\bar{q}$). For zero baryochemical potential ($\mu_b=0$), every gluon and about 1/3 of the quarks must fragment before meson formation. If $\mu_b \neq 0$, the need for fragmentation is reduced. This is because the specific entropy of the more massive baryons exceeds that of a meson. So the actual amount of fragmentation is less when baryons and mesons are formed than when only mesons are assumed to be formed (as was discussed above).

Fragmentation of quarks and gluons allows conservation of entropy and possi-

ble entropy generation in a combinatoric picture of the hadronization process. At any instant, the flavor composition of the quarks is determined by quark reactions and fragmentation. In order to decide if strangeness is enhanced when the plasma is formed, the flavor composition was studied based on a picture of the evolution of the plasma in which: QGP is formed, it expands and cools until it reaches a critical temperature at which point the transition to a hadron gas begins. The plasma is slowly converted into hadronic gas while the temperature and baryochemical potential remain constant. Finally, the entire plasma is converted to a gas of hadrons.

For the early phase in which only the plasma is present, strange quarks are formed mainly through the process $gg \rightarrow s\bar{s}$. Later, when the plasma and hadron gas states coexist, strange quarks hadronize according to the fragmentation-recombination scheme discussed above. In this stage, the abundance of strange particles in the hadron gas must be found in addition to the strange quark abundance in the plasma. The available quarks are distributed among the hadrons using two constant probabilities, one for meson formation and one for baryon formation.

The increase in production of strange particles when a plasma is formed, according to Koch Müller and Rafelski, is due mainly to the increased strange quark production in a plasma versus hadronic matter. Fragmentation of quarks and gluons, introduced in order to obey the second law of thermodynamics, plays a major role in maintaining the strangeness abundance when hadrons are formed. The most striking signal of plasma formation, in this model, is the enhancement in the pro-

duction of antihyperons. Figure (3-6) and figure (3-7) show strange particle abundances for fast ($V \approx t^3$) and slow ($V \approx t$) volume expansion respectively. The figures represent the time when the entire plasma is converted to hadronic gas and are a function of μ_b. It has been suggested that $\mu_b = |x| m_N$, where x is the normal Feynman variable and m_N is the nucleon mass (Greiner, Koch and Rafelski 1984). So, for the area of interest for E735 (the central region), since $x \approx 0$, $\mu_b \approx 0$. The strangeness enhancement is sensitive to the amount of quark (and gluon) fragmentation in the combinatoric model for hadronization, but is present when fragmentation is not included in the model. The main observable, postulated in this argument, is the ratio of antihyperons to antinucleons. Other strange particles, in this model, also show an increase in production in the plasma versus hadronic matter, but these increases are less dramatic.

E735 was designed to look at the central rapidity region in order to search for a phase transition from normal hadronic matter to a deconfined quark-gluon state. This experiment was designed to look at a variety of potential QGP signatures. Other searches for QGP are being conducted mainly at heavy-ion accelerators. These experiments are looking in the high baryon density, low temperature region of the QGP phase diagram. Conversely, E735 probes the high temperature, low baryon density region. E735 hopes that the higher center-of-mass energies at the Tevatron will be the needed advantage in finding a deconfined plasma state.

In order to conduct the search, a detector was designed to sample the transverse momentum spectra of charged particles in the central rapidity region. The detector would also measure the charged particle multiplicity associated with

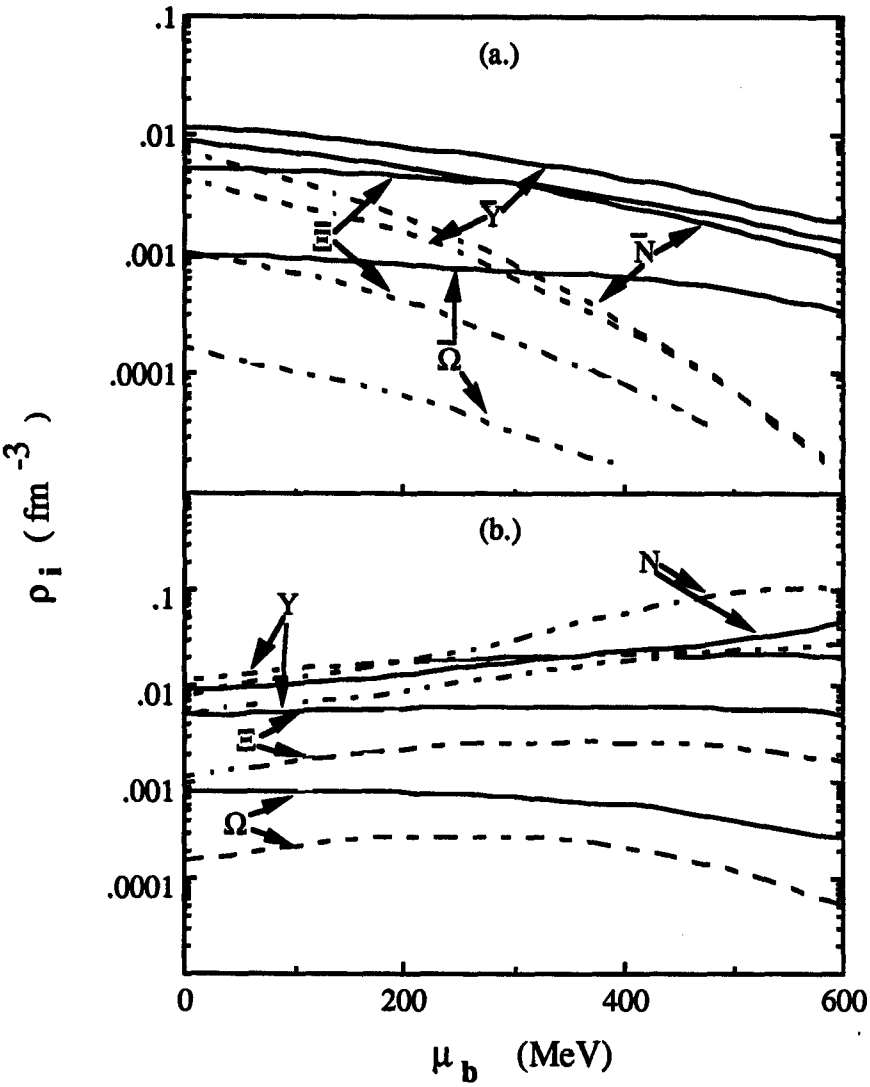

Figure 3-6. Strange particle densities assuming 'fast' volume expansion ($V \approx t^3$) for hadrons with (a.) $\bar{s}$ and (b.) s quarks. Solid lines are density when the plasma is fully converted to hadrons. Dashed lines represent density if a hot hadronic gas is formed (no QGP). (Koch et al. 1986)

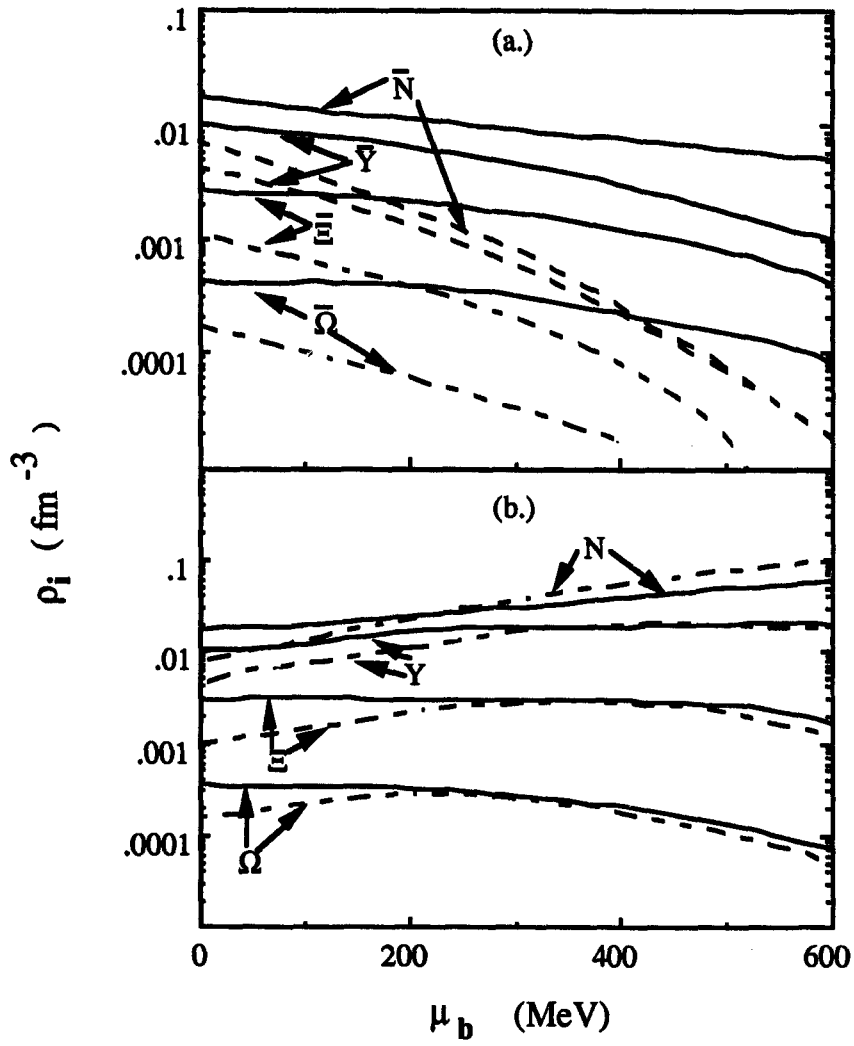

Figure 3-7. Strange particle densities assuming 'slow' volume expansion (V≈t) for hadrons with (a.) $\bar{s}$ s and (b.) s quarks. Solid lines are density when the plasma is fully converted to hadrons. Dashed lines represent density if a hot hadronic gas is formed (no QGP). (Koch et al. 1986)

the event. Particle identification was included to look at particle compositions and transverse momentum spectra of different particles.

II. EXPERIMENTAL SETUP

As was previously mentioned, experiment E735 was conducted at FNAL. Figure (3-8) shows a schematic of the layout at FNAL. As shown in the figure, FNAL is a series of accelerators. In the first stage, negatively ionized hydrogen is accelerated to 750 KeV by a Cockroft-Walton accelerator. A linac then accelerates these ions to 200 MeV. After the linac, a process called Multi-turn Charge Exchange Injection is used to inject positively ionized hydrogen (protons) into the booster. In the booster, the protons are accelerated to 8 GeV. From there, the protons are injected into the main ring either to be used to produce antiprotons or to be used in the actual 1.8 TeV Tevatron ring.

In order to produce antiprotons, the protons are accelerated to 120 GeV in the main ring, extracted and focused onto a copper target. All negatively charged particles which emerge from the target at around 8 GeV are collected by a lithium lens and sent to the Debuncher. Since the protons are in bunches in the main ring, the antiprotons arrive in the Debuncher also in bunches. Here they are redistribut-

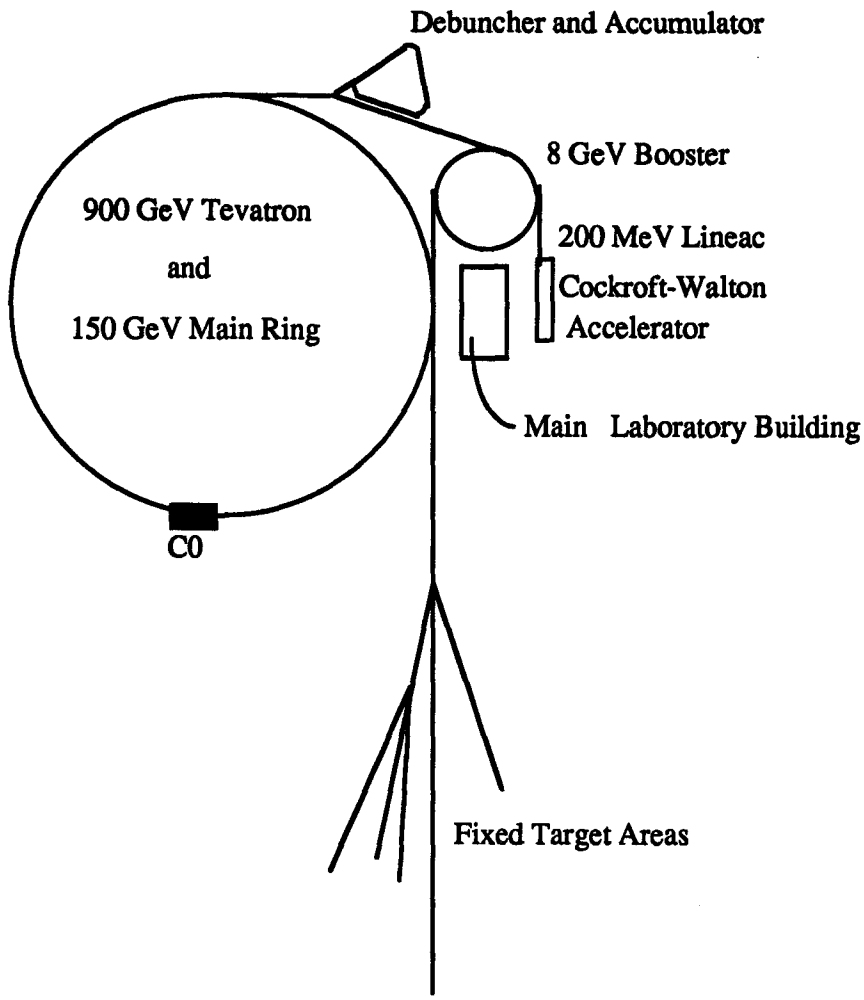

Figure 3-8. Layout of the accelerators at the Fermi National Accelerator Laboratory.

ed continuously , or debunched, and the momentum spread is lessened by stochastic cooling. The antiprotons are then stored at 8 GeV in the accumulator.

For use in collisions in the Tevatron, protons are accelerated to 150 GeV in the main ring and then injected into the Tevatron ring which is located below the main ring. The process is repeated twice more making a total of three proton bunches for a store. Antiprotons are then transferred from the accumulator into the main ring, in a direction opposite to that used for protons, accelerated to 150 GeV and transferred to the Tevatron. Three bunches of antiprotons are also present in a store. When the three proton bunches and the three antiproton bunches are present in the Tevatron, they are then accelerated to 900 GeV, providing 1.8 TeV center of mass energy collisions at six locations around the Tevatron.

Figure (3-9) shows the experimental arrangement for E735 (FNAL E735 Collaboration, 1986). The detector consists of a magnetic spectrometer at 90° and a multiplicity hodoscope surrounding the intersection region. The spectrometer, which has a solid angle coverage of 0.5 sr., samples the momentum spectrum of charged particles and also provides mass identification for charged particles. Two sets of scintillation counters, located close to the beampipe, are used for triggering (Banerjee et al. 1988). These sets of counters are separated by 400cm along the beam direction.

Figure (3-10a) shows the multiplicity hodoscope. The multiplicity hodoscope is made up of a barrel hodoscope and two endcap hodoscopes. Each hodoscope consists of counters using plastic scintillators with a polyvinyltoluene (PVT) base and light guides made from nonscintillating PVT. The barrel hodoscope is situated par-

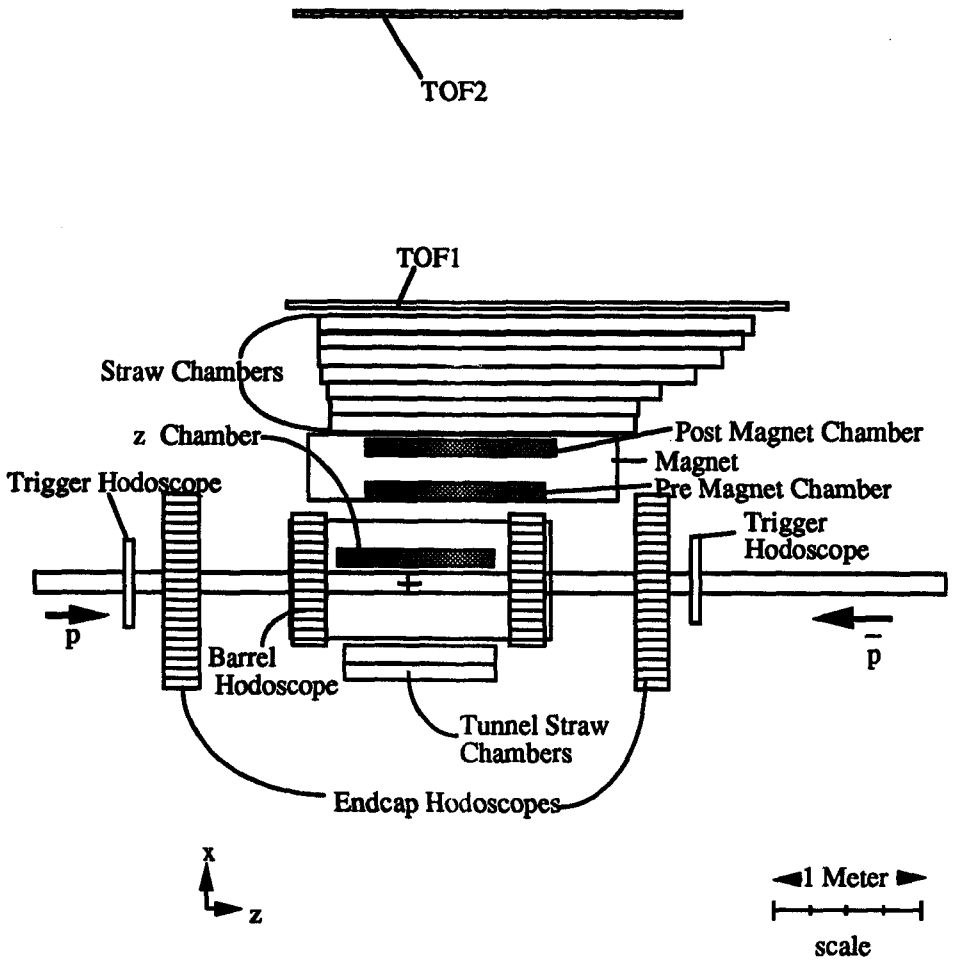

Figure 3-9. Layout of the detector components for experiment E735

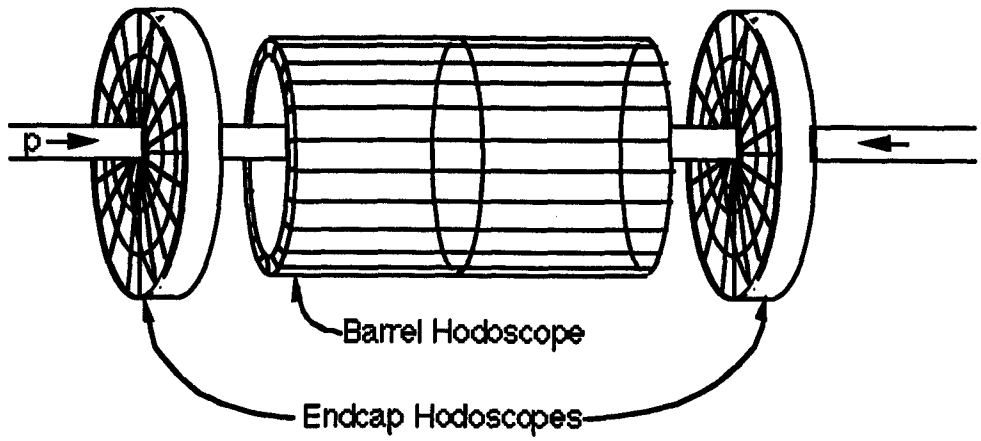

(a.)

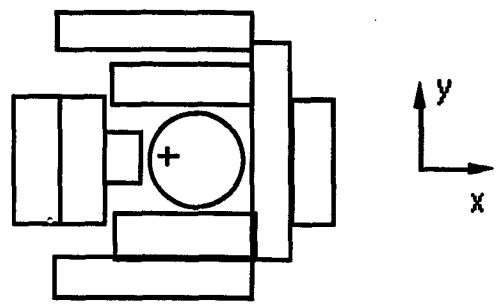

(b.)

Figure 3-10 (a.) Perspective view of the multiplicity hodoscope.
(b.) View of a trigger hodoscope array looking in the $-\hat{z}$ direction

allel to the beamline and is divided longitudinally into two halves of 48 counters each. The barrel system covers the pseudorapidity range $-1.64<\eta<1.64$. Pseudorapidity is given by $\eta=-\ln\tan(\vartheta/2)$, where ϑ is the angle with respect to the +z-direction, which is defined as the direction the protons travel in the Tevatron at the C0 collision region (Appendix A). Azimuthally the barrel system covers 2π except for a window matching the spectrometer aperture. Located upstream and downstream of the barrel hodoscope are the two endcap hodoscopes. Each of these consists of three rings of counters which are situated perpendicular to the beamline. There are 24 counters in each ring bringing the total number of counters in the multiplicity hodoscope to 240. The endcap hodoscope extends the pseudorapidity coverage to $-3.25>\eta>3.25$. Of the 240 multiplicity hodoscope counters, all were equipped with pulse height measurement, but only half were instrumented to measure time. The number of hits in the multiplicity hodoscope, N_h, was converted to a true charged multiplicity, N_c based on Monte Carlo studies. These studies included the effects of the finite size of the multiplicity counters with respect to multiple hits in a counter and the effects of background.

The spectrometer arm covers the pseudorapidity range $-0.36<\eta<1.0$, with an azimuthal acceptance of 18°. The spectrometer therefore measures the momentum of about 1% of the particles seen by the multiplicity hodoscope. The spectrometer arm is made up of ten drift chambers, two sets of time of flight counters and a dipole magnet. Figure (3-11a) shows the magnet aperture, looking in the x-direction, with the y and z-directions labeled. The center of the magnet is located about 75 cm from the beam in the x-direction, about +15 cm in y and +25 cm in the z-direc-

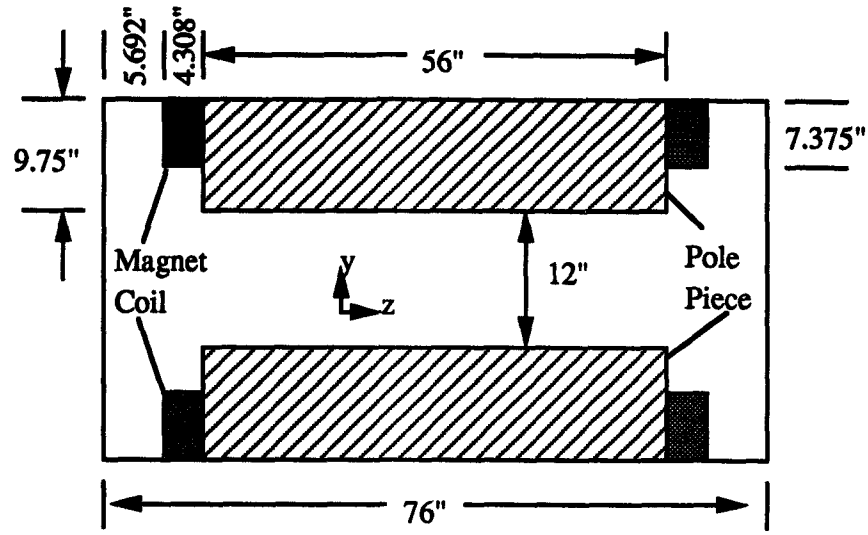

(a.)

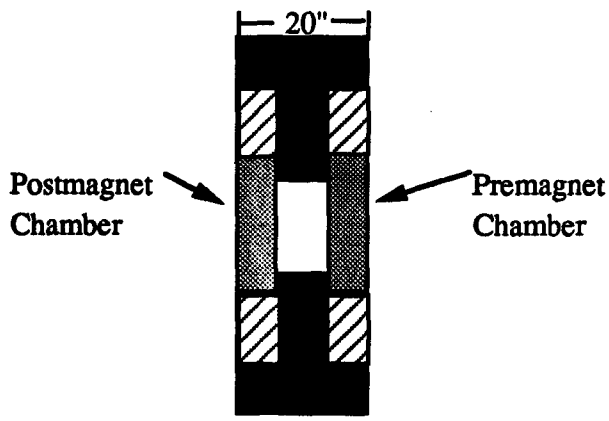

(b.)

Figure 3-11. Two views of the magnet aperture, (a.) looking in the +x direction, (b.) looking in the +z direction showing the premagnet and postmagnet chambers

tion. The vertical distance from pole tip to pole tip is 30 cm and the pole tips are about 141.5 cm long the z-direction. The peak magnetic field is 4 kilogauss and the integrated field strength ($\vec{B} \bullet d\vec{l}$) generates a transverse momentum kick of about 50 MeV/c. Between the interaction point and the magnet are two drift chambers. The first is known as the z-chamber. This chamber contains three planes of 128 wires per plane and is located approximately 15 cm from the beam line. The planes are separated by 1.43 cm in the x-direction and the sense wires within each plane are spaced 8 mm apart in z. The second chamber before the magnet is known as the pre-magnet chamber. This chamber contains four planes of 25 wires and rests against the edge of the pole tip of the magnet. The plane separation for this chamber is 1.9 cm and the wire spacing is 5 cm. It is approximately 55 cm from the beamline. Resting against the other side of the pole tip of the magnet is the post-magnet chamber. This chamber contains four planes of 30 wires and is approximately 85 cm from the beamline. The plane separation and wire spacing for this chamber are the same as that of the pre-magnet chamber. Figure (3-11b) shows the pre-magnet and post-magnet chambers in their location inside the magnet aperture. After the magnet are seven straw drift chambers, each with two staggered rows of tubes (Oh et al. 1990). Counting from the magnet, the even numbered straw chambers contain tubes slanted at four degrees with respect to the vertical for stereo reconstruction. These chambers are discussed in greater detail in the next section. Immediately behind the straw drift chambers is the first of two sets of time of flight counters (Banerjee et al. 1988). Both of these sets of counters are made of the same scintillator as the multiplicity hodoscope, but have

UVT Lucite light guides. In the first set of counters, there are seven of these 300 cm long horizonital scintillators at a distance of about 200 cm. These counters, known as TOF1 are used in particle identification, along with the next, vertical, set of 150 cm long time of flight counters, known as TOF2, located 400 cm from the beamline. In this first running period, only about half of the 32 TOF2 counters were installed and these were present for only part of the run. Therefore these counters were not used in the analysis for this thesis.

Located on the opposite side of the beam pipe from the spectrometer, just outside of the barrel hodoscope were two small straw drift chambers. These chambers, present only in the first running period of E735, were used in conjunction with the trigger hodoscopes to find the interaction vertex. Since there was no magnetic field between these chamber and the interaction point, tracks reconstructed in these chambers could be easily traced back to the beamline to find the z-coordinate of the interaction vertex.

The trigger hodoscopes, which cover the pseudorapidity regions $3< |\eta|<4.5$, are located outside the multiplicity hodoscope, approximately 2 m from the interaction region, one array upstream and one array downstream. These counters are also made of PVT with nonscintillating PVT light guides. Each set of scintillators consists of nine counters which are 2.5 cm thick. The counters range from 33.0 to 58.4 cm wide and from 15.2 to 35.6 cm long. Figure (3-10b) shows the setup of one of these sets of counters. The two sets of scintillators are identical. These two arrays are used in finding the interaction vertex and the interaction time, which is used to cut out background events at the trigger level. All events taken are required to

have at least one hit in each array with an interaction time consistent with a $p\bar{p}$ crossing; this is our minimum bias trigger. In order to get a larger sample of high multiplicity events, an online trigger processor, which scales the number of events in different multiplicity regions, was used. The effects of trigger bias on the acceptance were studied as a function of multiplicity and corrected using a Monte Carlo simulation of the experiment as discussed later.

III. STRAW DRIFT CHAMBERS

The work done for this thesis included the construction of the straw drift chambers used as a part of the spectrometer arm in experiment E735. Straw drift chambers have the advantage of modularity over conventional drift chambers. If a wire breaks in a straw drift chamber, it is easier to isolate and remove the broken wire without affecting other wires in the chamber. Cross-talk is less of a problem in this type of chamber, because of the electrical isolation of each wire. Also, with straw drift chambers, no slope correction has to be made when converting time measurements to hit positions. Located just behind the spectrometer magnet, the straw drift chambers play a major role in tracking for this experiment. In this section, the construction and performance of the straw drift chambers are discussed.

As mentioned in the previous section, seven straw drift chambers are located just after the magnet, when looking from the interaction region. These chambers range in size from 75 cm high x 220 cm long to 110 cm x 340 cm. Figure (3-12) shows schematically a straw drift chamber. In the figure, only a few of the chamber's tubes are shown in order to display the pattern of holes (for tubes) in

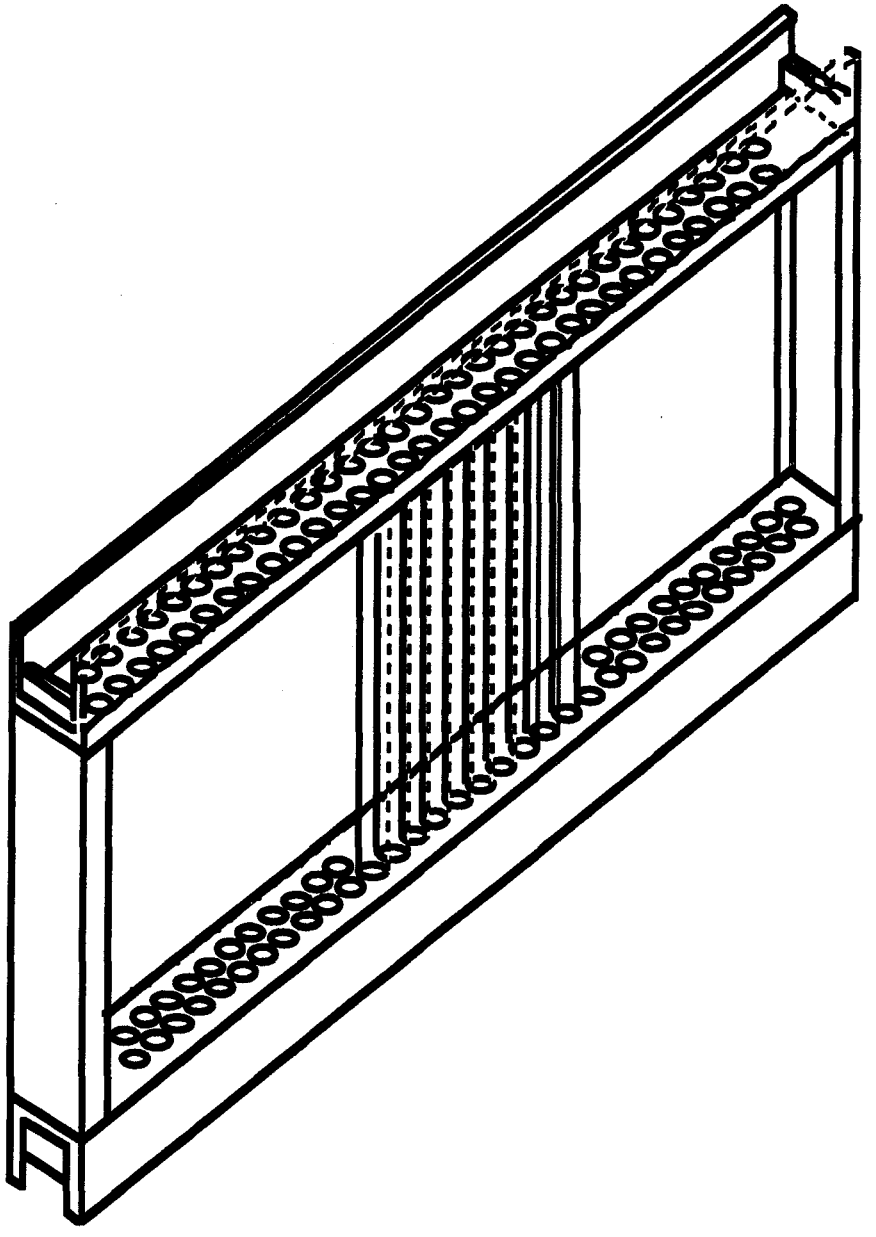

Figure 3-12. Schematic of a straw drift chamber with most of the tubes removed to show the pattern of holes.

the frame. Four of the chambers have vertically oriented tubes and the other three have tubes that are slanted at 4° to the vertical for stereo reconstruction. The chambers with vertically oriented tubes alternate with the slanted tube chambers, with the chamber nearest the magnet having vertical tubes.

The main component of the chambers is 5 cm diameter aluminized mylar tubes (figure 3-13). The tube walls are about 0.04% of a radiation length and are made of 0.018mm of aluminum, 0.075mm of paper and 0.075mm of mylar. Aluminum plates on the top and bottom of the chamber hold the tubes in place. An aluminum plate on each end of the chamber supplies support for the structure and two aluminum plates on both top and bottom protect the tube ends and electronics.

Each chamber contains sixty to ninety holes which have been milled to within 0.1 mm for size and separation between holes. The holes are in two staggered rows. After milling, the center of each hole was measured with respect to a survey point. Aluminum end pieces slide through the holes in the end plates and into the tubes to hold them in place. Hose clamps squeeze the tubes to the end pieces to insure mechanical and electrical connections. Ground cables connect the aluminum end piece to the frame for an electrical ground.

End plugs made of delin are inserted into the aluminum end pieces and feed throughs are inserted into the delin end plugs. Between the feed throughs, 50 micron gold plated copper-beryllium wire is strung at a tension of 0.25 kg. The tension limit on the wire is about 1 kg.

Gas is provided to each tube through 1/4 inch plastic tubing which is inserted in the aluminum end pieces. Sixteen tubes are connected in series in every chamber.

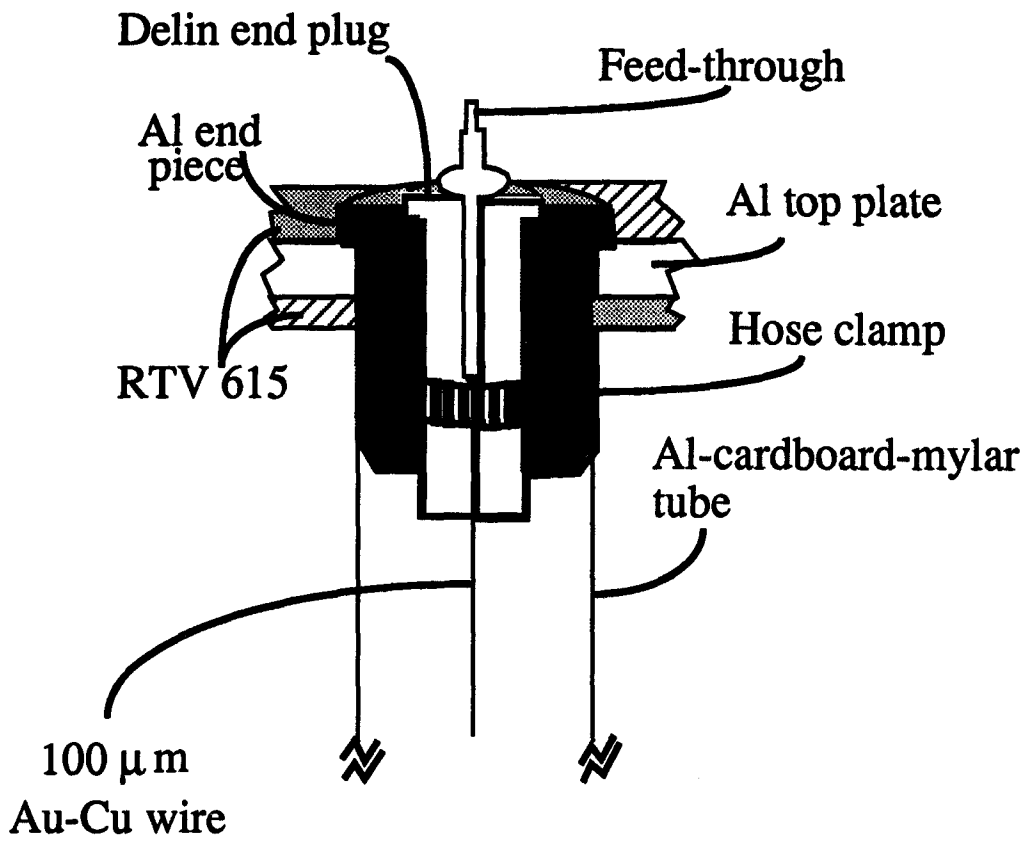

Figure 3-13. Schematic representation of a tube end showing the end piece, the aluminum plate, the gas seal system and the wiring system.

Each group of sixteen is supplied by its own gas line. This is in order to minimize the number of contaminated tubes in case a leak develops. During normal data taking, each chamber has a gas flow rate of 1 ft^3/hr. Gas seal around the ends of the tubes and the aluminum end pieces is provided by low viscosity RTV-615. RTV-615 is poured on each side of the aluminum end plates in a manner such that the tube ends and most of the aluminum end pieces are completely covered. RTV-112 is used to accomplish the gas seal around the feed throughs and the gas lines.

Since C0 has no overpass for the main ring beam line and since the aborts for both the main ring and the tevatron are located at C0, it was expected that the radiation levels the chambers would be exposed to would be high. Therefore, radiation tests were performed on a prototype consisting of a single tube. The prototype was exposed to an intense source (Sr^{90}) such that the current draw was about 1 microampere/cm. Although both argon-methane (90-10) and argon-ethane (50-50) were tested for use in the chambers, argon-ethane was used for the radiation tests, because of the high hydrocarbon content which has been found to be responsible for chamber aging.

The prototype was exposed for four months. During this time, current draw, singles rate and the plateau were checked periodically. These quantities were found to remain constant over the period of the test. After the test, the tube of the prototype was opened and examined for signs of aging such as whisker growth. No signs of deterioration were found.

As was mentioned above, both argon-methane (90-10) and argon-ethane (50-50) were tested for use in the straw drift chambers. Although better resolution

was attained using argon-ethane (better by about 20%) argon-methane was used during the first run of E735 because of safety considerations. Cosmic rays were used to measure the resolution. A coincidence signal form two scintillators, one on each side of a chamber, is used as a trigger to start the TDC. The measured drift velocity as a function of electric field is used to convert the drift time to a distance from the wire. Next the tracks were reconstructed, using the method discussed later, and the residuals were calculated. From the residuals, the measured resolution of the straw drift chambers is about 200 microns (figure 3-14). The efficiency of the track finding algorithm was studied by scanning about 1000 events by eye. The results are then compared with the results of the reconstruction program. With the algorithm described in chapter IV, it was determined that tracks are reconstructed in the straw drift chambers about 95% of the time. The Monte Carlo simulation described in the next chapter also was used to study the track reconstruction efficiency. The efficiency from the Monte Carlo simulation was consistent with the value quoted above.

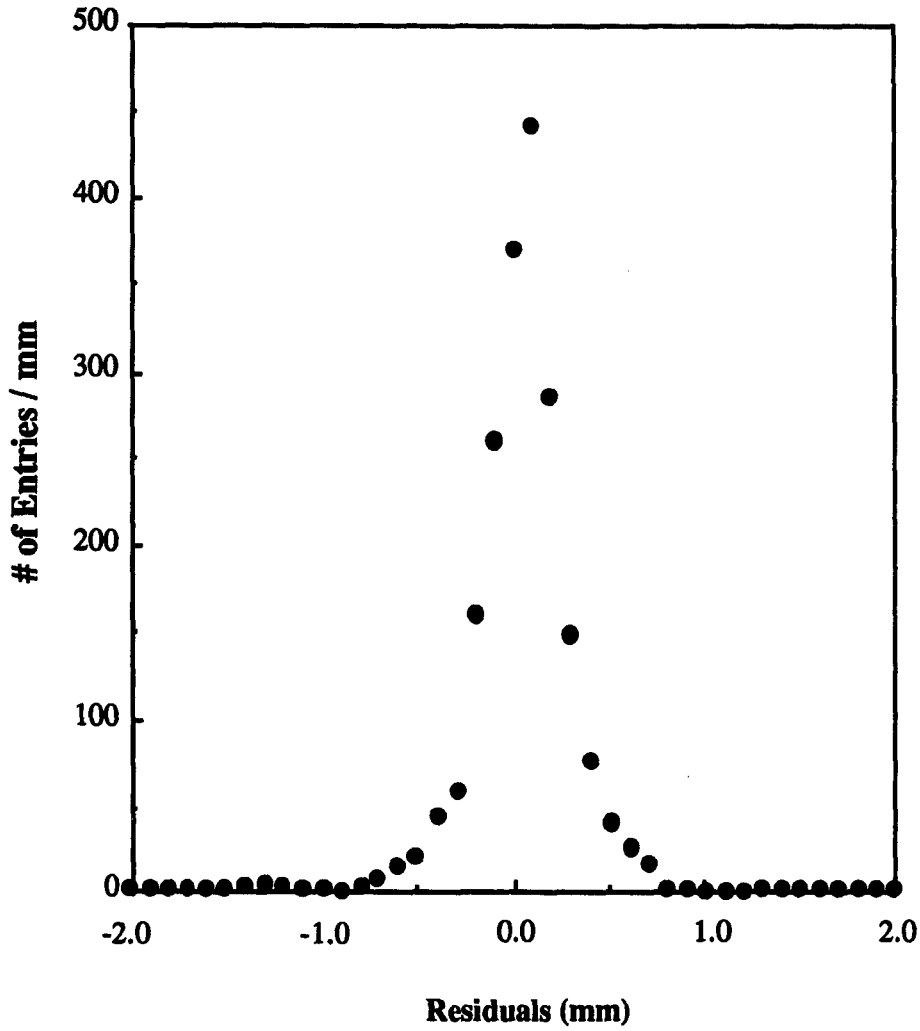

Figure 3-14. Residuals for the Straw Drift Chambers using 90% argon-10% methane gas.

IV. DATA ACQUISITION

This section deals with the collection of data for the experiment. The various stages in the flow of the data from the detector to magnet tape will be discussed, including the basic triggering requirements for an event and online rejection of unwanted interactions. Finally, the different types of triggers, other than the minimum bias trigger, will be presented.

Except for the z-chamber, pre-magnet chamber and post-magnet chamber, data from each component of the detector was read out through a single Camac branch by a PDP 11/45. Data from the z-chamber, pre-magnet chamber and post magnet chamber were read out through FASTBUS by a PDP 11/50. From the PDP's, events were sent to a VAX 750 over DR11-W links. Here the two parts of an event were combined into one array. This was accomplished by matching the event numbers from the event time clock (ETC). The ETC is an event counter which is read by both the PDP 11/45 and the PDP 11/50.

The Fermilab data acquisition package VAXONLINE was used for computer control. By communicating with the RSX DA system on the PDP's, this package

coordinated the starting and stopping of data taking by the PDP's, received and concatenated the events from the PDP's, and maintained a "pool" of events which could be accessed to write an event to tape or for online monitoring of the experiment by different programs. Also using this package, another type of "event" was periodically written to the data tapes. This "event" was an array containing information about the performance of the accelerator at the time. Figure (3-15) shows the path taken by the data through the system.

Online monitoring was accomplished using a program called Mon. Mon sampled concatenated events from the event pool and generated histograms of hits per counter and hits per event for a given detector component. Scanning on an event by event basis, for instance to check the number of tracks in the spectrometer per event, was accomplished by using the event display option present in Mon. Two dimensional scatter plots of the time an upstream counter was hit versus the time a downstream counter was hit for combinations of trigger-hodoscope counters and for combinations of multiplicity hodoscope counters were used to determine and check the timing for the various triggers.

Each magnetic tape contains at least one "run", where a run is defined as the data taken between the time the PDP's DA system is started and when it is stopped for any reason. In general the data acquisition rate for a given run was about 10 Hz out of an interaction rate of ≈100 Hz with three proton and three antiproton bunches in the Tevatron. The time spent by the DA system processing an event was known as dead time since any triggers which arrived during this time were vetoed. For our trigger rate of 10 Hz, the experiment was ready to take data

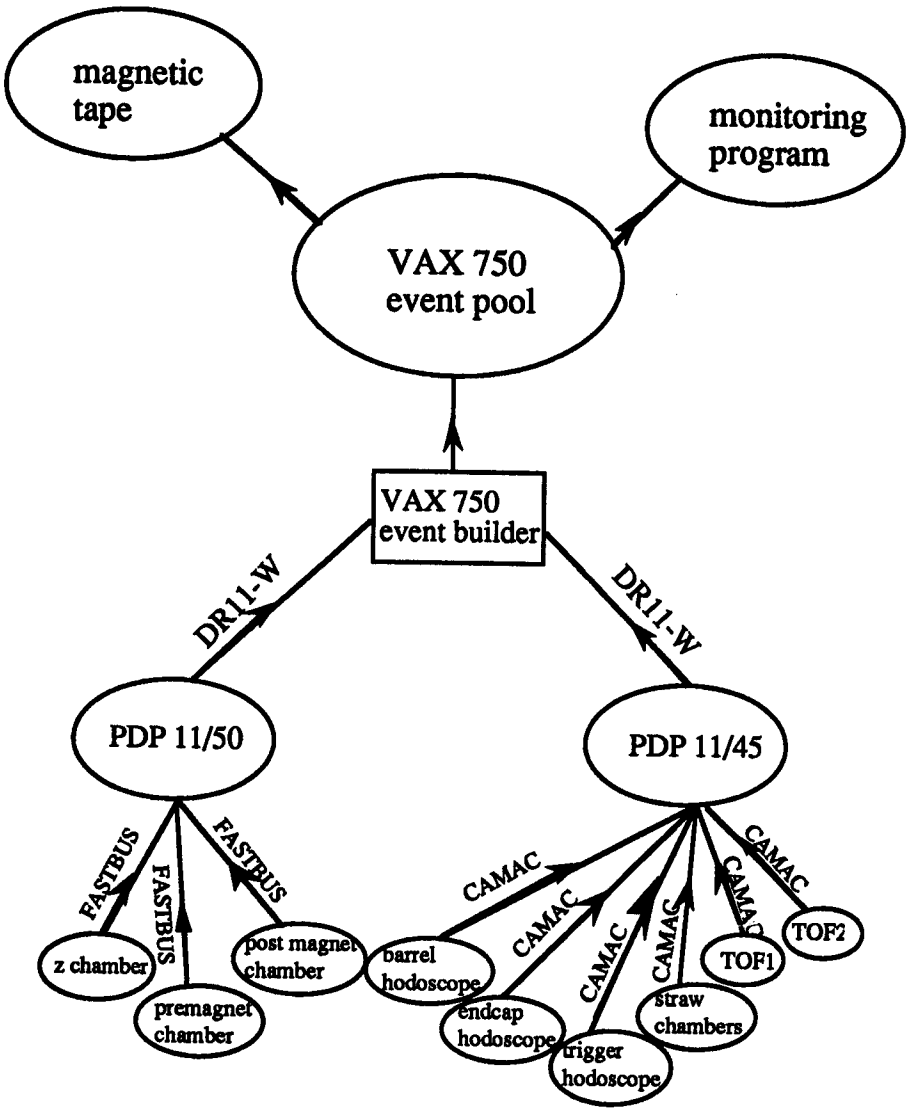

Figure 3-15. Flow of data through the acquisition system.

(i.e. the DA system was not processing an event) about 80% of the time.

As mentioned previously in this chapter, there is no main ring overpass at C0, so the main ring beam pipe is only about 60 cm above the Tevatron beam pipe. When beam was stored in the Tevatron, the main ring often was being used to produce antiprotons. Losses from the main ring were relatively high when protons were injected and when acceleration began. During this part of a main ring cycle, the DA system was inactive to avoid main ring background. Also during this time, the voltages were lowered for scintillators and chambers closest to the main ring to avoid damage from high currents. The main ring gate lasted 1.0 second of the 2.4 second main ring cycle, so the main ring prevented data taking about 40% of the time.

The first step in getting data to tape is to determine when an event of the desired type has occurred. In this case, the desired type of event is an interaction between a proton, from one of the main proton bunches, and an antiproton, from one of the main antiproton bunches, as the bunches cross in the interaction region. Preceding and trailing each bunch, are satellite bunches. Interactions involving these satellites must be removed from the data sample. Other sources of background include beam scraping the beam pipe, a limiting aperture or a magnet. All sources of background will be referred to as beam-gas background. Offline methods used to veto these events will be discussed in a later chapter, but in this chapter we deal with online methods of event selection.

The most basic trigger, for a colliding beam experiment, occurs whenever a proton bunch and an antiproton bunch cross the interaction region. This signal,

known as T0, is supplied by the Tevatron Beam Synchronous clock (TBS). Whenever the bunches pass each other at F0, the region directly across the accelerator ring from C0, a signal is generated and supplied to C0 by TBS. This signal, with appropriate delays, is used to generate TDC starts, ADC gates, fast clear signals and the beam crossing trigger, T0. All other triggers were timed to be in coincidence with T0.

The trigger hodoscopes were responsible for the next level of triggering. When hits were detected in each trigger hodoscope array within the beam crossing time, a trigger known as a beam-beam trigger (BB) was generated. This trigger required the difference in the time of the earliest hit in each trigger array to be <5ns. These hits were also required to occur during the beam crossing time as defined by T0.

In order to make this trigger cleaner, vetoes were added. The first was an early time veto (ETV). This removed events in which either array had a counter hit before the bunch crossing. This excluded background events involving the main bunches which occurred before they reached the interaction region, either interacting with satellites or gas particles inside the beam pipe. This veto also removed events in which early satellites interacted with gas particles, main bunch particles or other early satellites. The other veto is aimed at trailing satellite particles which interact before reaching the trigger array. This veto excludes an event when the upstream trigger array was hit ≈14ns before the downstream trigger array (the two trigger arrays are separated by ≈14ns). This was known as the satellite beam gas veto (SBG).

When the luminosity was relatively low, another veto was added. This ex-

cluded events in which only one counter was hit in the upstream trigger array. This was to remove beam gas events involving protons in the main bunch-gas particle interactions, in which few particles were produced in the backward (-z) direction. This type of event dominated at low luminosities. This requirement, which was achieved through the trigger processor, was known as Pbar>1.

The combination T0*BB*ETV*SBG*Pbar>1 was known as the standard trigger (ST). However, the combination T0*BB*ETV*SBG was used more frequently and became know as the standard trigger minus Pbar>1 or more simply as PT. Most triggers, especially those from later in the run used the combination known as PT as a part of the trigger.

The other components used in the trigger were used to enhance the probability of taking a certain type of event. For example, a TOF1 trigger was used in order to enhance the number of events with tracks in the spectrometer. This was done by requiring at least one hit in the first time of flight array. In general, this trigger was used in conjunction with either ST or PT. A series of enhancement triggers, the TPB series (e.g., TPB1, TPB2...), made use of the trigger processor to take a larger percentage of events with high multiplicity. This series used the number of hits in the barrel hodoscope obtained by the trigger processor. Events were classified as belonging to different barrel hodoscope multiplicity regions and the fraction of events which were accepted in each region was scaled according to a preset factor. For instance every high multiplicity event (>50 hits in the barrel hodoscope for TPB1) was taken, while (also for TPB1) only 1 event out of every 2 was taken for barrel hodoscope multiplicities between 38 and 49, with a lower per-

centage of low multiplicity events taken. In this way, at higher luminosities, most of the high multiplicity events could be taken without increasing the trigger rate or the dead time.

Chapter 4

Data Analysis

The data went from the original tapes to the data summary tapes (DST's) in three stages. The first step was a zero suppression which compressed the data by a factor of approximately three. In the second step, detector calibration was performed including pedestal subtraction for hodoscope ADC's and time to distance conversion for drift chamber hits. The final stage was where the actual DST's were written. Track reconstruction was accomplished in this stage, including the calculation of the momentum and path length of tracks for use in particle identification in conjunction with the time of flight system. Also, the vertex was

calculated from the trigger hodoscope arrays and, independently, from the tunnel straw drift chambers. These two vertices were then used to find an event vertex based on the conditions under which each vertex was found. If one vertex was obviously better than the other, it was used. Otherwise the average of the two was used.

In this chapter, the track reconstruction method will be discussed with special attention given to the method used to find a track's momentum. Following this discussion, background events will be the focus. In the previous chapter, we looked at the online vetoes used to remove background events at the trigger level. In this chapter, we examine the offline cuts used for this purpose. Then we will discuss track selection.

The topic of the second section of this chapter is the method used to identify Λ's and $\bar{\Lambda}$'s. Included in this discussion are the method used in identifying protons and the cuts used to enhance the signal to noise ratio. In the final section, the acceptance corrections and the Monte Carlo simulation from which they were generated are discussed. This discussion will also look at the invariant mass width of the Λ peak obtained from the simulation.

I. Data Reduction

Track reconstruction begins in the straw drift chamber which is located the farthest from the interaction point. For the first part of the search, only the planes with vertical tubes are considered. Two hits, one of which must be in the last three planes of vertical tubes, are used to begin a track search. Due to the geometry of the straws, a hit in these chambers gives a circle which represents the closest approach of the particle to the wire. Using two hits, there are four possible lines which are tangential to both circles (figure 4-1). Since there is a negligible magnetic field in the last few straw drift chambers, the search for tracks can start in these chambers by looking for straight tracks. An attempt is made to associate hits in other planes, closer to the interaction point, with each of the four tracks obtained from the two hits being used. Of the four possibilities, any track with four or more hits is kept for further processing. If more than one track meets this requirement,

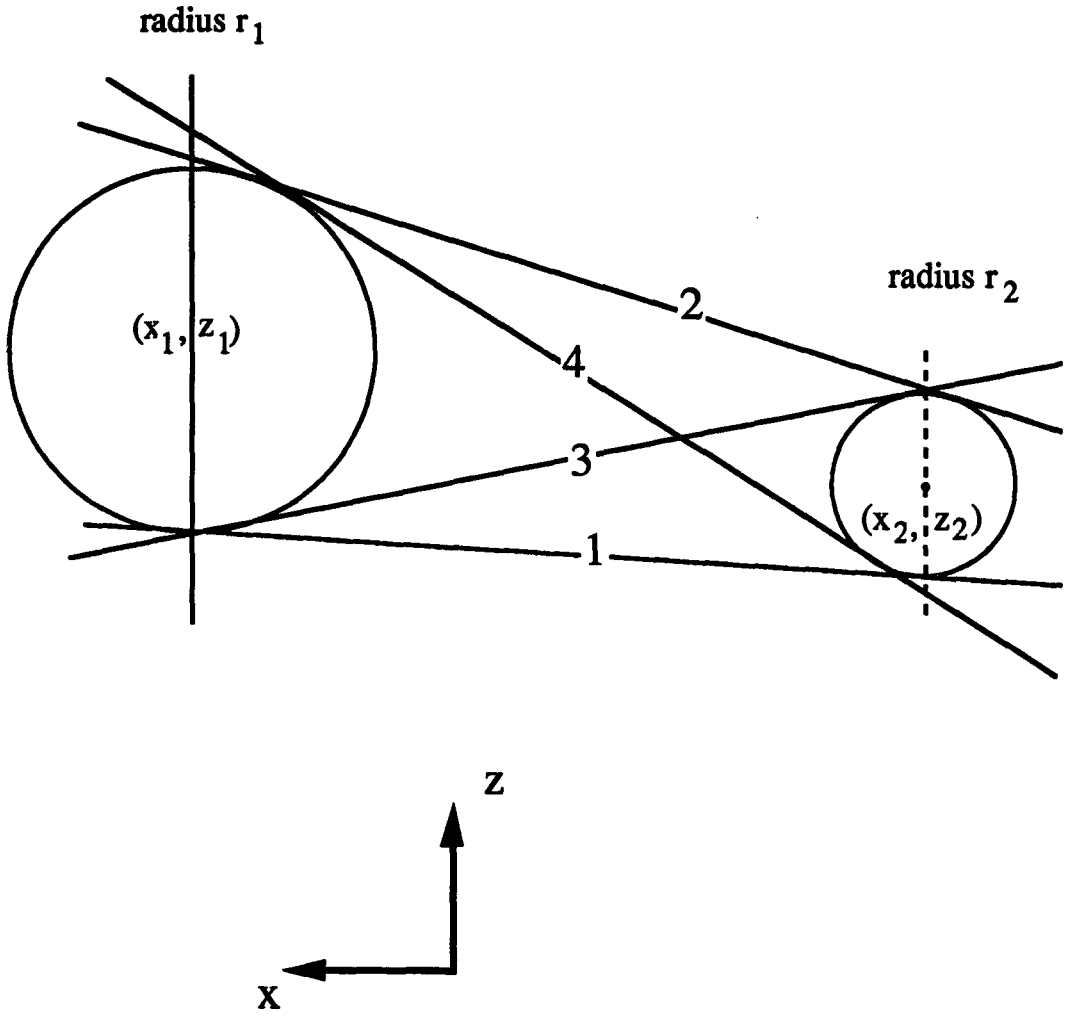

Figure 4-1. Four possible tangential lines generated using two circles corresponding to two hits in the straw drift chambers.

then the candidate with the lowest χ^2 per degree of freedom is kept. This initial search, done in the x-z plane, uses only straw drift chambers 3, 5 and 7 (the last three chambers with vertical tubes). After finding a possible track in these chambers, hits in straw drift chambers 2, 4 and 6 (the chambers with wires tilted at 4 degrees with respect to the vertical) are matched to the track in order to find y information.

When four or more colinear hits are found in the last six vertical planes of tubes, an attempt is made to associate hits in straw drift chamber 1 with this track. A momentum estimate is obtained by assuming the track originated at the event vertex. Using this assumption, an estimate of the angle of deflection is obtained. From this the momentum of the track is estimated. This momentum estimate is used to swim the track in order to pick up hits in the first chamber (the straw chamber closest to the magnet). Another iteration, associating hits in slanted chambers for y information, estimating the momentum from the new quadratic fit and swimming through the field to find hits in vertical chambers close to magnet, is preformed. Next, if the track has a χ^2 per degree of freedom of less than 4.0, the hits in the straw chambers associated with this track are deleted from the array of hits so that they are not used in other tracks.

The momentum estimate obtained from the track reconstructed in the straw drift chambers is used to swim the track through the magnet, in an attempt to pick up hits in the pre-magnet and post-magnet chambers. If hits in these chambers are successfully associated with the track, then these points, along with the straw

drift chamber points, are fitted with a cubic spline to find a new estimate for the momentum. The new momemtum estimate is used to try to pick up hits in the z-chamber.

When attempts have been made to associate hits in all twenty-two planes of the spectrometer arm tracking chambers with the candidate track, another iteration on the fit is made and the χ^2 per degree of freedom is checked to see if it is less than 3.0. If the χ^2 per degree of freedom is greater than 3.0, then the worst point (farthest from the fit) on the track is deleted and the track is refit and checked for improvement in the χ^2. If χ^2 is still greater than 3.0, the next worst point is also deleted and the track is fit a final time.

A cubic spline fit is used for the track whenever the points used include hits in more than just the straw drift chambers. The advantage of this method over step by step tracking through the magnetic field is the speed of the convergence for the spline fit (Wind, 1973). In this method, a cubic spline is used as the model for the track. The cubic spline is continous through the second derivative which, multiplied by the momentum, is given by the formulae:

$$F(x) = py'' = \sqrt{1 + y'^2 + z'^2}\left(B_x z' + B_y y' z' - B_z\left(1 + y'^2\right)\right) \quad (4-1)$$

and

$$G(x) = pz'' = \sqrt{1 + y'^2 + z'^2}\left(-B_x y' + B_z y' z' - B_y\left(1 + z'^2\right)\right) \quad (4-2)$$

which are obtained from the equations of motion of a particle in a magnetic field

(Appendix B). Numerically integrating these expressions twice gives an expression for the track which is continous through the second derivative. That is, there is still a constant term and a term linear in x to be found. This can be represented by:

$$y = a_1 + a_2 x + \frac{Y(x)}{p} \qquad (4-3)$$

and a similar expression for z, where Y(x) is the double integral of F(x). A least squares fit is then performed in order to find the y-intercept (a_1), slope (a_2), z-intercept, z-slope and momentum for the track. This involves inverting a 5x5 matrix in order to minimize the χ^2. If the resulting fit is not yet satisfactory, the parameters are used in the next iteration as input. Figure (4-2) shows an event fully reconstructed in the spectrometer arm.

When track reconstruction is complete, we have three classes of tracks. Tracks that do not pass the χ^2 per degrees of freedom cut above are an example of the first class. This type includes tracks that have a fitted momentum error greater than $2\Delta p$, where Δp is obtained from a fit to the momentum error of tracks in a Monte Carlo simulation of the detector and is parametrized by the formula (T. Alexopolous, et al, 1988):

$$\frac{\Delta p}{p} = \sqrt{0.0016 * p^2 + \frac{0.0016}{\beta^2}} \qquad (4-4)$$

where $\beta = \frac{v}{c}$ and p is in GeV/c. Also in this group are tracks with no hits in the

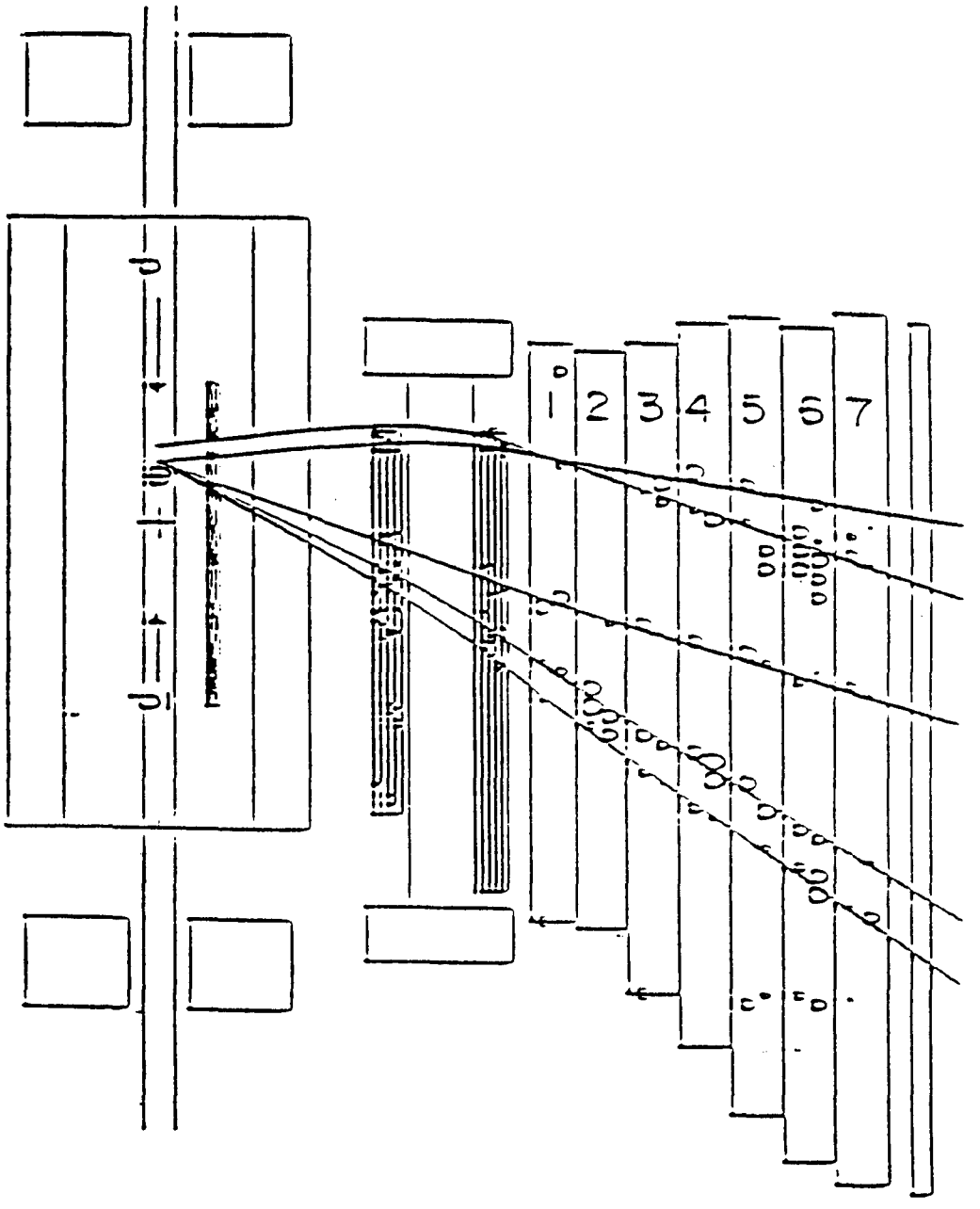

Figure 4-2. Top view of a five track event fully reconstructed in the spectrometer arm.

pre-magnet chamber. This class of track is not used in this analysis.

The second class of track has passed the χ^2 per degrees of freedom cut and the fitted momentum error cut, but failed to obtain reliable y information from straw drift chambers 2, 4 and 6. These tracks are given a y-slope and intercept which correspond to a track originating at y=0 and going through the center (in the y-direction) of the magnet.

The final class of track is a "good" track. This track has passed the χ^2 per degree of freedom cut and the fitted momentum error cut; unlike the second class this class has reliable y information from straw drift chambers 2, 4 and 6.

For this thesis, all "good" tracks were used in the analysis. Additionally, in order to increase the statistics for this analysis, tracks in the second class were also used (this is possible since the major component of the magnetic field is in the y-direction.).

Both through online trigger vetoes and through offline cuts in the analysis programs, efforts were made to increase the ratio of good events to background events. Using stores with one or more of the three antiproton bunches missing, characteristics of background events (including timing in the hodoscope and forward-backward assymetries) were investigated. As was previously mentioned, one source of background events was interactions between particles in the beam and molecules of the gas inside the vacuum pipe. Other sources of background events include beam scraping the beam pipe, a limiting aperture or a magnet.

Beam-gas background events can be divided into two categories-main bunch beam-gas and satellite beam-gas. Of the two, main bunch beam-gas is the

larger background due to the higher intensities in the main bunches. Satellite beam-gas involves smaller groups of protons or antiprotons (satellite bunches). During the first run, the intensities of the proton bunches were 10 to 20 times greater than the antiproton intensities, causing proton beam-gas to dominate the background events.

Online trigger requirements, discussed in the last chapter, removed some of the beam-gas background at the trigger level. However, some background events which occurred between the trigger hodoscope arrays were able to pass the online cuts and had to be removed offline. Online, the emphasis was on using the trigger hodoscopes. Offline, the emphasis switched to the multiplicity hodoscope for removing background events. Events which were obtained when a proton bunch crossed the interaction region without a corresponding antiproton bunch were assumed to be representative of the background. These events were used to devise methods to remove beam-gas events. Since the beam-gas events are essentially fixed target events, most of the products of the interaction travel in the direction of the incident beam particle with few particles traveling in the backward direction. Figure (4-3) shows the number of hits in the upstream and downstream trigger hodoscopes for events obtained when only a proton bunch was present (beam-gas events) and events obtained when both a proton and an antiproton bunch were present (beam-gas and beam-beam events). This shows that the peak at number of hits equals 1 is due to beam-gas events. Requiring two or more hits in both trigger hodoscopes was effective in removing much of the background.

In order to remove more background events the asymmetric nature of these

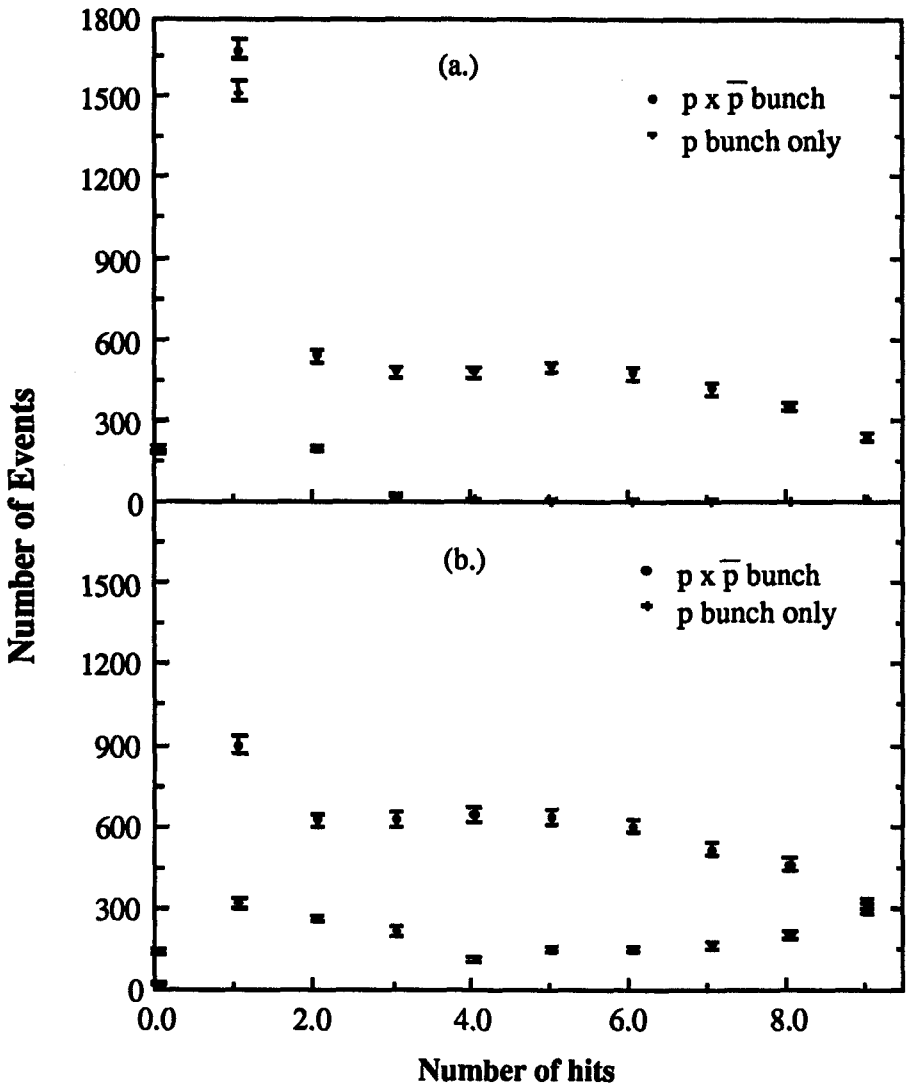

Figure 4-3. The number of hits in (a.) the upstream and (b.) the downstream trigger hodoscopes for events when only a proton bunch is present and when both a proton and an antiproton bunch are present.

events was used once again. A variable to measure the degree of asymmetry for an event was defined;

$$A = \frac{(N_{ue} - N_{de})}{(N_{ue} + N_{de})} \qquad (4-5)$$

where A is the asymmetry variable, N_{ue} is the number of hits in the upstream endcap hodoscope and N_{de} is the number of hits in the downstream endcap hodoscope. Again, because beam-gas events are fixed target events, most of the produced particles tend to be found in the forward direction. For events with a multiplicity greater than 80, the cut was used, requiring |A| to be less than 0.6. In figure (4-4), A is plotted with the cuts marked.

Beam-gas events also appeared in the timing for the innermost ring of the endcap hodoscope. If a plot is made of the TDC values for an upstream counter versus the TDC value for a downstream counter for all combinations of counters in the inner ring of the endcap hodoscopes, six areas develop in which the density is high (figure 4-5). The largest of these areas corresponds to the normal beam-beam event timing. The other five areas correspond to different types of beam-gas background. Figure (4-6) shows the types of beam-gas events which pass timing cuts imposed online on the trigger hodoscopes. These beam-gas events show up in the five regions in the timing for the endcap hodoscopes.

The area of high concentration in figure (4-5) in which the time for the up-stream counters is similar to that of a good beam-beam event, but the time for the

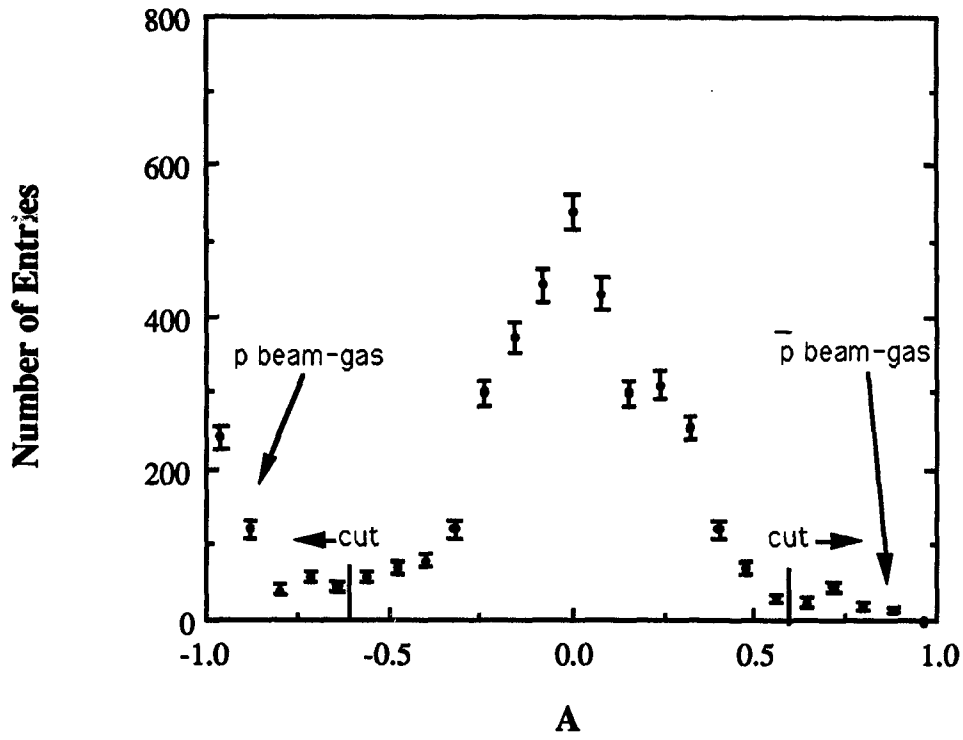

Figure 4-4. Plot of the assymetry variable, $A=(N_{ue}-N_{de})/(N_{ue}+N_{de})$, showing the beam-gas cuts. Also shown are the proton beam-gas region ($A<-0.6$) and the $\bar{p}$ beam-gas region ($A>0.6$).

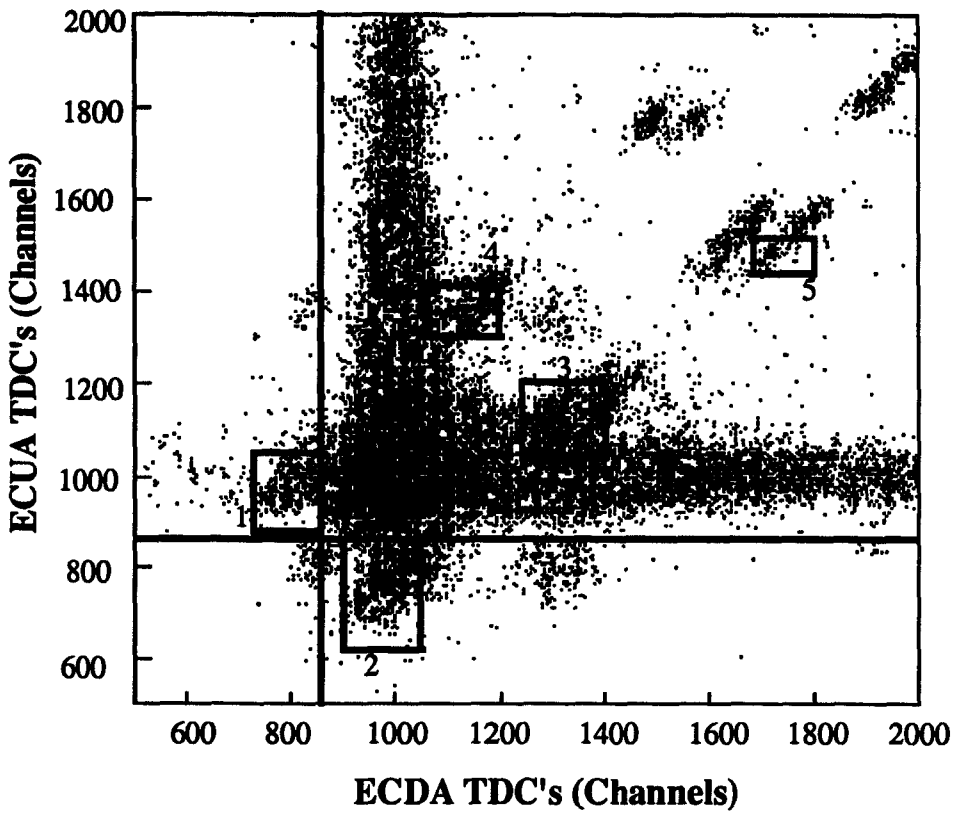

Figure 4-5. Endcap hodoscope upstream TDC's versus endcap hodoscope downstream TDC's (inner ring only for both) before beam-gas cuts. Beam-gas cuts are indicated by boxes.

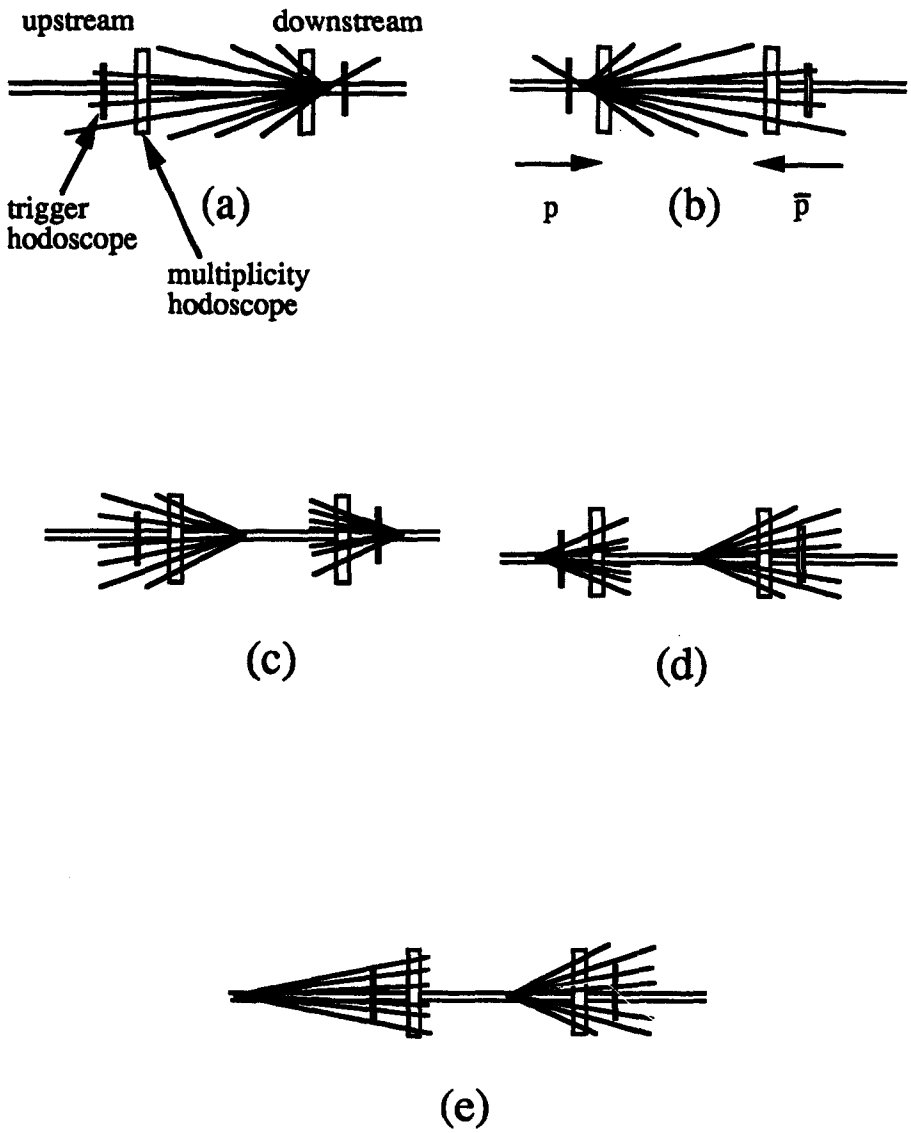

Figure 4-6. Examples of background events which pass the online cuts using the trigger hodoscope, but are eliminated by offline cuts using the endcap hodoscope.

downstream counters is early, corresponds to a beam-gas event involving a main bunch which occurred between the downstream endcap hodoscope array and the pbar counters as shown in figure (4-6 a). This corresponds to the box marked "1" in figure (4-5). Figure (4-6 b) shows an event, corresponding to the box marked "2" in figure (4-5), also involving a main bunch, which occurs between the upstream endcap hodoscope array and the p counters. This event would have early hits in the upstream array and hits in the downstream array in time with beam-beam events. In figures (4-6 c) and (4-6 d), two interactions occur during one crossing, one interaction involves a main bunch in a possible beam-beam event while the other involves a satellite bunch in a beam-gas event. The satellite event would cause late hits in the array closest to beam-gas interaction point. So figure (4-6 c) would have late hits in the downstream array, while figure (4-6 d) would have late hits in the upstream array. Events of the type depicted in figure (4-6 c) would show up in the box marked "3" in figure (4-5), while events like that in figure (4-6 d) would be in box "4". The last area of high concentration is also caused by two interactions during one crossing. Figure (4-6 e) shows an event which would populate the fifth heavily concentrated area (the box marked "5" in figure (4-5)). Events in this area involve a normal beam-beam event along with a beam gas event involving the second trailing satellite for the proton bunch. This second trailing satellite interaction occurs upstream of the detector and therefore generates late hits in both the upstream and downstream arrays.

Figure (4-7) shows the same plot as figure (4-5) after the timing cuts have been imposed. It is estimated that after these offline cuts have been made, ap-

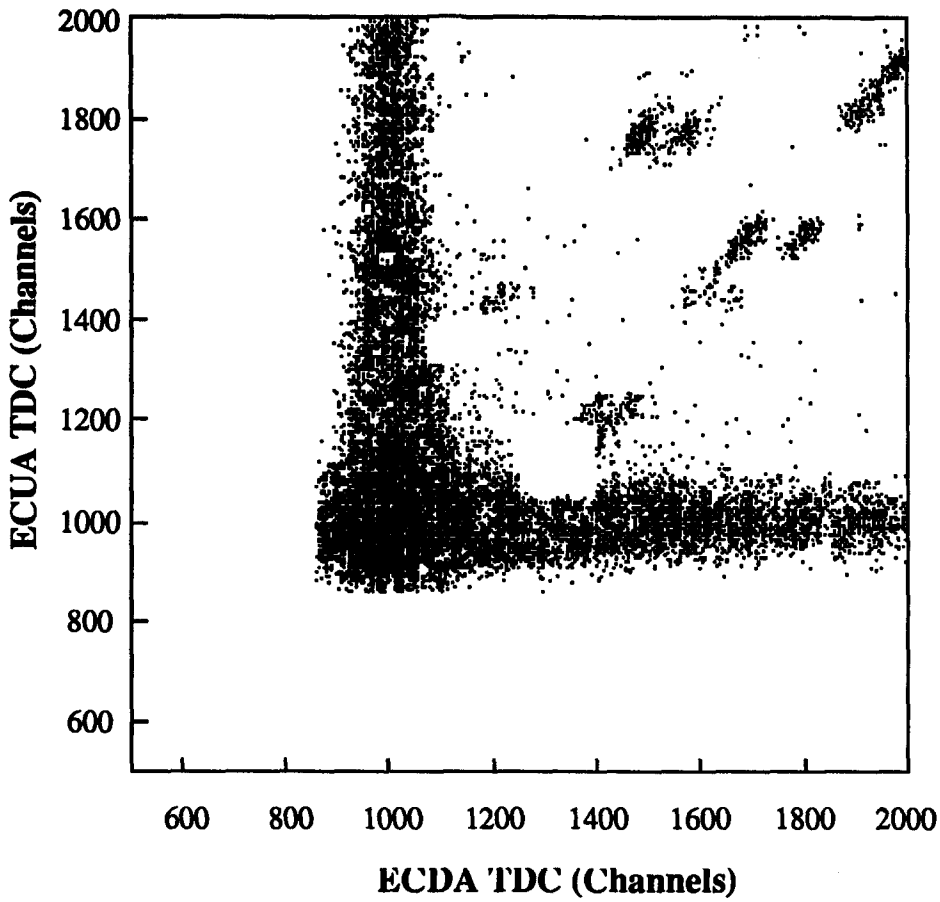

Figure 4-7. Endcap hodoscope upstream TDC's versus endcap hodoscope downstream TDC's (inner ring only for both) after beam-gas cuts.

proximately 2% of the remaining events are from beam-gas.

Even when a true $\bar{p}p$ interaction occurs, not all tracks which are found in the spectrometer arm are from this interaction. Background tracks in the data come predominately from secondary interactions in the beam pipe, the concrete surrounding the interaction region and the magnets. These tracks had to be removed from the data.

After tracks were reconstructed, those which passed the χ^2 and momentum error cuts were rejected if the fitted momentum was less than 150 MeV/c because of poor track reconstruction efficiency and contamination from secondary (background) tracks. Single charged tracks were required to originate at the event vertex. This condition, discussed below, was not used in the selection of Λ candidates, but were used in this thesis for the analysis of individual proton and all charged track samples. Figure (4-8) shows the y-intercept at the beam line (x=0) for tracks in spectrometer arm. Tracks were required to have a y-intercept less than ± 10 cm at the beam line. Although the y-position of the beam is known to better than a few millimeters, the poor y-resolution of the spectrometer arm necessitates the 10 cm cut. Those tracks that survived these requirements were subjected to cuts requiring that each track came from the vertex as determined by the trigger hodoscope and the tunnel straw chambers. In figure (4-9), the difference between the event vertex (Z_{ev}) and the track vertex (Z_{tr}) along the beamline is plotted. The RMS error in the event vertex has been found to be less than 5 cm. For events with more than one track, if the z-verticies of the tracks are within 2 cm of each other at the beam line the tracks were determined to have intersected. The

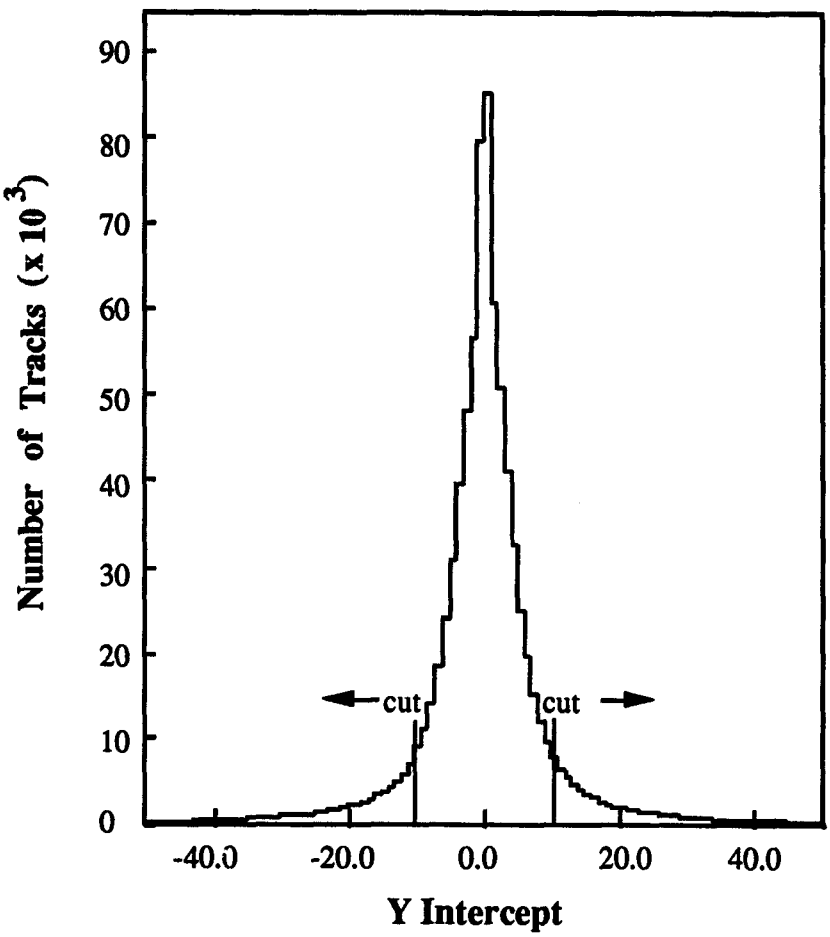

Figure 4-8. The distribution of y intercepts at the beam line (x=0) for all tracks. Also shown are the cuts made at y intercept equals ± 10 cm to remove background tracks.

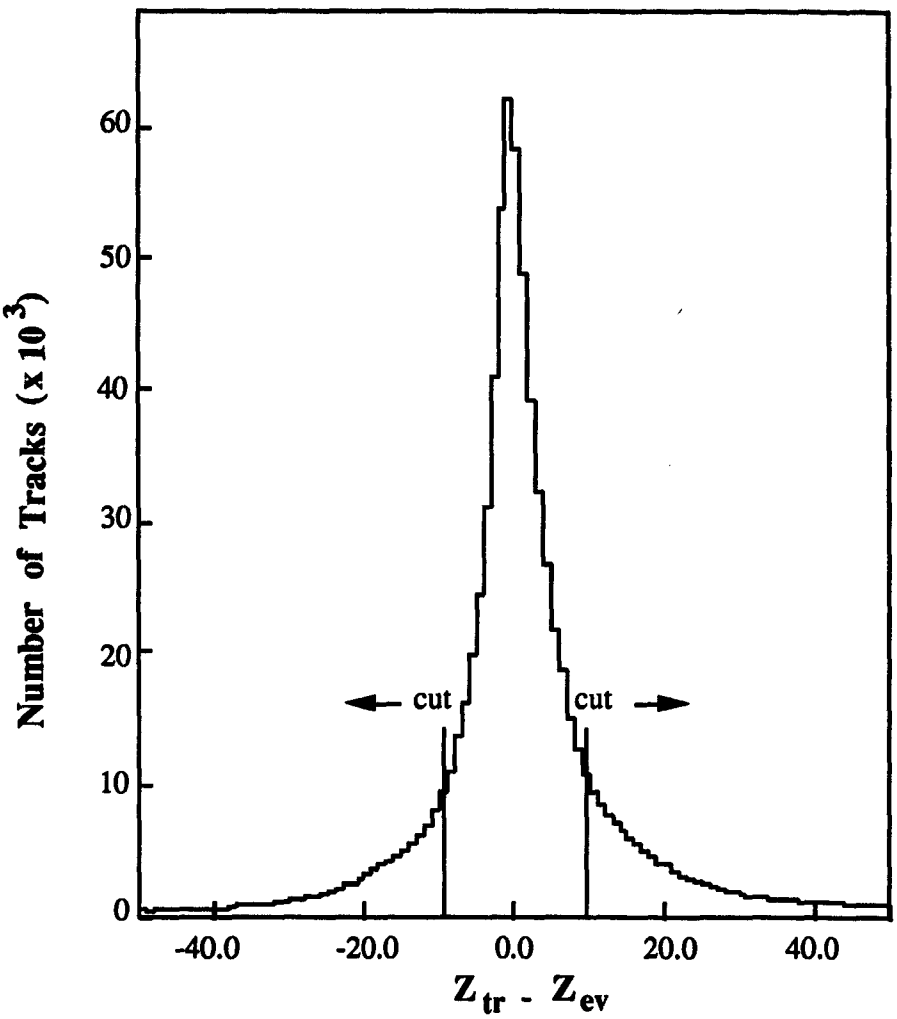

Figure 4-9. The distribution of the difference between the track vertex (Z_{tr}) and the event vertex (Z_{ev}) for all tracks. Also shown are the cuts made at Z_{tr}-Z_{ev} equals $\pm$ 10 cm to remove background tracks.

average z-vertex for intersecting tracks was required to be within 10 cm of the event vertex. For events with multiple spectrometer arm tracks in which no intersecting tracks were found, the track which had a z-vertex closest to the event vertex was accepted if the difference was less than 10 cm. For events with a single track, the track was accepted if $|Z_{ev}-Z_{tr}|$ was less than 10 cm. It is estimated that less than 10% of the tracks which pass these requirements are background tracks.

II. Λ^0 and $\overline{\Lambda}^0$ Identification

Of the possible decay modes of the Λ, the useful one for this detector is $\Lambda \rightarrow p^+ \pi^- \ (\bar{\Lambda} \rightarrow p^- \pi^+)$. The signature corresponding to this decay was two charged particles in the spectrometer arm. Therefore, from the data summary tapes, which were discussed earlier in this chapter, events in which two or more good tracks were present in the spectrometer arm were written to "mini" data summary tapes for use in this analysis. Of the three types of tracks mentioned earlier, for this analysis, a track was considered good if it passed the χ^2, momentum error and minimum momentum cuts mentioned previously and had at least three hits in the pre-magnet chamber associated with it.

Using the momentum obtained from the magnetic spectrometer arm along with the time of flight from the TOF system, a mass was calculated for each

particle. In chapter 3, the time of flight system, which consists of the trigger hodoscopes, TOF1 and TOF2, was described. As mentioned in that chapter, TOF2 was not in place for the entire run and when it was in place, only half of the array was present. For this reason, TOF1 was used in conjunction with the trigger hodoscopes to obtain a time of flight for each particle. The process of finding a time of flight begins with the trigger hodoscopes.

In addition to being used as an event trigger, the trigger hodoscopes were also used to find an interaction time, t_0, for the event. To find t_0, the counter in the proton array with the earliest hit is used along with the earliest hit in the pbar array of the trigger hodoscope. It is assumed that these "early" particles from the interaction are traveling close enough to the speed of light that the difference can be ignored. For a counter of length ℓ, with an index of refraction n, t_0 is given in terms of the time, t_1, obtained from one end of the counter after calibration and subtraction of the cable length by (see figure 4-10)

$$t_0 = t_1 - \left(\frac{\ell}{2} + x\right)\frac{n}{c} - \frac{d}{c} \qquad (4-6)$$

and for the other end

$$t_0 = t_2 - \left(\frac{\ell}{2} - x\right)\frac{n}{c} - \frac{d}{c} \qquad (4-7)$$

where x is the distance (along the length of the counter) from the center of the counter that the particle hits, c is the speed of light, t_2 is the time obtained from the other end of the counter and d is the distance traveled by the particle in its

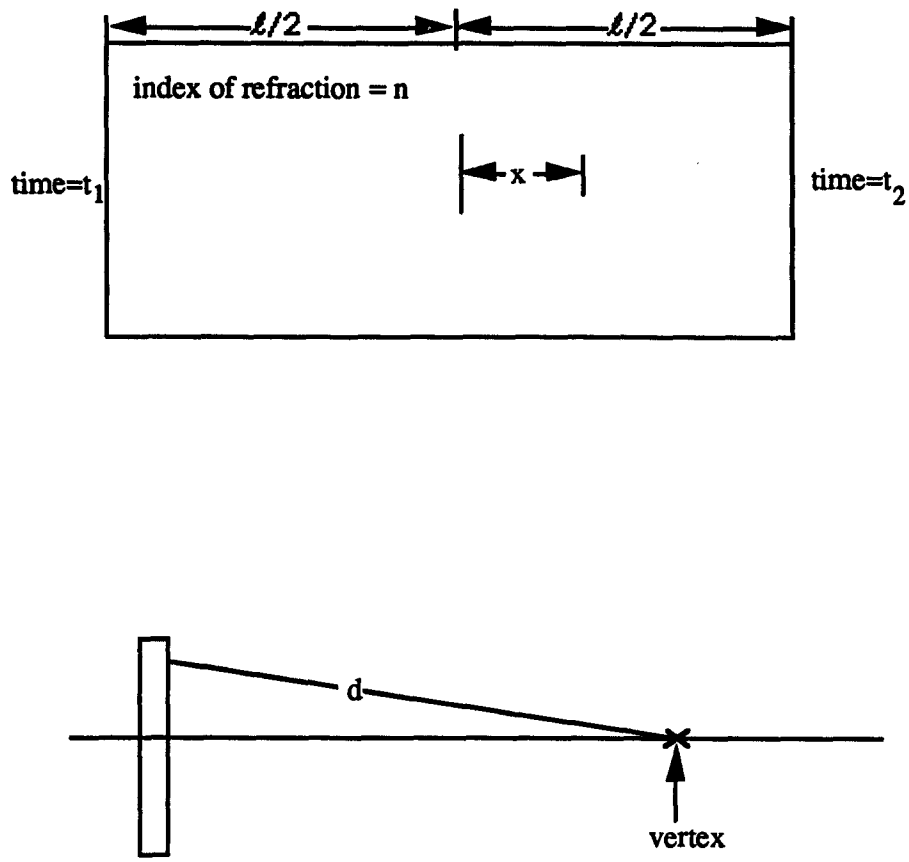

Figure 4-10. A trigger hodoscope counter of length ℓ and an index of refraction n, which is hit by a particle which has traveled a distance, d, from the vertex. The particle hits a distance, x, from the center of the counter giving a time, t_1, at one end of the counter and t_2 at the other end.

flight (the z intercept of the track to be identified, with the beamline is used as the starting point to obtain this distance). Since multiple hits in a single counter cause poor time resolution, the counter used in each array was subjected to a minimum ionizing cut. This required only one minimum ionizing particle in each counter used to find the vertex and the interaction time. Taking the counter with the earliest hit in each array of the trigger hodoscope gives four values of t_0 (two counters with two ends each). These are averaged to get a better value for t_0.

The interaction time is then used to calculate the time of flight of the particle. First, using the track reconstructed in the spectrometer arm, the TOF1 counter which is most likely to have been hit by the particle is found. Since the TOF1 counters are horizontal, this involves finding the y position of the track at the x location of TOF1 and checking the z position of the track at TOF1 to be sure the particle would have hit a counter. Figure (4-11) shows the difference between the z-coordinate of the track at TOF1 (z_{trk}) and the corresponding hit in the TOF1 counter.

The time obtained from one end of a counter is (see figure 4-12)

$$T_1 = \left(\frac{L}{2} + x'\right)\frac{n_1}{c} + \frac{D}{v} + t_0 \qquad (4-8)$$

again, for the other end

$$T_2 = \left(\frac{L}{2} - x'\right)\frac{n_1}{c} + \frac{D}{v} + t_0 \qquad (4-9)$$

for a counter of length L and an index of refraction n_1 which is hit a distance x' from its center by a particle which traveled a distance D at a velocity v after an

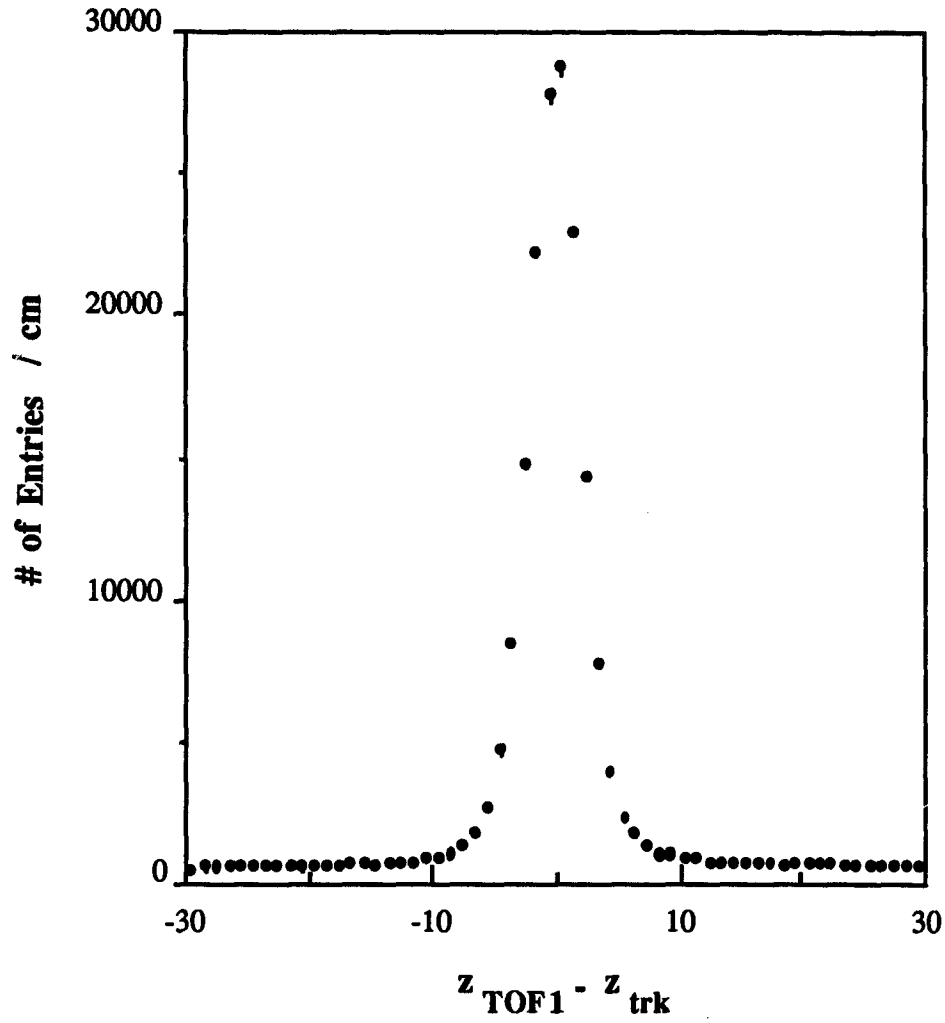

Figure 4-11. Plot of the difference in the z direction between the track position at TOF1 (z_{trk}) and the hit in the corresponding TOF1 counter (z_{TOF1}).

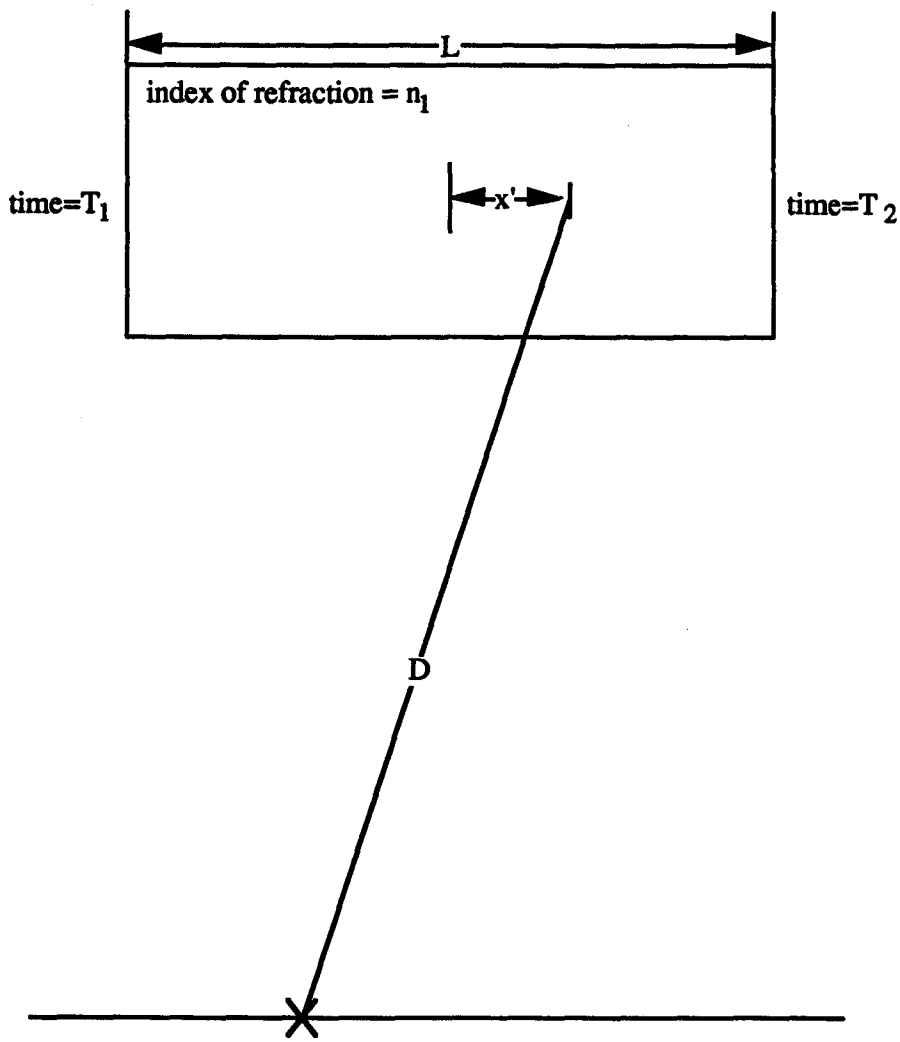

Figure 4-12. A TOF1 counter of length L and an index of refraction n_1, which is hit by a particle which has traveled a distance, D, from the vertex. The particle hits a distance, x', from the center of the counter giving a time, T_1, at one end of the counter and T_2 at the other end.

event which occurred at a time t_0. So, adding the two equations, the time of flight of the particle, D/v, is given by;

$$T_{off} = \frac{D}{v} = \frac{(T_1 + T_2)}{2} - \frac{Ln_1}{2c} - t_0 \qquad (4-10)$$

and from this, the velocity of the particle is;

$$v = \frac{D}{T_{off}} \qquad (4-11)$$

From this we can find a value for the mass of the track using;

$$m = \frac{p}{\gamma\beta} = p\frac{\left(\sqrt{1-\frac{v^2}{c^2}}\right)c}{v} \qquad (4-12)$$

In figure (4-13) and figure (4-14) the mass of particles from this method is plotted for two different momentum ranges.

This mass was then used to identify protons and antiprotons. If the calculated mass of the particle was greater than 0.65 GeV/c^2 and less than 1.5 GeV/c^2 then the particle was call a proton (or antiproton for negative particles). These limits were determined by a Monte Carlo which will be discussed in the next chapter. With these limits, more than 95% of all protons with momentum less than 2.5 GeV/c are selected. Any particle with a mass below the lower mass cut was called a π. This particle identification reduced the data sample under consideration by about a factor of ten. Figure (4-15) shows the invariant mass plots for all $p\,\pi^-$ and, separately, all $\bar{p}\,\pi^+$ pairs.

In order to enhance the ratio of the Λ ($\bar{\Lambda}$) signal to the background, the $p\pi^-$

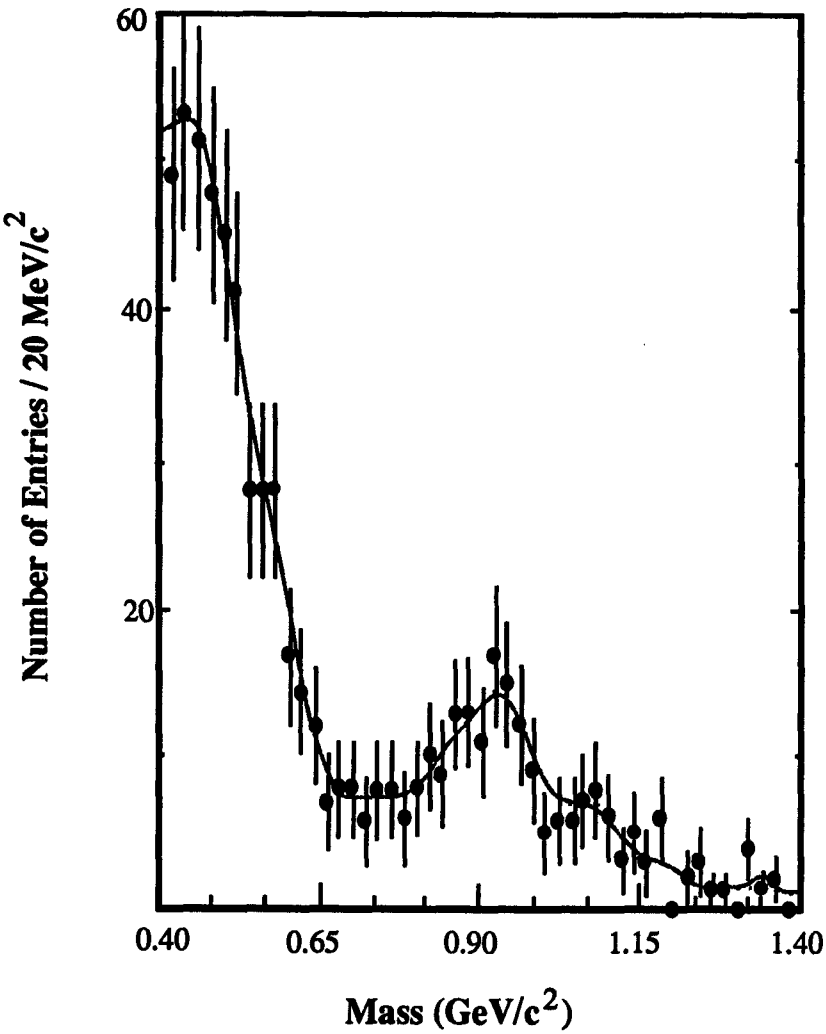

Figure 4-13. Mass plot from time of flight for charged particles with a momentum, 0.5≤ GeV/c ≤ p ≤ 0.6 GeV/c. Evident in the plot is part of the kaon peak and all of the proton peak.

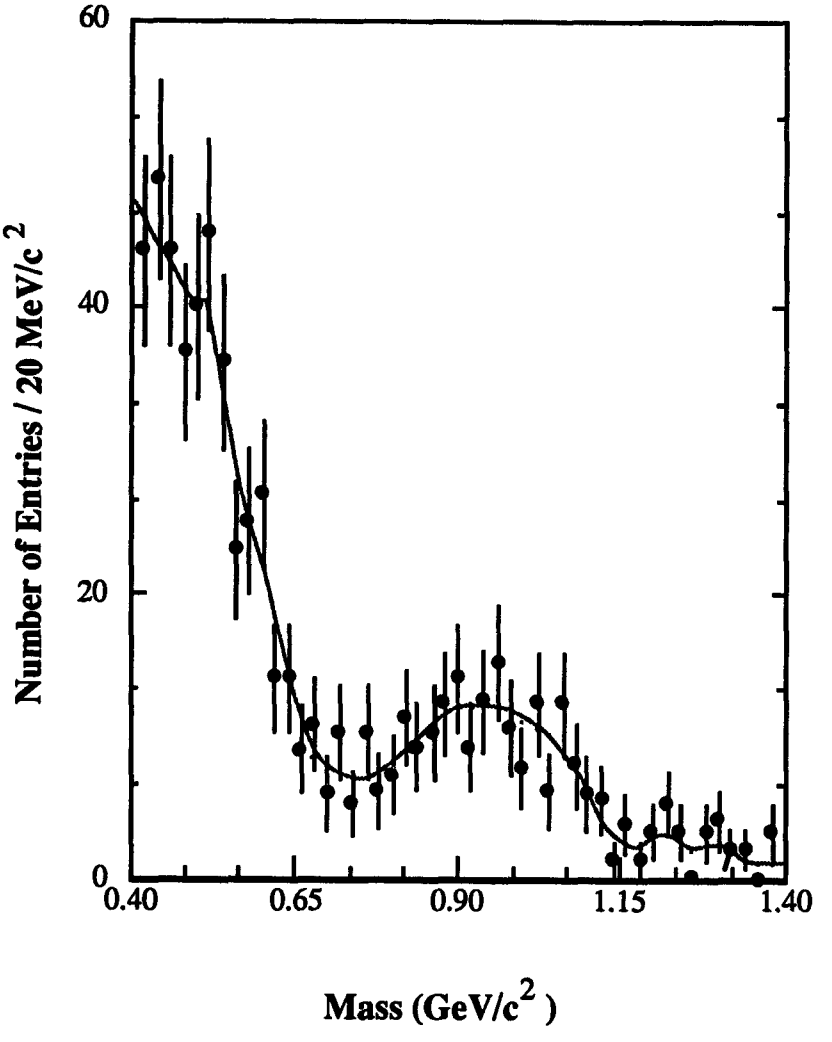

Figure 4-14. Mass plot from time of flight for charged particles with a momentum, 0.6≤ GeV/c ≤ p ≤0 .7 GeV/c. Evident in the plot is part of the kaon peak and all of the proton peak.

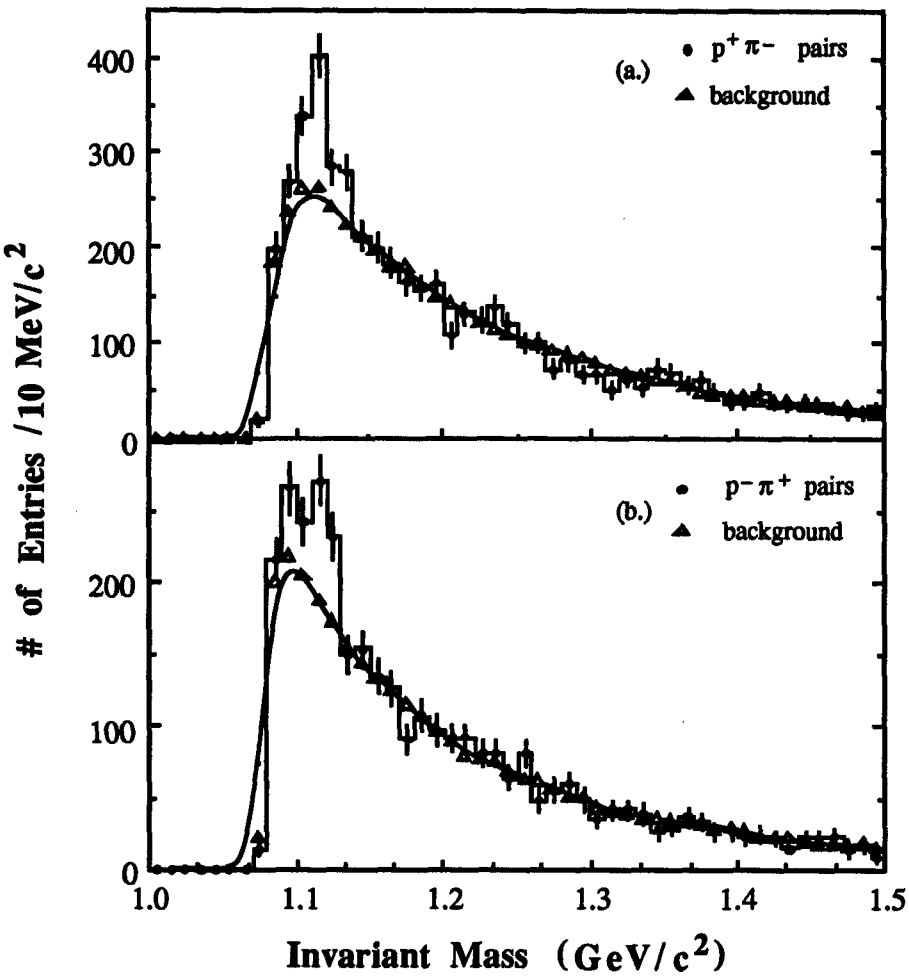

Figure 4-15. Invariant Mass plots for all (a) $p^+\pi^-$ and all (b) $p^-\pi^+$ pairs with background before cuts. Protons mass identified by time of flight measurement.

($\bar{p}\pi^+$) pairs were subjected to cuts. In this and the following two sections, these cuts will be discussed. We will look at the reasons for the cuts and their effects. The first of these cuts to be discussed is concerned with the x projection of the decay position of the Λ.

In order for both the π and the proton ($\bar{p}$) to get into the limited aperture of the spectrometer arm, the parent Λ ($\bar{\Lambda}$) had to be traveling toward the spectrometer. The most obvious manifestation of this fact is that the x position of the Λ when it decayed must have been positive. Logically, this would lead to the requirement that the x intercept of the π and proton tracks be greater than 0. In order to take into account the error in the reconstructed slopes and intercepts of the two tracks, this cut was varied. It was found that the signal to noise ratio was optimized for a cut requiring that the tracks intercept at a point $x > -10.0$ cm.

In the first section of this chapter, the difference in the quality of tracks was discussed. The lowest quality tracks included those with no hits in the pre-magnet chamber. Without hits in the pre-magnet chamber, there is no tracking before the magnet and it is difficult to calculate the momentum of the track. These tracks are not used in this analysis and this provides another limit on the x position of the Λ decay.

As stated in the previous chapter, the pre-magnet chamber is located at approximately $x = +55$ cm. In order for the tracks to have hits in this chamber, the Λ must decay before it reaches the pre-magnet chamber. Therefore, the upper limit on the intercept of the proton and π tracks is $x=50$ cm. For a decay length of at

least 50 cm, over 99% of all Λ's created with a momentum of 0.5 GeV/c have decayed and over 90% of all Λ's created with a momentum of 3.0 GeV/c. So very few Λ's are lost by this cut.

Figure (4-16) shows the invariant mass plot of all $p^+\pi^-$ pairs and $p^-\pi^+$ pairs which pass the decay vertex cuts. Of all the $p\,\pi^-$ pairs identified, 61% passed these two cuts. Of all the $\bar{p}\,\pi^+$ pairs identified, 74% passed these two cuts. Combining both $p\,\pi^-$ and $\bar{p}\,\pi^+$, 66% passed these two cuts.

The kinematics of a two body decay, such as $\Lambda \rightarrow p^+\,\pi^-$, are well determined. For a decaying particle of a given mass and momentum, measuring the angles (in the laboratory frame) between the direction of the parent and the directions of the products completely determines the momenta of the products. This knowledge of the allowable kinematics of the decay ($\Lambda \rightarrow p^+\,\pi^-$) can be used to make cuts on the Λ sample.

The first kinematic cut makes use of the small amount of energy available to the decay products as momentum in the center of mass frame of the decay. Since most of the energy of the decay goes into creating the π and the proton, the momentum of the products is only about 100 MeV in the rest frame of the decay. If we define the x direction as being the direction of travel of the Λ in the laboratory frame, then the Lorentz transformation of the momentum of the proton and the π to the laboratory frame is given by the equations

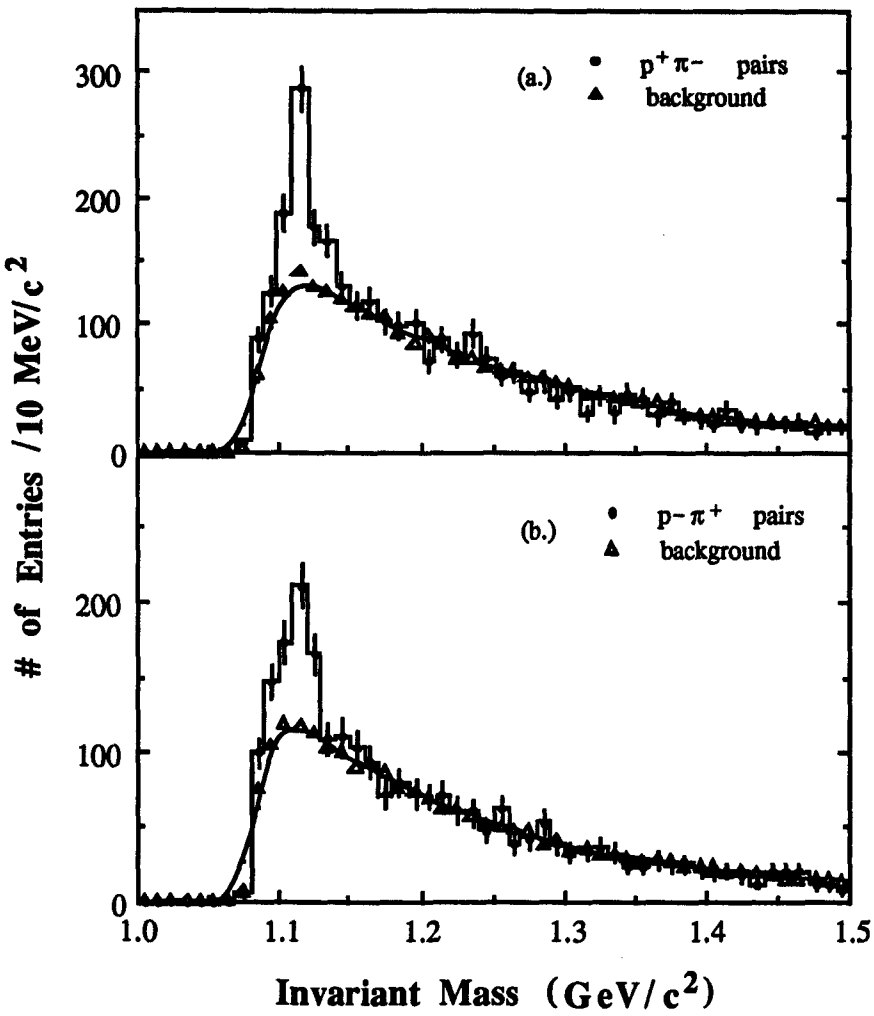

Figure 4-16. Invariant Mass plots for all (a) $p^+\pi^-$ and all (b) $p^-\pi^+$ pairs with background after cuts on x-position of the Λ decay vertex ($-10.0<x_{decay}<.\ 50.0$ cm).

$$p_{x_p} = p_x * \frac{E_\Lambda}{m_\Lambda} + E_p * \frac{p_\Lambda}{m_\Lambda} \qquad (4-13)$$
$$p_{y_p} = p_y$$
$$p_{z_p} = p_z$$

$$p_{x_\pi} = -p_x * \frac{E_\Lambda}{m_\Lambda} + E_\pi * \frac{p_\Lambda}{m_\Lambda} \qquad (4-14)$$
$$p_{y_\pi} = -p_y$$
$$p_{z_\pi} = -p_z$$

where p_x, p_y and p_z are the components of the momentum of the proton in the Λ decay frame, and E_p (E_π) is the energy of the proton (π) in this frame. For p_Λ greater than about 300 MeV, the second term in the equations for x components of the proton and π momenta tend to dominate. Therefore since $E_p > E_\pi$, for Λ's with momentum above about 300 MeV, the momentum of the proton is always greater in the laboratory frame than the momentum of the π. This was required of all of the $p\,\pi^-$ and $\bar{p}\,\pi^+$ pairs remaining after the decay vertex cuts.

The other kinematic cuts deal with limits on the momenta of the proton and π which are being considered as Λ candidates. First, the momentum of the π must be greater than 150 MeV/c. This cut was made because of the acceptance of the spectrometer arm. The acceptance, including magnetic acceptance as a function of momentum and track reconstruction efficiency as a function of momentum, drops rapidly below p=150 MeV (Alexopolous, et al, 1988).

The π's used in the proton π pairs are also required to have a momentum less

than 900 MeV/c. This is slightly higher than the kinematic limit for π's coming from 3.0 GeV/c Λ's when the direction of the π in the decay frame is the same as the direction of the Λ in the laboratory frame. From equation (4-14)

$$p_{x_\pi} = \frac{\left(0.1\frac{GeV}{c}\right)(3.2\,GeV)}{1.115\frac{GeV}{c^2}} + \frac{(0..177\,GeV)\left(3.0\frac{GeV}{c}\right)}{1.115\frac{GeV}{c^2}} = 0.76\frac{GeV}{c}$$

$$p_{y_\pi} = 0$$

$$p_{z_\pi} = 0\,.$$

The last kinematic cuts set a lower limit on the momentum of the proton and the reconstructed Λ candidate. Since we are only studying at Λ's with a transverse momentum greater than 0.5 GeV/c, we can set a lower limit on the Λ momentum. Therefore, Λ candidates with momentum less than 0.5 GeV/c are cut from the sample. Also, for 0.5 GeV/c Λ's, the proton from the decay must be above a minimum momentum. This minimum occurs when the proton direction in the decay frame is opposite to the Λ direction in the laboratory frame. From equation (4-13),

$$p_{x_p} = \frac{\left(0.1\frac{GeV}{c}\right)(1.222\,GeV)}{1.115\frac{GeV}{c^2}} + \frac{(0.944\,GeV)\left(0.5\frac{GeV}{c}\right)}{1.115\frac{GeV}{c^2}} = 0.314\frac{GeV}{c}$$

$$p_{y_p} = 0$$

$$p_{z_p} = 0\,.$$

So the proton must have a momentum greater than 0.314 GeV/c. For this analysis, any proton with a momentum less than 0.3 GeV/c was cut from the

sample.

After all of these kinematic cuts, 71% of the p π^- pairs which survived the decay vertex cuts still remained. Of the $\bar{p}\ \pi^+$ pairs which survived through the decay vertex cuts, 75% survived the kinematic cuts. Of all pairs remaining after the decay vertex cuts, 73% survived the kinematic cuts. Figure (4-17) shows the invariant mass plots for (a.) p π^- pairs and (b.) $\bar{p}\ \pi^+$ pairs which survived these kinematic cuts.

The final type of cut is equivalent to one of the cuts for background tracks discussed in the last chapter. When looking at individual charged tracks, a cut is made on the difference between the track vertex and the vertex determined by the trigger hodoscope counters. However, when looking at charged tracks which may have come from the decay of another particle, this cut is not useful, since there is no reason to believe that these tracks should point back to the event vertex.

A more reasonable cut is to require that the Λ track should point back to the event vertex. Therefore, the Λ ($\bar{\Lambda}$) which is reconstructed from the p π^- ($\bar{p}\ \pi^+$) pair is required to come within $z = \pm$ 12cm of the event vertex as determined by the trigger hodoscope counters. The RMS error for the event vertex as determined by the trigger hodoscopes is 5 cm.

Approximately 81% of the p π^- pairs which remained before this cut, still survived after this cut was applied. Of the $\bar{p}\ \pi^+$ pairs which had survived all the other cuts, 85% remained after the event vertex cut. Combined, 83% of all the Λ candidate pairs survived the event vertex cut. Of all the candidate pairs which had an identified proton, but had not been subjected to any of the above cuts, 40% were

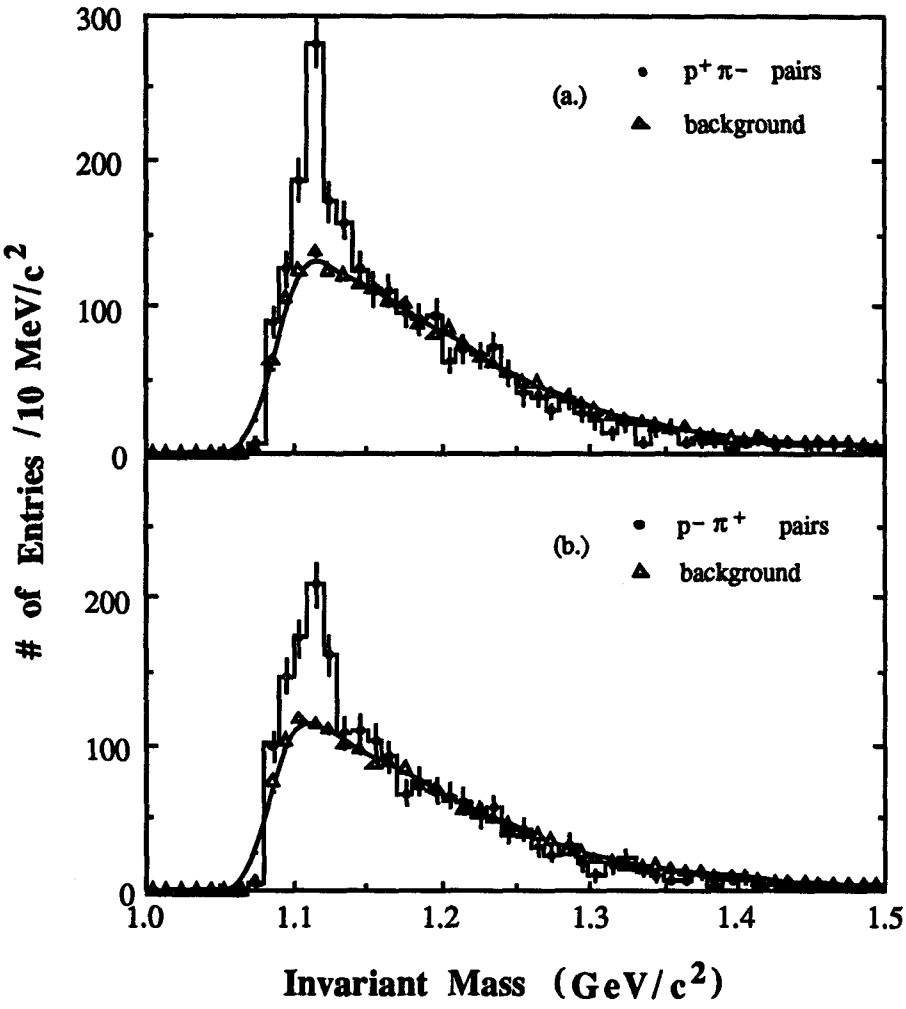

Figure 4-17. Invariant Mass plots for all (a) $p^+\pi^-$ and all (b) $p^-\pi^+$ pairs after momentum cuts have been applied (0.3 GeV/c $\leq p_p$, $p_\pi < p_p$, 0.15 $\leq p_\pi <$ 0.9 GeV/c and 0.5 GeV/c $\leq p_\Lambda$).

Table 4-1
Cuts imposed and the effects of each cut.

Condition Imposed	Number of $p^+\pi^-$ pairs surviving this cut	%	Number of $p^-\pi^+$ pairs surviving this cut	%	Total # of pairs surviving this cut	%
mass identified proton ($\bar{p}$)	5400	100	3620	100	9020	100
$-10.0 \leq x_{decay} \leq 50.0$ cm	3316	61.4	2665	73.6	5981	66.3
momentum cuts	2352	70.9	1991	74.7	4343	72.6
$\lvert z_{\Lambda\ intercept} \rvert \leq 12.0$ cm	1928	82.0	1694	85.1	3622	83.4

left after all the cuts were applied. Table 4-1 gives a summary of the cuts used and the effects each cut had on the data. Figure (4-18) shows the invariant mass plot for all $p\ \pi^-$ pairs and all $\bar{p}\ \pi^+$ pairs after all of the above cuts were applied. The method through which the background shown in the figures was found will be discussed next.

Since the ratio of noise to signal in the data sample for Λ's is about one to one

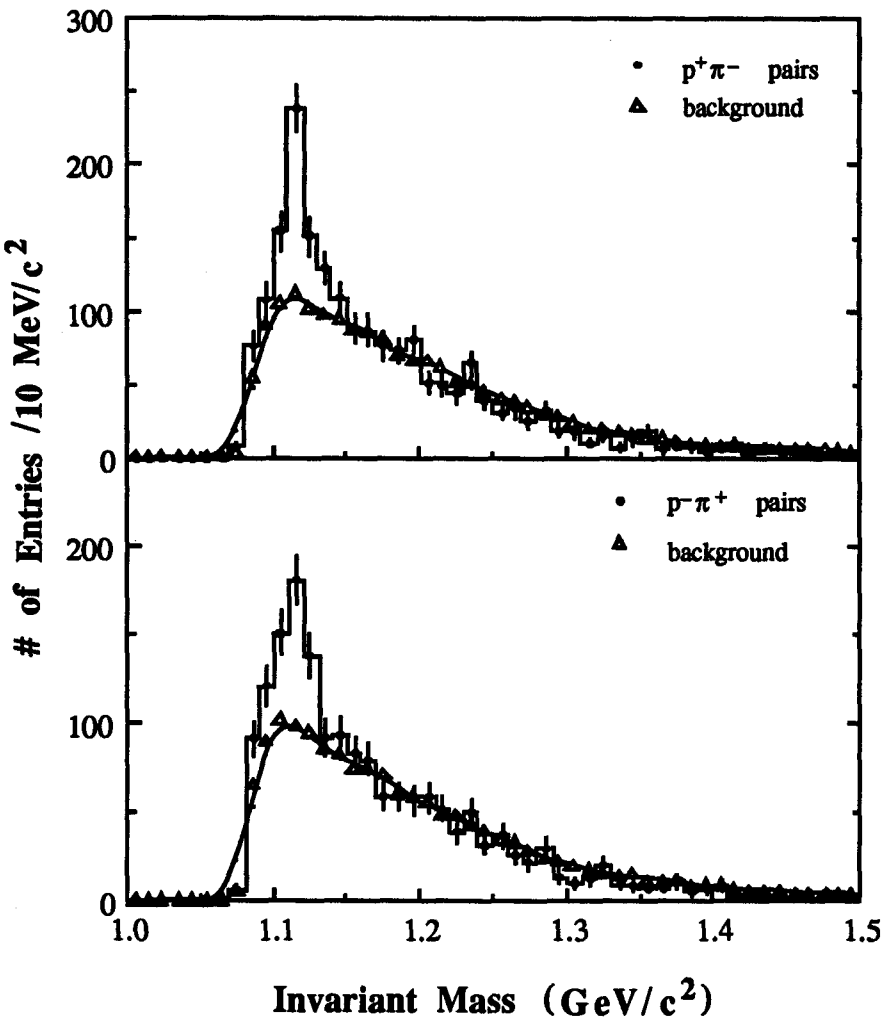

Figure 4-18. Invariant Mass plots for all (a) $p^+\pi^-$ and all (b) $p^-\pi^+$ pairs after all cuts have been applied (including vertex cuts; $|z_\Lambda - z_{ev}|<12.0$cm).

after every cut discussed above is applied, generating a reasonable background is very important. The first method tried was to use same sign $p\pi$ pairs taken from the same event. This is the most obvious way to ensure there are no Λ's in the generated background.

Problems with this approach were encountered however. The major problem which effects the shape of the background is the difference in the effective aperture for same sign pairs as opposed to opposite sign pairs. This difference in effective aperture, which is especially significant for low momentum pairs, causes an over-abundance of pairs with low invariant mass for the same sign sample. Therefore, a different method was sought to generate a background.

The method which was used to generate a background for the Λ analysis involved opposite sign pairs from different events. For each event, an extra proton from another event was added to the array of tracks already present in the event. The intercept of the proton which was added to the event was adjusted such that the simulated origin of the proton was in the same position relative to the event vertex in this new event as the actual origin was to the event vertex in the event from which the proton came. This was done to simulate the actual background distribution for the $p\,\pi$ intercept.

Using the proton which had been introduced into the event and all π's with opposite sign, an invariant mass was calculated for each pair. These pairs were then subjected to the same cuts, discussed previously, as the data sample. The resulting distribution was then used as the background which, when normalized, was subtracted to find the number of Λ's ($\bar{\Lambda}$'s) in the data. Figure (4-19) shows the

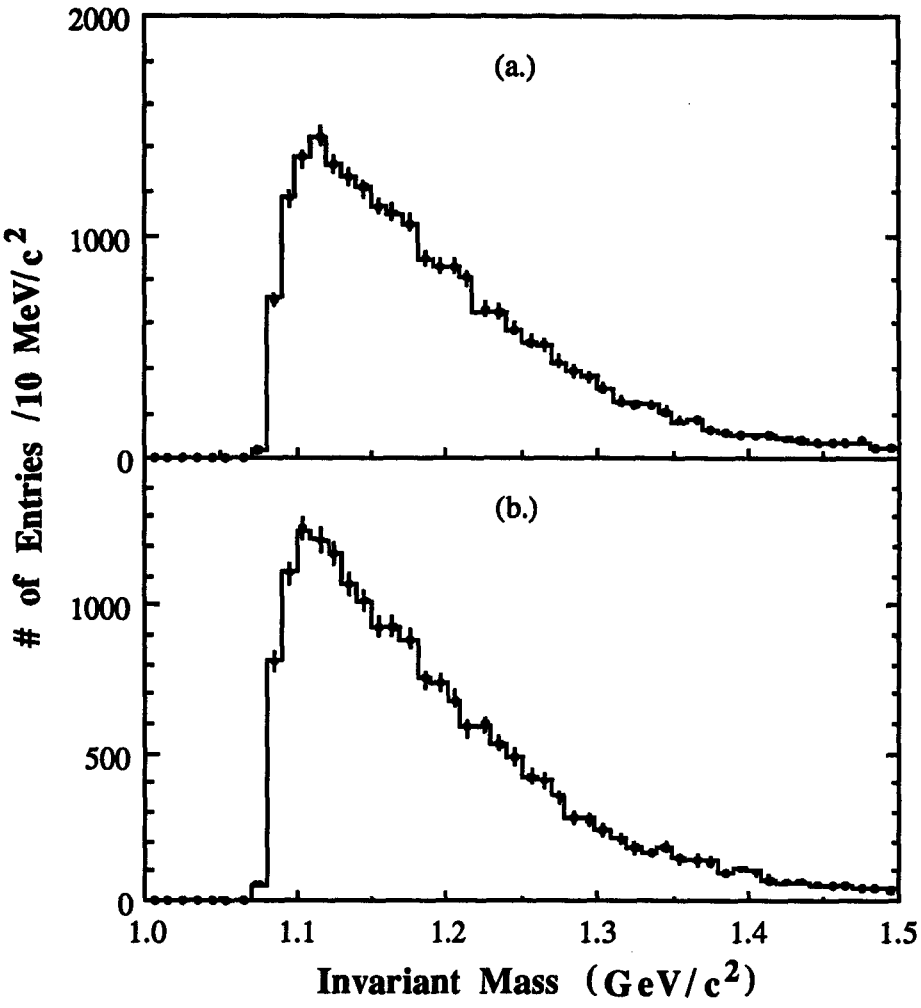

Figure 4-19. Background for (a) Λ's and (b) $\overline{\Lambda}$'s generated from $p^+\pi^-$ ($p^-\pi^+$) pairs from different events. Both plots were made after all cuts had been imposed.

background generated in this manner for (a) p π^- pairs and (b) $\bar{p}\,\pi^+$ pairs.

As a check on the quality of the Λ sample, the proper decay length ($L_0=L/\gamma\beta$) was plotted after background subtraction. Figure (4-20) shows the proper decay length distribution for the Λ's and $\bar{\Lambda}$'s in the data. Using the invariant mass cuts discussed in the next section ($1.10 \leq M \leq 1.13$ GeV/c^2), the data was divided into two groups, pairs which fell inside the limits (Λ's plus background) and those which fell outside (background). Since Λ's could not be identified on an event by event basis, the distribution is plotted for both groups. The distribution for those outside the invariant mass cuts is then normalized to the number of background events within the cuts and subtracted from the distribution for Λ's plus background. The curve is from an exponential using the known decay length for Λ's and is provided for comparison. Figure (4-21) shows a plot of the expected decay length distribution for Λ's and $\bar{\Lambda}$'s generated by the Monte Carlo discussed in the next section. Once again, the curve is an exponential using the known decay length for Λ's. The flattening of the tail of the distribution from the data is also seen in the Monte Carlo generated distribution.

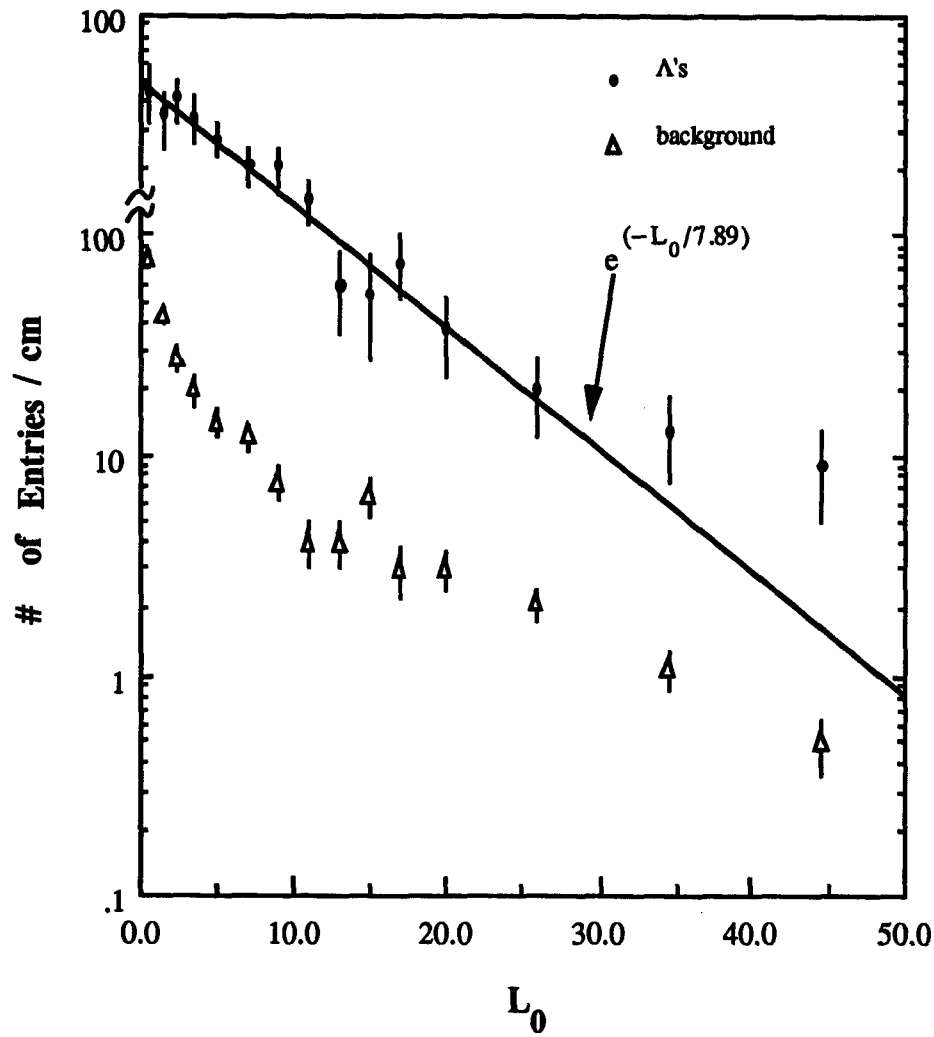

Figure 4-20. Proper decay length (L_0=L/$\gamma\beta$) distribution for Λ's and $\overline{\Lambda}$'s from our data. Also shown is the background distribution determined as discussed in the text. The solid line is the decay distribution using the known decay length for Λ's and $\overline{\Lambda}$'s .

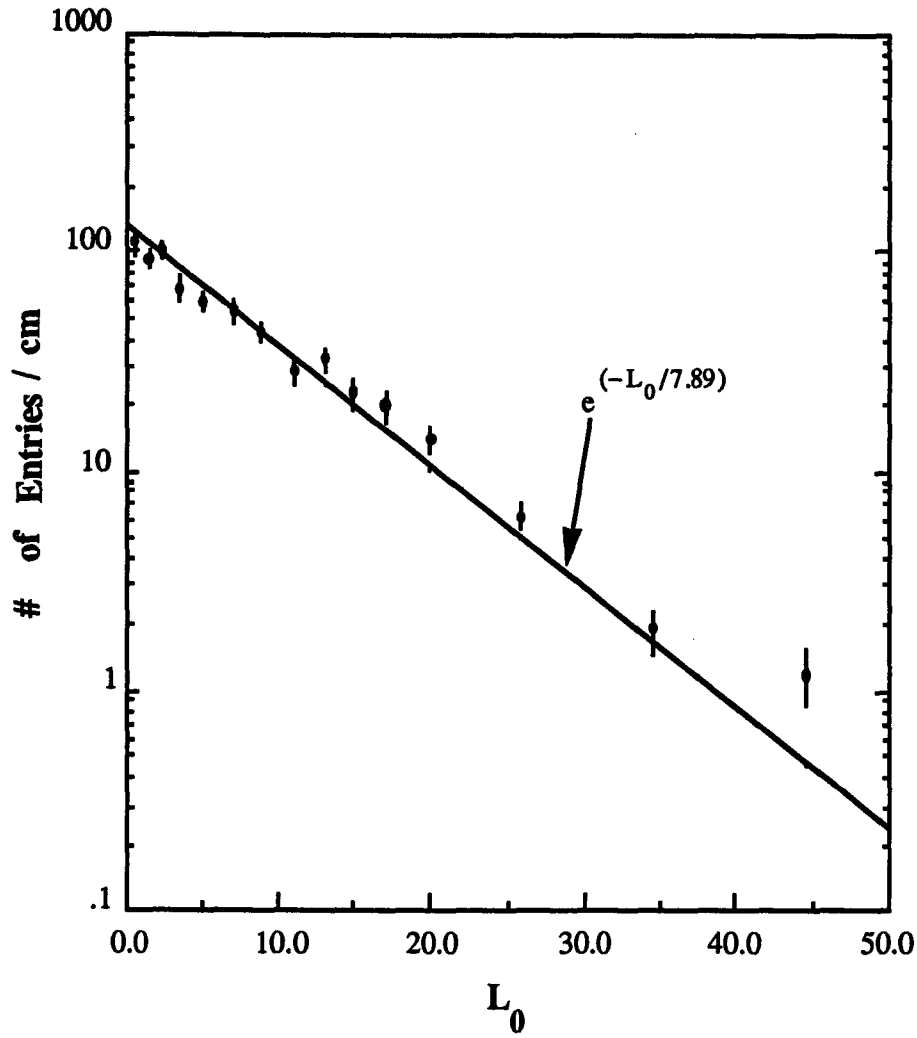

Figure 4-21. Proper decay length (L_0=L/$\gamma\beta$) distribution for Λ's and $\overline{\Lambda}$'s generated uniformly in rapidity in a detailed Monte Carlo.

III. Acceptance Corrections

Acceptance corrections to the observed number of Λ's were generated through a Monte Carlo simulation. In this Monte Carlo, Λ's ($\bar{\Lambda}$'s) with a given transverse momentum are generated uniformly in azimuth and uniformly in the rapidity interval, $-1.2 < y < 1.2$. The event vertex distribution and therefore the distribution of the Λ vertices, was generated from a Gaussian which was centered at z=+10 cm and had a σ_z= 30.0 cm to match the vertex distribution obtained from the data.

Lambdas which are headed toward the spectrometer aperture undergo a simulated decay into a proton and a π. If this decay occurs inside the beam pipe, the proton and the π are subjected to energy loss in the beam pipe. Next, the paths of the decay products are projected into the chambers of the spectrometer arm. For each chamber plane, simulated hits are generated (which include the

effects of multiple scattering, the measured detector position resolution and decays).

Using these simulated hits, tracks are reconstructed in the same manner as for the data. At this point, the effects of the particle identification efficiency of the time of flight counters are included. The particle identification efficiency of these counters is obtained from the data by calculating the fraction of reconstructed tracks which pass the cuts for good particle identification. With the cuts used in this analysis, approximately 65% of the tracks have good particle identification. Therefore, to simulate this effect, 35% of the protons in the Monte Carlo are randomly assigned the π mass.

The resolution of the time of flight counters is taken into consideration next. To simulate the mass distribution from the data, the actual time of flight from the vertex to TOF1 of the particle is calculated and an error determined from a Gaussian distribution, with a resolution of 250 ps (FWHM). From this time the mass is calculated and the proton mass cuts, discussed previously, are applied. As with the data, those passing the cuts are called protons, those below the cuts are called π's and those above the cuts are not used. In simulated events where an identified proton and a π pass the above conditions, an invariant mass is calculated for the pair. Each Monte Carlo p π pair is then subjected to the same cuts as those in the data. The x projection of the Λ decay point, the kinematic cuts and the Λ vertex cut discussed in detail earlier in this chapter, are used in this Monte Carlo.

From this Monte Carlo routine, the expected width of the invariant mass peak

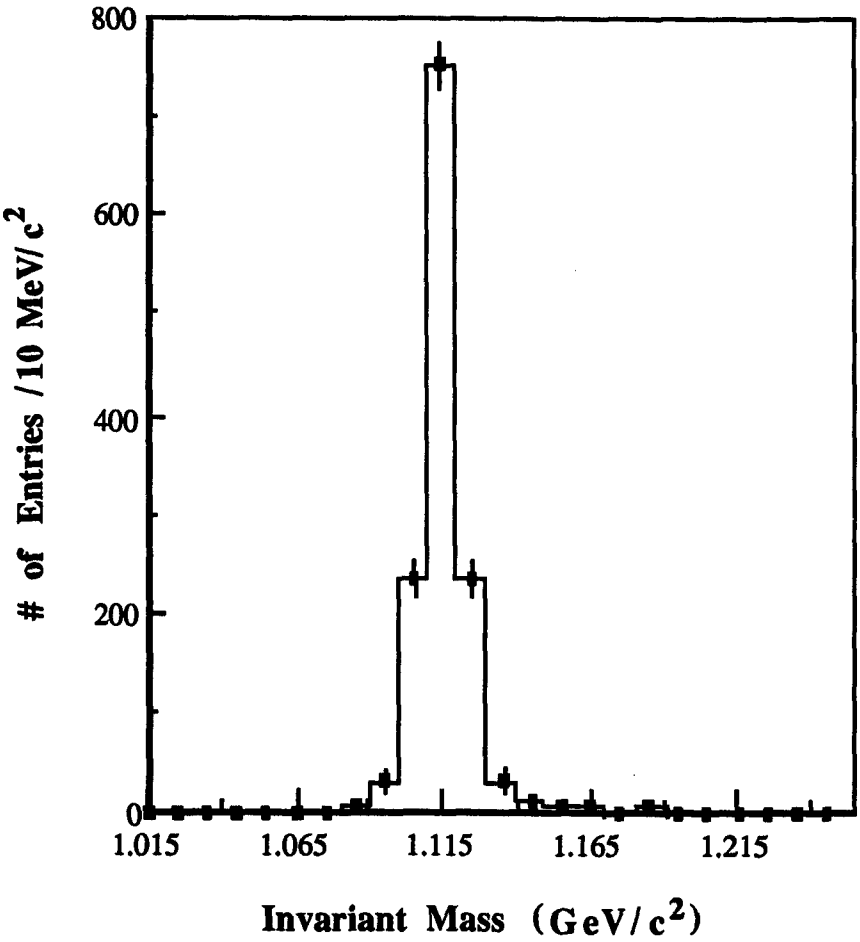

Figure 4-22. Invariant mass plot for Λ's and $\overline{\Lambda}$'s generated by Monte Carlo with a transverse momentum (p_t) of 1.0 GeV/c. The mass is from the analysis program after a detailed Monte Carlo of the detector has been used.

for Λ's and $\bar{\Lambda}$'s was obtained. In figure (4-22), the invariant mass distribution for Λ's which were generated with p_t=1.0 GeV/c by the Monte Carlo is plotted after all cuts. As can be seen in the figure, more than 90% of all reconstructed Λ's have an invariant mass 1.10 <M< 1.13 GeV/c^2. This statistic is fairly constant for the transverse momentum range, $0.5 \leq p_t \leq 3.0$ GeV/c. This is true for $\bar{\Lambda}$'s as well as Λ's. Figure (4-23) shows the background subtracted invariant mass plot for Λ's and $\bar{\Lambda}$'s together. In this figure, the data are plotted for the full p_t range. Reasonable agreement can be seen between the width of the peak for the data and the width of the peak for the limited p_t range Monte Carlo peak.

The acceptance correction to the number of observed Λ's was calculated relative to the acceptance for charged π's. The number of accepted π's was obtained from a Monte Carlo procedure similar to the one used for Λ's. At each p_t, the same number of π's were generated as Λ's. The relative acceptance, shown in figure (4-24), is for Λ's + $\bar{\Lambda}$'s accepted divided by $\pi^+ + \pi^-$ accepted $((\Lambda+\bar{\Lambda})/(\pi^+ + \pi^-))$ as a function of p_t. As can be seen in the figure, the relative acceptance drops rapidly with decreasing transverse momentum and is very low below p_t=0.5 GeV/c. For this reason, only the region above 0.5 GeV/c was considered for this analysis.

Other acceptance corrections, discussed below, were studied using the Geant Monte Carlo program (CERN, 1985). The Geant Monte Carlo program is a detector simulation which allows the detector composition, response and geometry to be included. The effects of inert (non-detector) materials can also be included in the Geant simulation. In this simulation, particles are tracked through the detector and

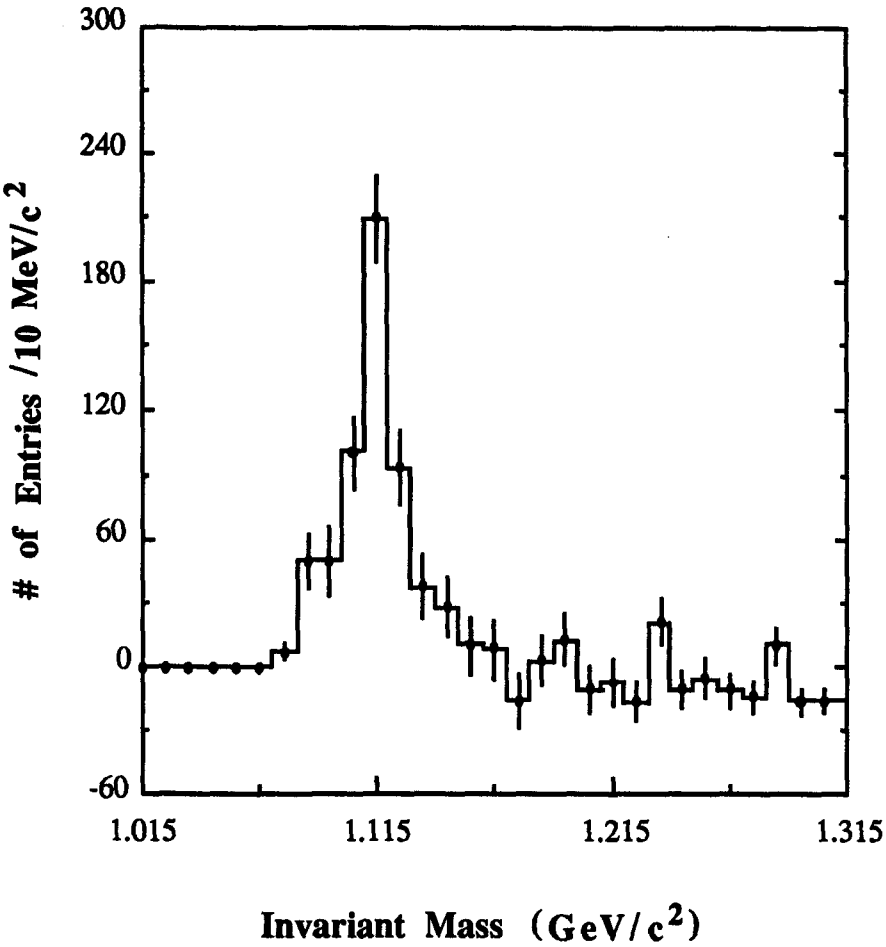

Figure 4-23. Invariant mass plot for Λ^0's and $\overline{\Lambda}^0$'s with background subtracted from the sample. The width of the peak is in good agreement with Monte Carlo predictions.

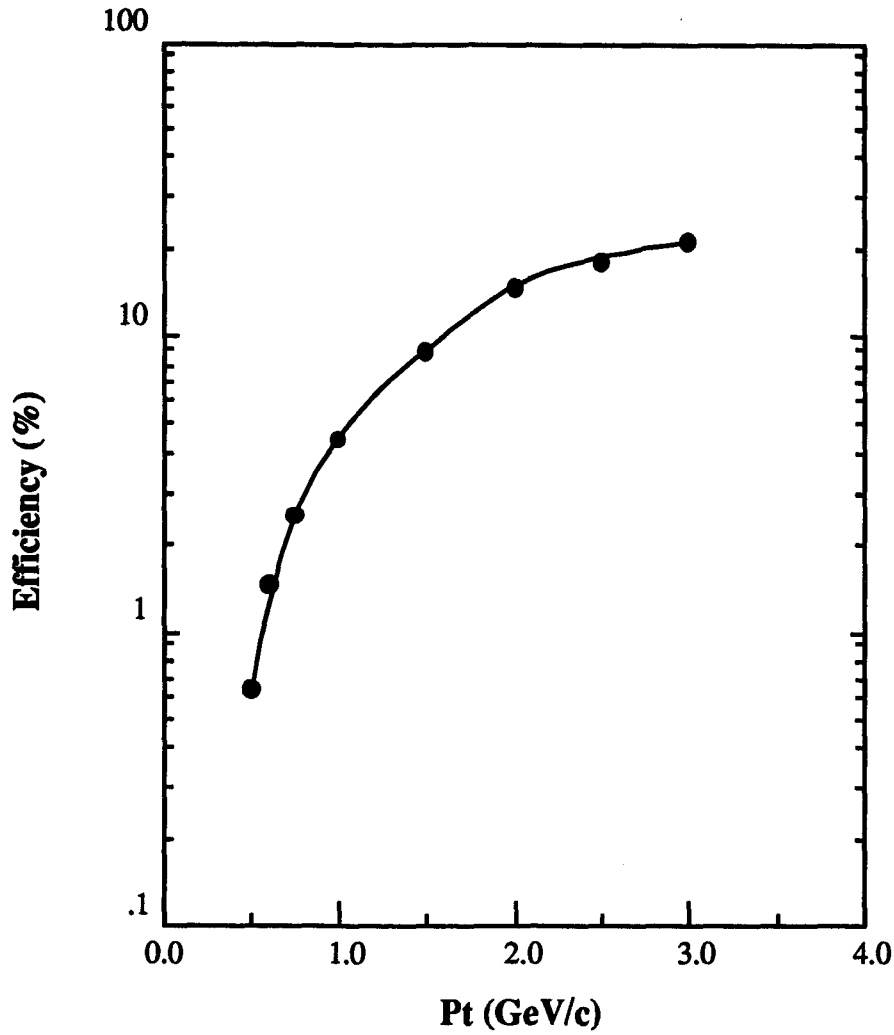

Figure 4-24. The relative acceptance, $(\Lambda+\bar{\Lambda})/(\pi^{+}+\pi^{-})$, where the quantity inside each parentheses is the number of particles of that type which were accepted (according to the Monte Carlo) out of 500,000 of each type generated.

hits are recorded. The Geant simulation includes the effects of multiple scattering, nuclear interactions, energy loss in matter and decays of particles in flight.

This simulation was used to convert the multiplicity from the hodoscope (N_h) to the true charged multiplicity (N_c). At low multiplicity, this conversion was needed because the multiplicity hodoscope recorded secondary particles from interactions of primaries in the aluminum beam-pipe as well as true primaries. Therefore, the hodoscope multiplicity was likely to be too high at low N_c. The difference for high N_c was caused by not only the secondary tracks but also the finite size of the hodoscope counters and the fact that each counter could record only one hit per event. The 240 element hodoscope could measure multiplicities up to $N_h \approx 150$ before double hits in a counter became a serious problem. For $N_c \approx 100$ the two effects described above roughly canceled and $N_h \approx N_c$. Figure (4-25) shows N_c plotted versus N_h using the Geant Monte Carlo program to study the relationship. The spectrometer arm was used as a check since multiple tracks could be more easily resolved here. Also in the spectrometer arm the vertex of the track could be used to separate primaries from secondaries. Figure (4-26) shows the number of accepted tracks in the spectrometer arm plotted versus N_h for the data and the Geant Monte Carlo program.

Another effect studied using the Geant simulation was the trigger efficiency. This effect was studied by generating events with various multiplicities and imposing the same requirements as the minimum bias trigger (PT). The PT trigger, which is based on the trigger hodoscopes, favors high multiplicity events. The effect of this correction is to change the triggered multiplicity distribution for minimum bias

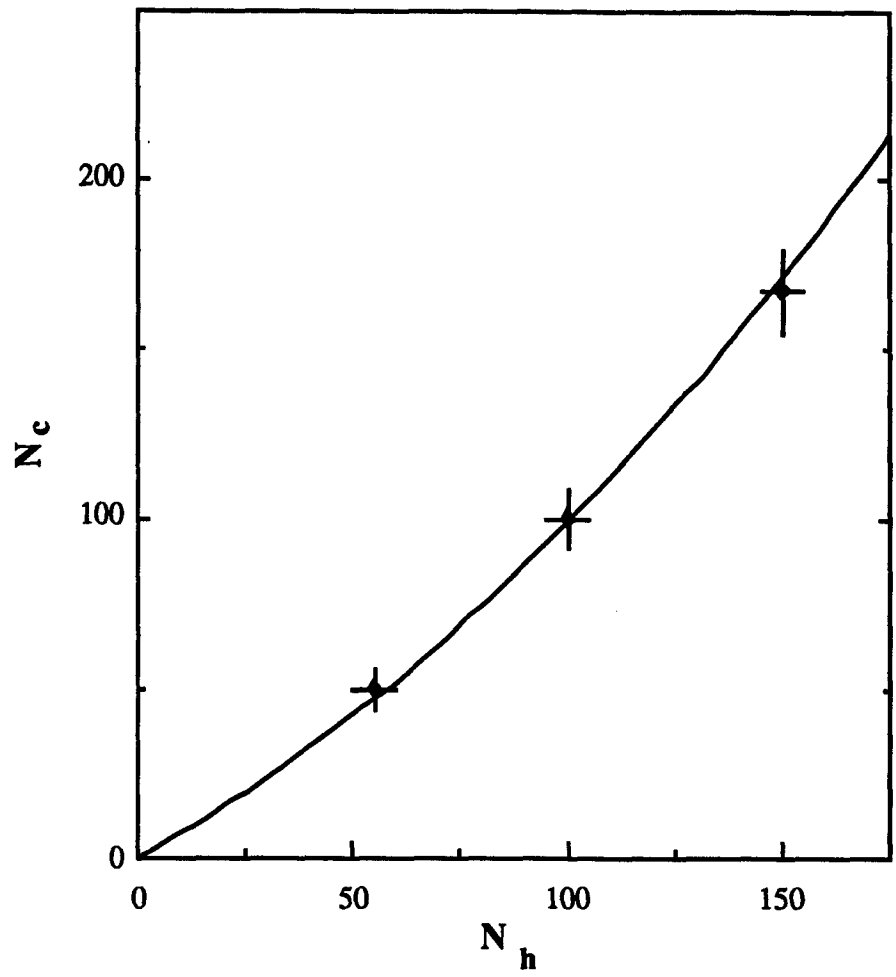

Figure 4-25. True charged multiplicity (N_c) plotted as a function of hodoscope multiplicity (N_h) from Geant Monte Carlo. Error bars show RMS spread on N_c (N_h) for a given N_h (N_c).

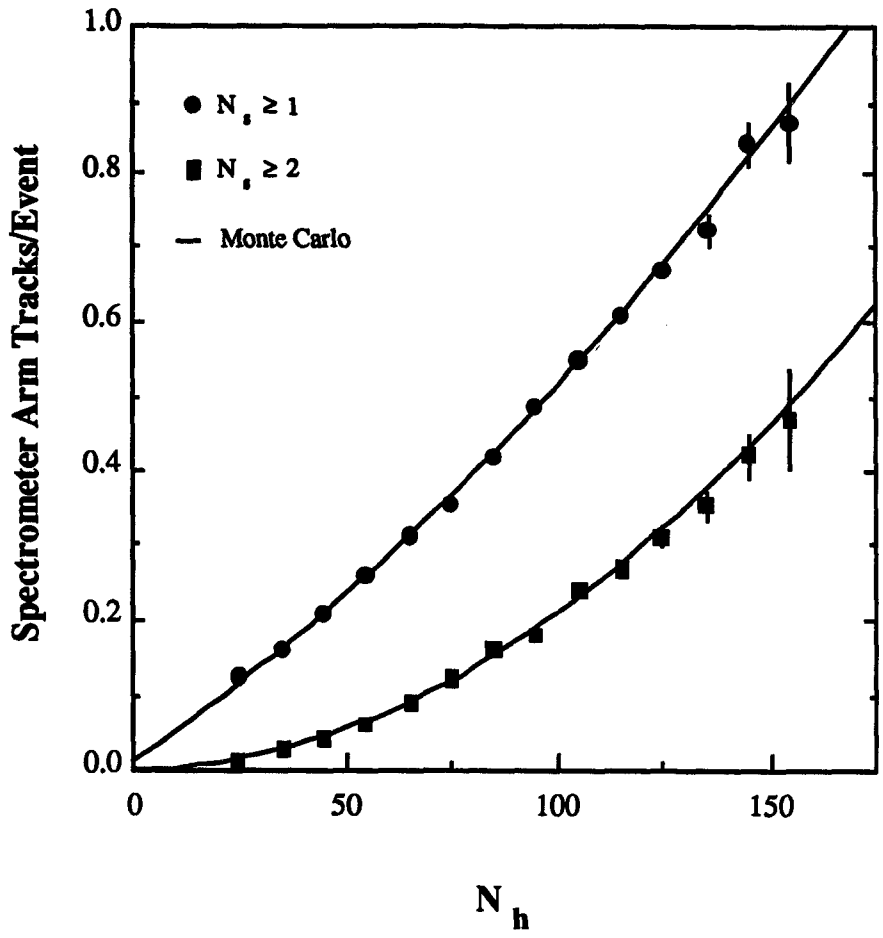

Figure 4-26. Average number of tracks in the spectrometer arm (N_s) plotted versus hodoscope multiplicity for all tracks and for $N_s \geq 2$. The curves repesent predictions of Geant Monte Carlo simulation.

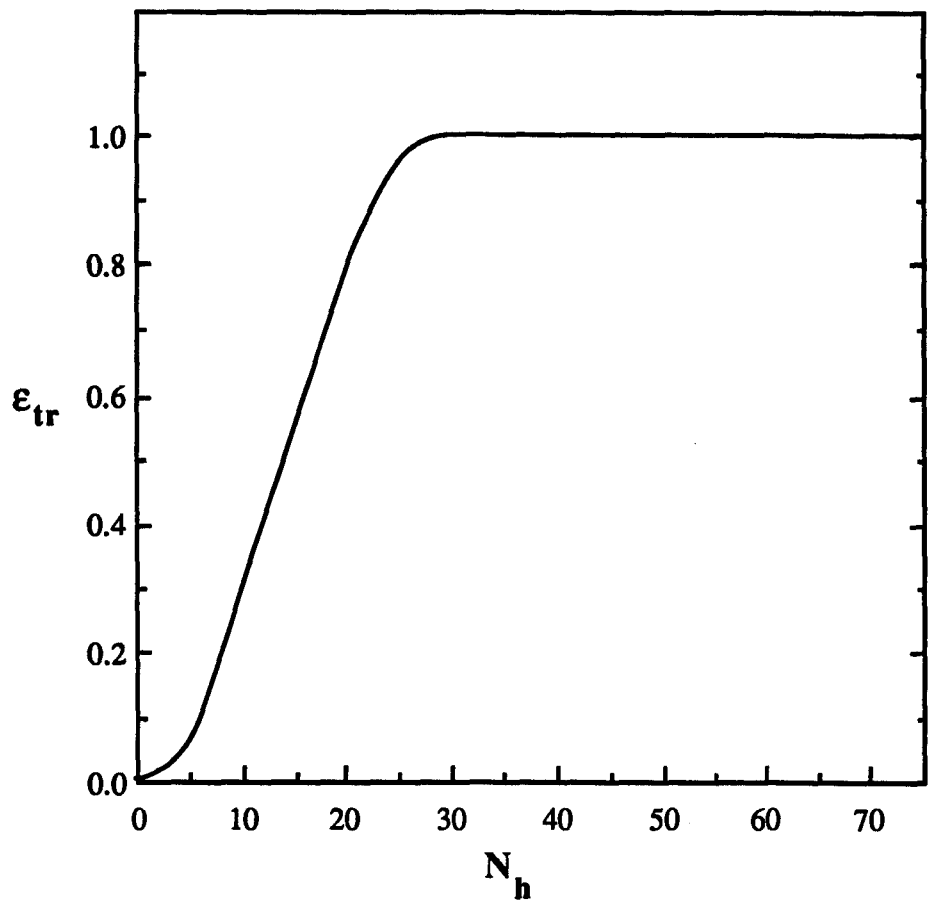

Figure 4-27. Trigger efficiency (ε_{tr}) plotted versus hodoscope multiplicity from the Geant Monte Carlo Program.

events into the real multiplicity distribution. Figure (4-27) shows the trigger efficiency ($\varepsilon_{tr}(N_h)$) plotted versus N_h. This correction is applied by weighting each track in an event of multiplicity N_h by $W_{tr}=1/(\varepsilon_{tr}(N_h))$. As shown in the figure this correction is not significant for $N_h>20$, but can be vary important for $N_h<20$.

Chapter 5

Λ^0 and $\overline{\Lambda}^0$ Production

In the previous chapter, we presented the methods used to find Λ^0's and $\overline{\Lambda}^0$'s at $\sqrt{s}$ =1.8 TeV. The first section of this chapter will deal with the results of this analysis. First, we will present the number of Λ^0's and $\overline{\Lambda}^0$'s found in the data and the ratio of Λ^0's to $\overline{\Lambda}^0$'s. Next, from the transverse momentum (p_t) spectra of Λ^0's and $\overline{\Lambda}^0$'s (both separately and together), we will obtain an average transverse

momentum for the sample. The first section ends with two ratios. The ratio of Λ^0's plus $\bar{\Lambda}^0$'s to all charged particles (N_{ac}) as a function of p_t and as a function of the charged particle multiplicity (N_c) will be presented first. Then the ratio of Λ^0's plus $\bar{\Lambda}^0$'s to protons plus $\bar{p}$'s, again as a function of p_t and as a function of N_c, will end the section.

The last sections of this chapter will deal with comparisons of these results to other data and to the results obtained using the UA5 Monte Carlo simulation. The second section will compare the results of this analysis to results at lower energies, especially CERN ISR energies ($\sqrt{s}$=53 GeV) and CERN SPS energies ($\sqrt{s}$=546 GeV). The final section will compare the results of this analysis to results obtained using the UA5 Monte Carlo event generator (G. J. Alner et al. 1987) used in conjunction with the E735 detector simulation.

I. Results at 1.8 TeV

In the last chapter, plots of the invariant mass of $p\pi^-$ and $\bar{p}\pi^+$ pairs were shown with the scaled background superimposed. The number of Λ^0's found is, by definition, the number of entries above the scaled background with an invariant mass, M_Λ, $1.10 \leq M_\Lambda < 1.13$ GeV/c^2. This was done in an iterative manner. For each iteration, the background is scaled to the number of entries in the data minus the number of Λ^0's found in the previous iteration. The iterations stop when the same number of Λ^0's is found in successive iterations. Using these criteria, we find a sample of 413 ± 32(statistical) ± 31(systematic) Λ^0's+$\bar{\Lambda}^0$'s. In this sample the ratio of Λ^0's to $\bar{\Lambda}^0$'s is $1.24 \pm 0.19 \pm 0.18$. Figure (5-1) shows the invariant mass of $p\pi^-$ and $\bar{p}\pi^+$ pairs after the scaled background has been subtracted.

The numbers above include Λ^0's from decays of Ξ's and Σ^0's as well as prompt Λ^0's. Because of our event vertex resolution, it is impossible to separate

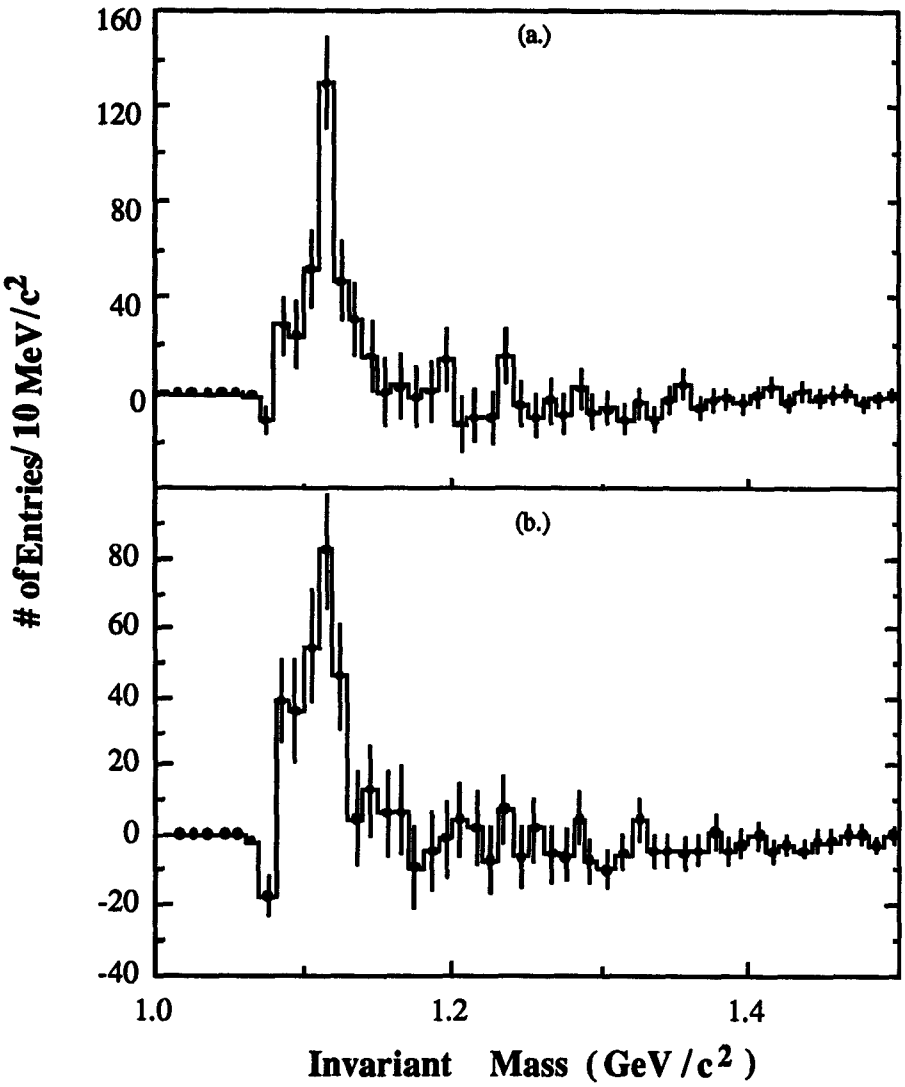

Figure 5-1. Invariant Mass plots after background subtraction for (a.)$p\pi^-$ pairs and (b.)$\bar{p}\pi^+$ pairs.

prompt Λ^0's from those which originate in decays of heavier hyperons. This was studied using Monte Carlo generated Ξ's. (Since Σ^0's decay within a very short time ($\tau c=2.2x10^{-9}$ cm), separating Σ^0's is not possible in any experiment). As discussed in the last chapter, the cut on the difference between the z intercept of a Λ candidate and the z position of the event vertex was $\Delta z= \pm 12$ cm. Figure (5-2) shows this difference for Λ^0's originating in the decay of Ξ's. The Ξ's were generated by the UA5 Monte Carlo (Alner et al. 1987b), allowed to decay, sent through our detector simulation (which generates an event vertex with the resolution of our detector) and sent through the Λ analysis program. In figure (5-2b), the event vertex resolution is not included, so this is the actual z-distance, at the beamline, of the Λ^0 track from the event vertex. While in figure (5-2a), the experimental event vertex resolution has been included. As shown in the figures, Δz is dominated by the event vertex resolution and it is impossible to separate prompt Λ^0's from those originating in decays. In fact, the figures show that $\geq$98% of the Λ^0's originating in the decay of a Ξ survive this cut. Later we will attempt to determine the fraction of prompt Λ^0's using the combinatoric quark model.

To calculate the p_t spectrum of Λ^0's, the invariant mass of $p\pi^-$ and $\bar{p}\pi^+$ pairs was also plotted for Λ^0 candidates in six different transverse momentum ranges. The background was again generated using opposite sign $p\pi$ pairs from different events. The background for each transverse momentum range consisted of pairs of tracks which combine to form a neutral track with a transverse momentum in the given range. Table 5-1 shows the number of Λ^0's and $\bar{\Lambda}^0$'s found in each p_t range.

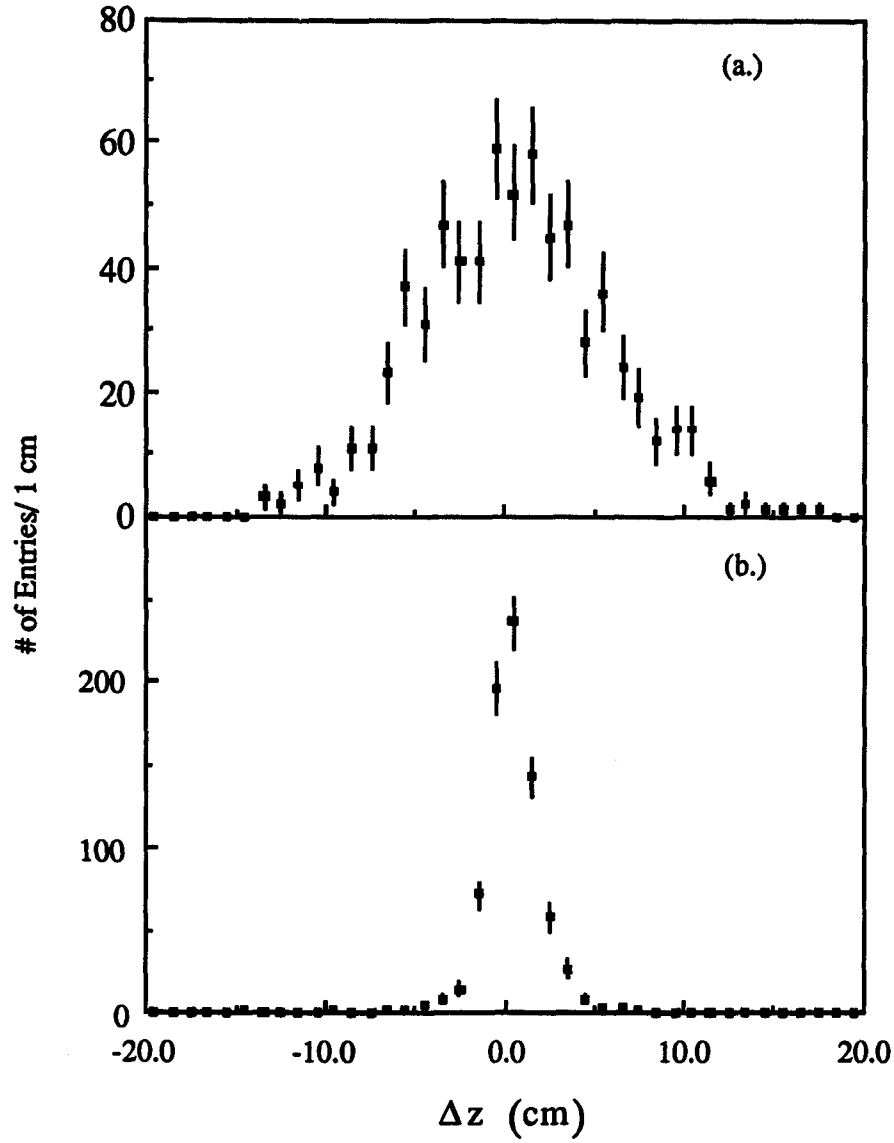

Figure 5-2. Difference, Δz, between the beam intercept of the reconstructed Λ^0 and the event vertex for Λ^0's from Ξ decay from a Monte Carlo (a) including vertex resolution, (b.) excluding vertex resolution.

Table 5-1.

Number of Λ's ($\bar{\Lambda}$'s) found in each p_t region.

p_t range (GeV/c)	(uncorrected)		(corrected)	
	# of Λ's	# of $\bar{\Lambda}$'s	# of Λ's	# of $\bar{\Lambda}$'s
$.5 < p_t < .75$	23 ± 7	20 ± 6	1513 ± 460	1316 ± 395
$.75 < p_t < 1.0$	53 ± 10	26 ± 8	1631 ± 308	800 ± 246
$1.0 < p_t < 1.5$	64 ± 13	62 ± 13	1103 ± 224	1069 ± 224
$1.5 < p_t < 2.0$	45 ± 11	32 ± 11	407 ± 100	290 ± 100
$2.0 < pt < 3.0$	45 ± 9	43 ± 9	273 ± 55	261 ± 55

These numbers were corrected for acceptance as described in the last chapter in order to calculate $1/(Np_t)\ dN/dp_t$. In figure (5-3a), this is plotted as a function of p_t for Λ^0's and $\bar{\Lambda}^0$'s separately and in figure (5-3b) $1/(Np_t)\ dN/dp_t$ is plotted versus p_t for Λ^0's plus $\bar{\Lambda}^0$'s. Both of these distributions were then fitted with the functional form $\exp(-bp_t)$. A value of 2.63 ± 0.20 was found for b from the fit to the

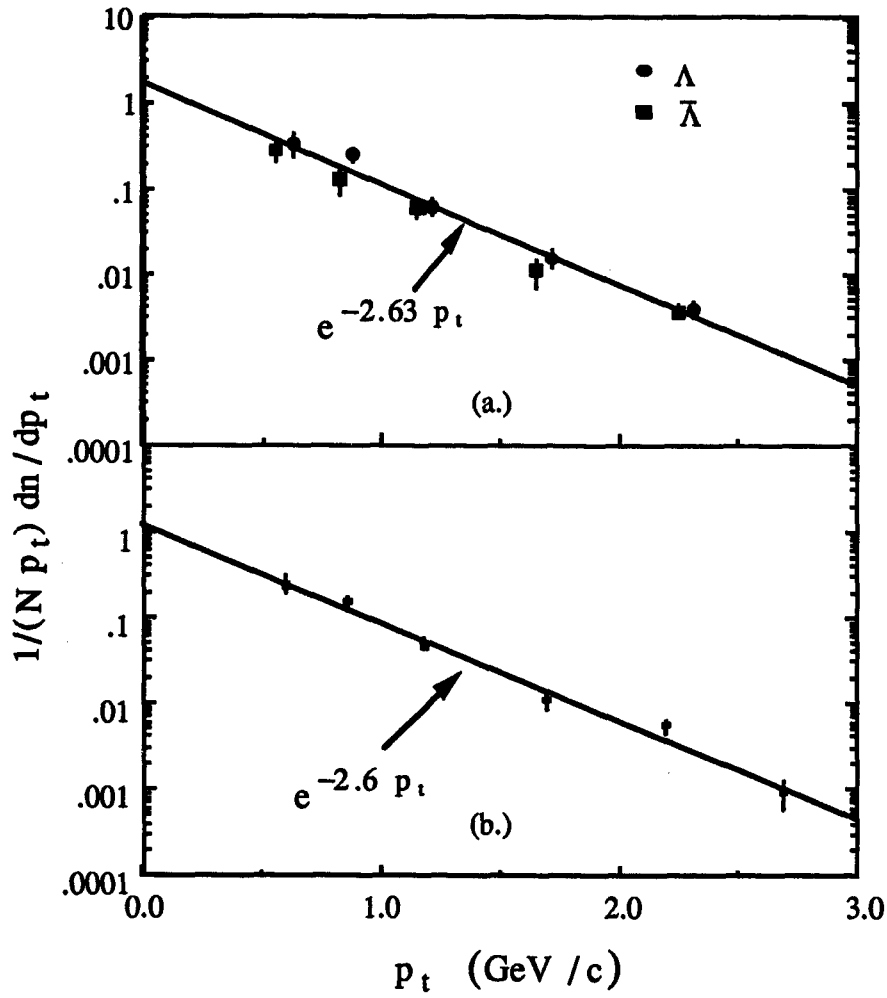

Figure 5-3. $1/(Np_t)\ dn/dp_t$ plotted for (a.) Λ^0's and $\overline{\Lambda}^0$'s separately and (b.) $\Lambda^0+\overline{\Lambda}^0$. Each line is from an exponential fit to all points on the particular plot.

distribution for Λ^0's and $\bar{\Lambda}^0$'s, giving an average transverse momentum of $\langle p_t \rangle = 0.76 \pm 0.06 \pm 0.07$ GeV/c assuming that the fit is good for all p_t. For the distribution for Λ^0's plus $\bar{\Lambda}^0$'s, a value of $b = 2.60 \pm 0.20$ was found, giving an average transverse momentum, $\langle p_t \rangle = 0.77 \pm 0.06 \pm 0.07$ GeV/c. In a later section, we will compare these results with results from lower energies.

Again, the first error is statistical and was obtained from the exponential fit to the p_t spectrum, while the second is systematic. The main contributions to the systematic error for $\langle p_t \rangle$ are uncertainties in the shape of the acceptance curve discussed in the previous chapter and uncertainties in the background subtraction. The shape of the acceptance curve is determined mainly by the geometrical acceptance. Other factors in the acceptance (such as particle identification, reconstruction efficiency and the cuts used in the analysis) are reasonably constant as functions of p_t and do not contribute significantly to the shape of the curve. It is estimated that the systematic error on $\langle p_t \rangle$, from the two factors mentioned above plus all other sources, is ≈15%.

Next the ratios $(\Lambda^0+\bar{\Lambda}^0)/N_{ac}$ and $(\Lambda^0+\bar{\Lambda}^0)/(p+\bar{p})$ were studied in the central rapidity region. First the ratio of Λ^0's plus $\bar{\Lambda}^0$'s to all charged tracks was studied as a function of p_t, for $0.5 < p_t < 3.0$ GeV/c. In order to obtain this ratio, the number of charged tracks was found for each of six transverse momentum ranges (the same ranges which were used to find the p_t spectrum of Λ 's), after imposing the cuts described in the last chapter. The number of acceptance corrected Λ's in each range was then divided by the number of charged tracks in the range. This ratio is plotted

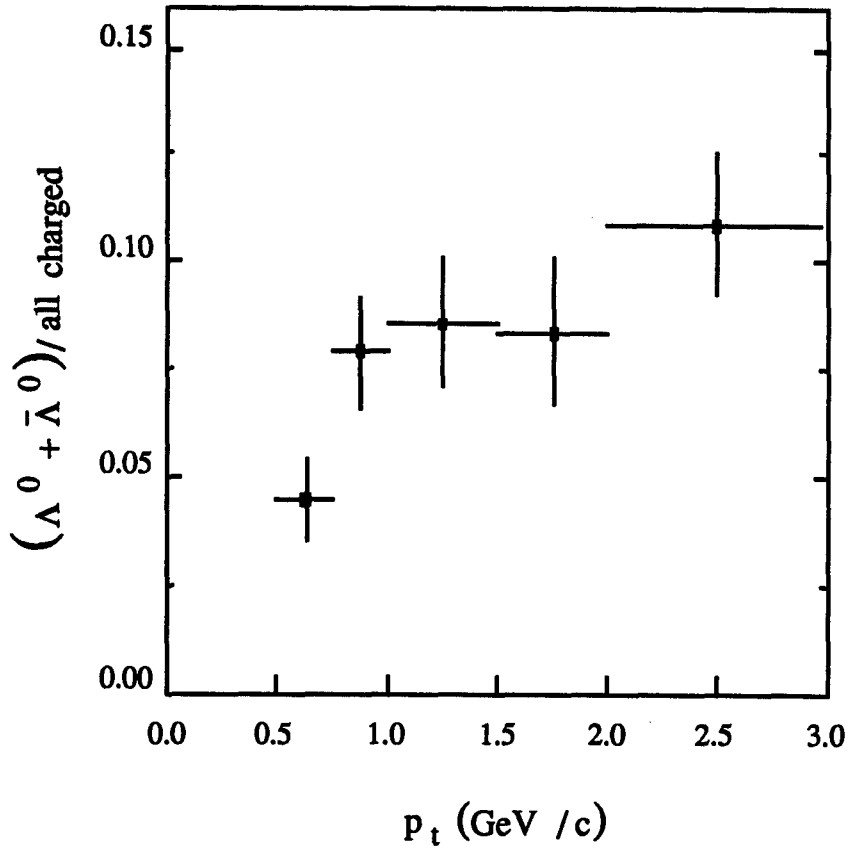

Figure 5-4. The ratio of $\Lambda^0+\bar{\Lambda}^0$ to all charged particles as a function of p_t. The errors are statistical only.

in figure (5-4). As seen in the figure, the ratio reaches a plateau at $p_t \approx 1.0$ GeV/c.

To obtain a ratio for all p_t, the exponential fit to the p_t spectrum of Λ^0's was integrated over all p_t. The number of charged tracks in the range $0.15<p_t<3.0$ GeV/c was obtained from the data. In order to find the number of charged particles with $p_t<0.15$ GeV/c, an exponential fit was performed over the p_t range $0.15<p_t<0.5$ GeV/c. This exponential was then integrated to find the number of unobserved charged tracks. After correcting for the number of unobserved Λ^0's and charged particles as described above, a value of $0.032 \pm 0.003 \pm 0.005$ is obtained for the ratio $(\Lambda^0+\bar{\Lambda}^0)/N_{ac}$ at $y \approx 0$.

The ratio $(\Lambda^0+\bar{\Lambda}^0)/N_{ac}$ was also studied as a function of the charged particle multiplicity. The acceptance corrections for this presented somewhat of a problem. Using a modified version of the Monte Carlo simulation that was described in the last chapter, a correction to the number of Λ's in each N_c bin can be generated. If the $<p_t>$ of the Λ's in the multiplicity range is known, then instead of generating Λ's with a fixed p_t, Λ's are generated with exponential p_t distribution ($\approx \exp(-2p_t/<p_t>)$). However, the relatively small sample of Λ^0's prevented an accurate measurement of the relationship between $<p_t>$ and the charged multiplicity. For this reason the Λ^0/N_{ac} ratio was studied using two different forms for $<p_t>_\Lambda$ versus N_c. The first form assumed that $<p_t>$ was flat versus N_c, so that each N_c bin was corrected by the same factor. Figure (5-5a) shows the ratio, Λ^0/N_{ac} plotted versus N_c using this assumption. The second form assumed that $<p_t>$ for Λ^0's had the same dependence on N_c as $<p_t>$ for protons

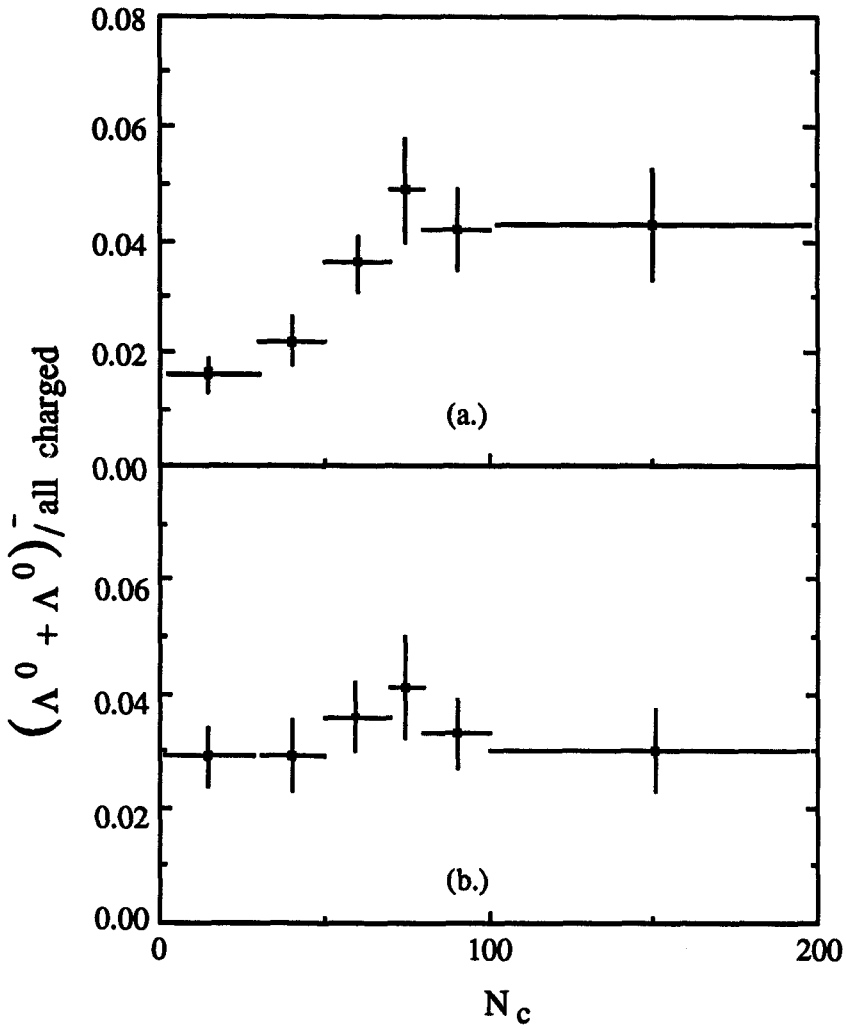

Figure 5-5. The ratio of $\Lambda^0+\bar{\Lambda}^0$ to all charged particles as a function of N_c assuming (a.) $\langle p_t \rangle$ is flat versus N_c, (b.) $\langle p_t \rangle$ behaves similarly for $\Lambda^0+\bar{\Lambda}^0$ and $\bar{p}$'s. Only statistical errors are shown.

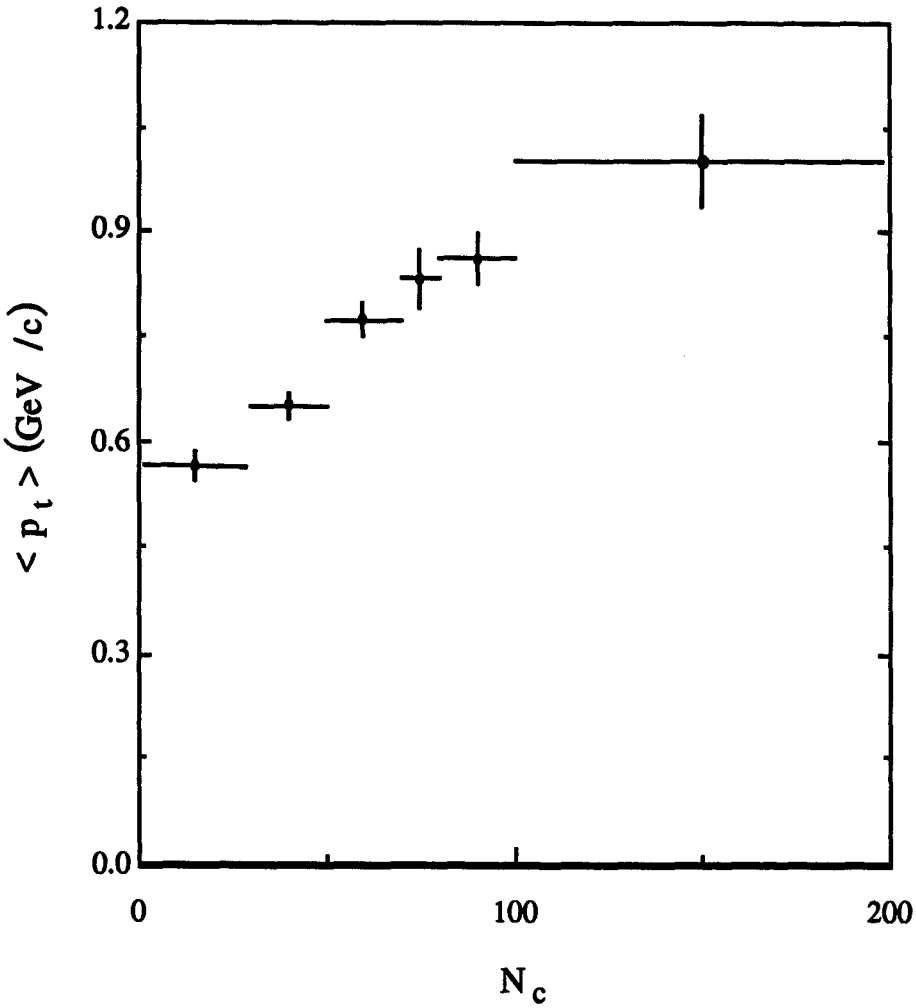

Figure 5-6. $<p_t>$ plotted versus N_c for $(p+\bar{p})$. This distribution was used as $<p_t>$ spectrum for $(\Lambda^0+\bar{\Lambda}^0)$ in order to calculate acceptance corrections as a function of N_c.

(Alexopoulos et al. 1989), which is shown in figure (5-6). Assuming this dependence, Λ^0/N_{ac} is calculated as a function of N_c and shown in figure (5-5b). It is likely that the $<p_t>$ of Λ^0's as a function of N_c is similar to that for protons.

The next ratio to be examined was $(\Lambda^0+\bar{\Lambda}^0)/(p+\bar{p})$. Since the antiproton track sample has fewer background tracks than the proton track sample (especially for low momentum (p<0.6 GeV/c) tracks) only antiprotons were used for this study. The excess of protons as compared to antiprotons was thought to arise mainly from secondary interactions of primary particles in the beam pipe. It was assumed that the same number of protons were present as antiprotons. So, the ratio which was actually studied was $(\Lambda^0+\bar{\Lambda}^0)/(2 \times \bar{p})$. Antiprotons were identified from their time of flight and momentum. In order to get a clean sample of antiprotons for this ratio the cuts for identifying an antiproton were more severe than those used when searching for Λ^0's. Antiproton candidates were required to cross the beamline within 10 cm in z of the event vertex as determined by the trigger hodoscope and within 10 cm of the y=0 beam position. A track was identified as a $\bar{p}$ if the mass was calculated to be greater than 0.76 GeV/c^2 and less than 1.5 GeV/c^2. Again only TOF1 was used for time of flight measurement. Since the separation between the kaon mass peak and the antiproton mass peak disappears for tracks with $p_t >$ 1.5 GeV/c using only TOF1, tracks with $p_t >$ 1.5 GeV/c were not considered. Because low momentum protons do not make it through the material in the detector including the aluminum beampipe, antiprotons with p_t<0.40 GeV/c were also cut. So, only antiprotons with 0.40 GeV/c < p_t < 1.5 GeV/c were identified for this study.

Acceptance corrections to the observed number of $\bar{p}$'s were generated using a Monte Carlo similar to the one used for Λ acceptance corrections. This time, $\bar{p}$'s with a given p_t are generated uniformly in azimuth and uniformly in the rapidity interval $-1.2<y<1.2$. Again the event vertex distribution from the data is simulated in the Monte Carlo. Antiprotons which are headed toward the spectrometer arm are subjected to a detailed Monte Carlo which includes effects such as multiple scattering and nuclear interactions in the beam pipe, detector position resolution, particle identification efficiency and the resolution of the time of flight counters. The Monte Carlo generated $\bar{p}$'s are then treated the same as the data to obtain the number that are identified as $\bar{p}$'s. The acceptance corrections for $\bar{p}$'s, like those for Λ's, are then obtained relative to the π acceptance. Figure (5-7) shows the $\bar{p}$ acceptance relative to π acceptance.

Shown in figure (5-8) is the the ratio $(\Lambda^0+\bar{\Lambda}^0)/(2\times\bar{p})$ in the central region plotted versus p_t for the three p_t regions $0.5<p_t<0.75$ GeV/c, $0.75<p_t<1.0$ GeV/c and $1.0<p_t<1.5$ GeV/c. As can be seen in the figure, all three points are consistent with a constant value of approximately 0.48 for the ratio. This ratio was also studied as a function of N_c, using the same assumptions that were used for the ratio $(\Lambda^0+\bar{\Lambda}^0)/N_{ac}$. Figure (5-9a) shows $(\Lambda^0+\bar{\Lambda}^0)/(2\times\bar{p})$ plotted as a function of N_c for $\langle p_t\rangle$ assumed to have a flat distribution versus N_c for Λ^0's + $\bar{\Lambda}^0$'s. In figure (5-9b) this same ratio is plotted versus N_c under the assumption that the $\langle p_t\rangle$ distribution versus N_c for Λ^0's follows that of protons. For either $\langle p_t\rangle$ distribution, the average value of $(\Lambda^0+\bar{\Lambda}^0)/(2\times\bar{p})$ is $0.47\pm0.03\pm0.07$ at $y\approx0$.

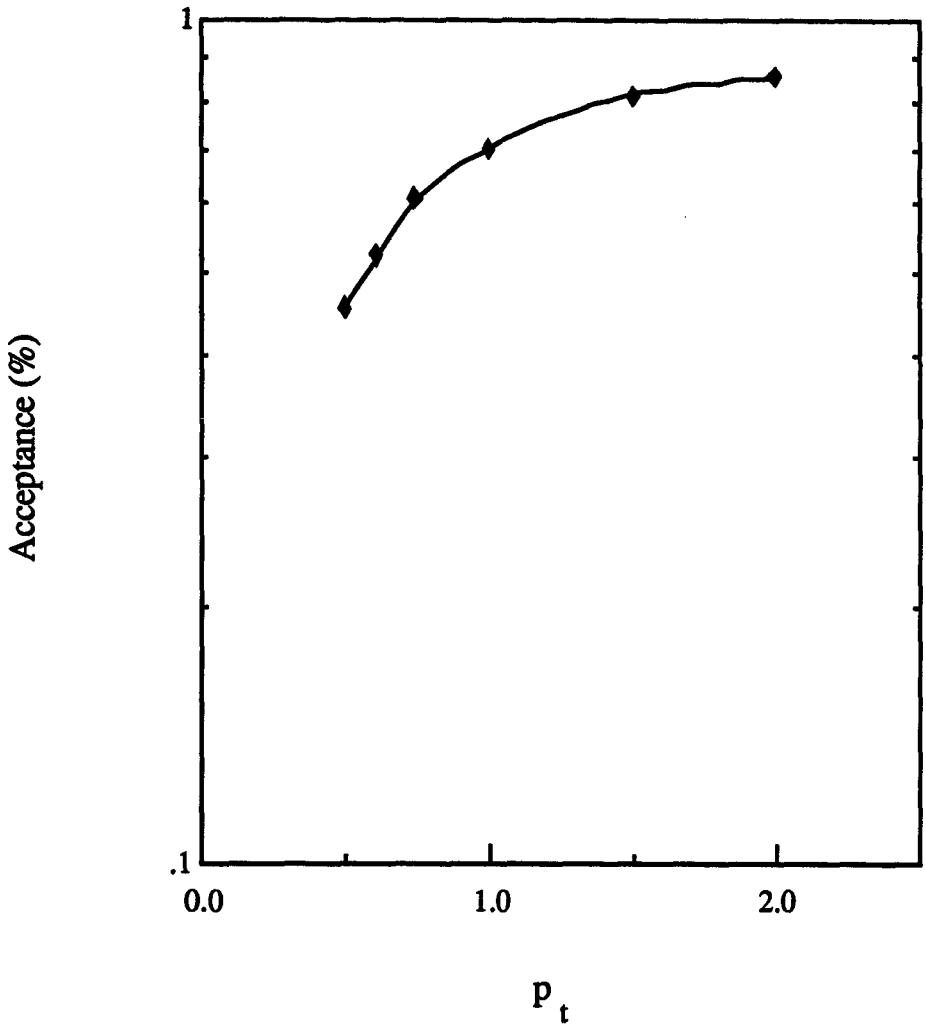

Figure 5-7. Antiproton acceptance relative to π acceptance as a function of p_t. (500,000 $\bar{p}$'s and 500,000 π's generated)

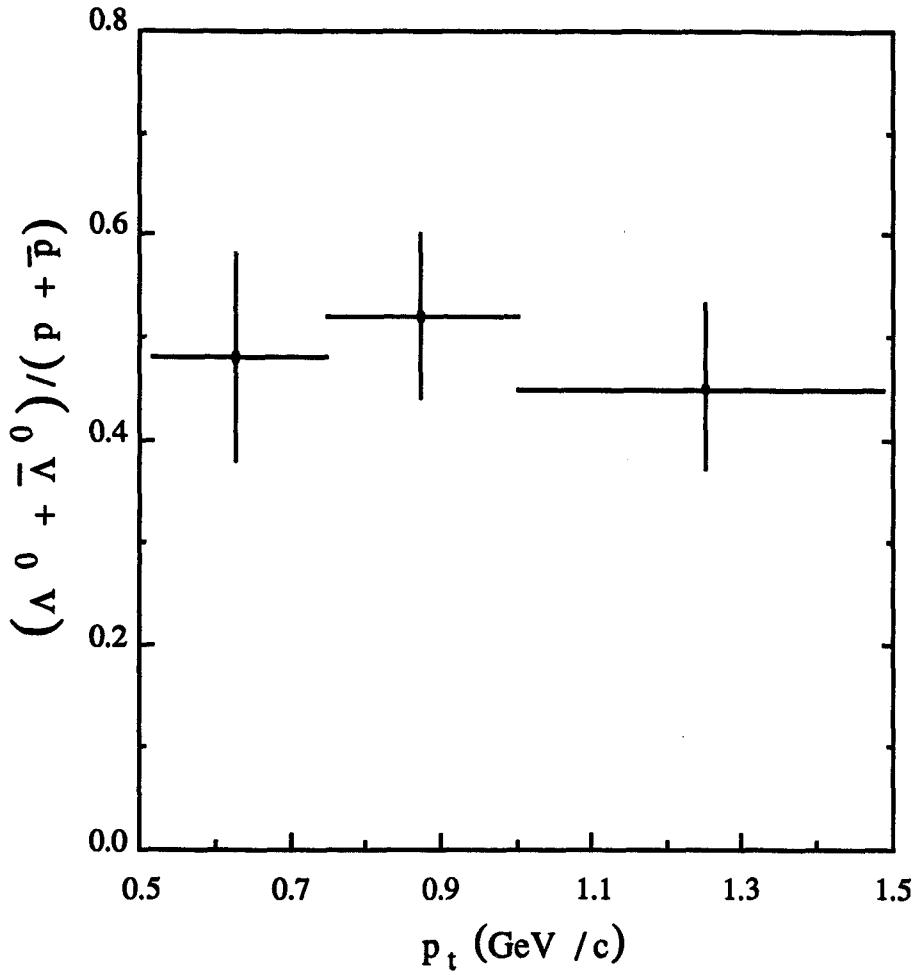

Figure 5-8. The ratio $(\Lambda^0+\bar{\Lambda}^0)/(p+\bar{p})$ plotted as function of p_t for the range; $0.5<p_t<1.5$ GeV/c. The error bars are statistical only.

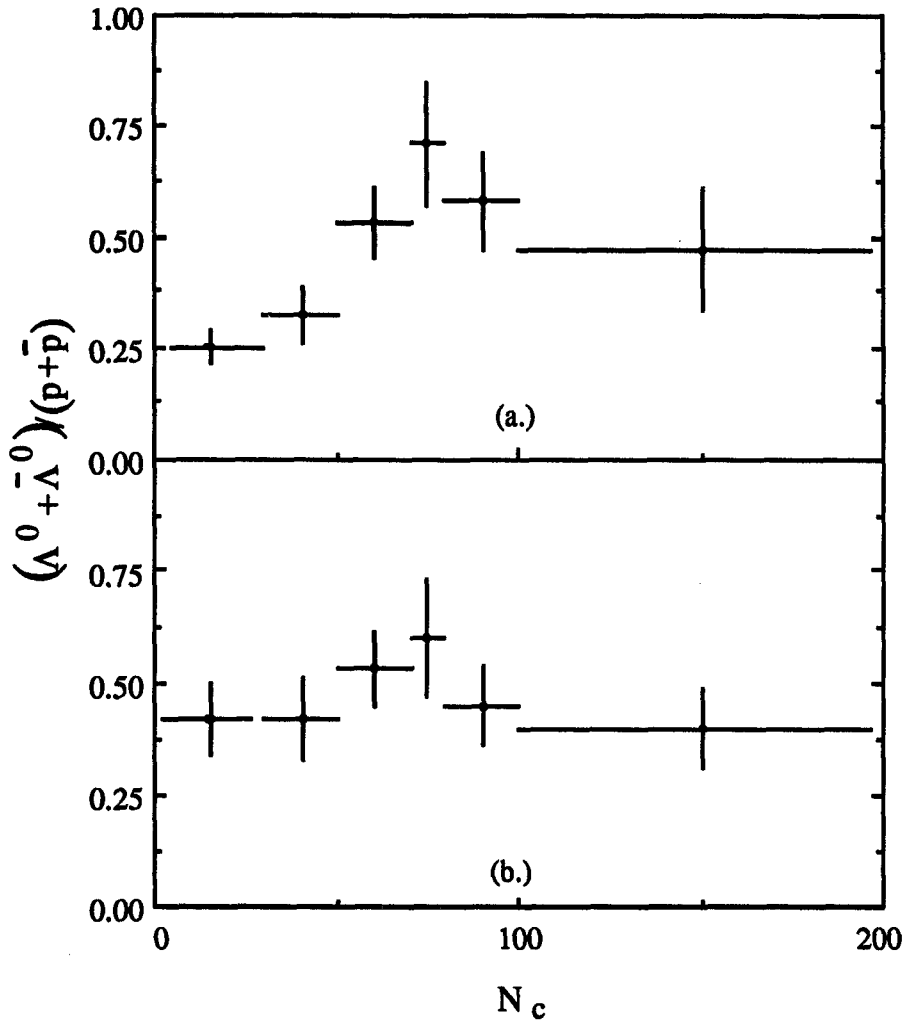

Figure 5-9. The ratio $(\Lambda^0+\bar{\Lambda}^0)/(p+\bar{p})$ plotted as a function of N_c assuming (a.)the $<p_t>$ for Λ's is flat versus N_c and (b.)the $<p_t>$ for Λ's is similar to the $<p_t>$ for protons versus N_c. Error bars represent statistical errors only.

II. Comparison with Lower Energy Results

The Tevatron collider has provided a higher energy than previously possible under laboratory conditions. We now turn to a comparison of the results obtained at 1.8 TeV and presented in the previous section to results of $p\bar{p}$ and pp experiments conducted at lower energies. In figure (5-10), the $<p_t>$ of Λ^0's+$\bar{\Lambda}^0$'s is plotted as a function of $\sqrt{s}$. As shown in the figure, the $<p_t>$ for Λ^0's+$\bar{\Lambda}^0$'s is approximately 24% higher than in $p\bar{p}$ collisions at the CERN SPS's 540 GeV energy (Alner et al. 1987) and about 55% higher than in proton-proton collisions at the CERN ISR's energies (Drijard et al. 1982). The $<p_t>$ of all charged particles increases by about 25% over the same energy range (Arnison et al. 1982). As will be discussed later, the contribution to the $<p_t>$ of Λ^0's due to Ξ decay is expected to be small.

The ratios quoted thus far have included Λ^0's from the decay of Σ^0's, Ξ's and Ω's. In order to compare these numbers to the ratios obtained at lower energies, we used the combinatoric quark model for multiparticle reactions (Anisovich and Shekhter, 1972) to estimate the contamination due to decays of these particles.

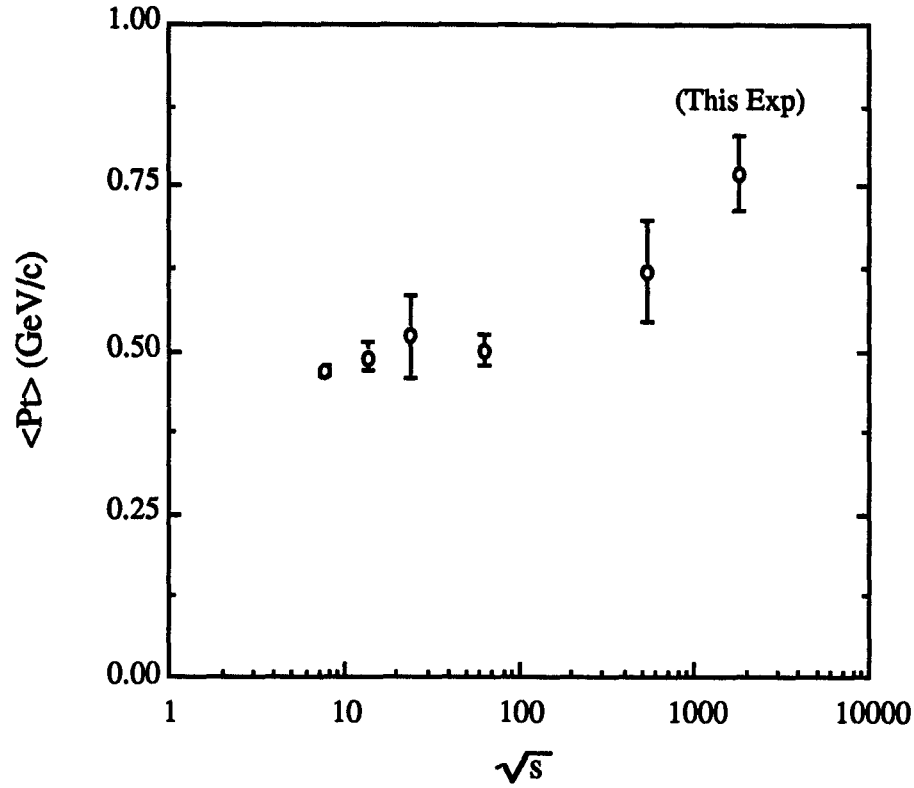

Figure 5-10. The $<p_t>$ for $(\Lambda^0+\bar{\Lambda}^0)$ as a function of $\sqrt{s}$ in pp and $\bar{p}p$ collisions. (Alner et al. 1987; Drijard et al. 1982; Poiret et al. 1981; Raja et al. 1977; Sheng et al. 1975)

This model provides a method to predict relative particle ratios in hadronic interactions. It involves no assumptions about the dynamics of the interaction; the particle ratios depend solely on which quarks, involved and produced in the interaction, combine to form the hadrons. According to the combinatoric quark model, the hadronic collision process produces a cloud of quarks and antiquarks. The probability for production of either light quark flavor (u,d) is the same, while production of strange quarks is suppressed by a factor of λ. Spectator quarks (antiquarks) and quarks (antiquarks) produced in the collision then bind into hadrons, mainly mesons of the SU(3) 36-plet and baryons (antibaryons) belonging to the SU(3) 56-plet. In the central rapidity region, where the particles are composed only of quarks produced in the collision, the distribution of particles is independent of the incident particles. For any quark (antiquark), the probabilities that it will combine with quark or an antiquark are the same. If a $q\bar{q}$ occurs a meson is formed, a qq pair combining with another quark results in a baryon and a qq pair combining with an antiquark results in a meson and a free quark. The probability for the production of any hadron is found through combinatoric calculus, leading to the result that meson production is six times more likely than baryon production. The production probability of individual hadrons is proportional to the number of spin states of the hadron.

Stable particles are produced in two ways; they may be produced directly or through the production and decay of shortlived resonances. Table 5-2 gives the relative multiplicities (in arbitrary units) of different stable particles after resonance decay.

The Λ/p ratio can be used to find the strangeness suppression factor (λ) by

Table 5-2

Relative production ratios of stable particles in the central region after resonance decay; $\kappa=(4+4\lambda+\lambda^2)/(5+5\lambda+3\lambda^2+\lambda^3)$ (Anisovich and Kobrinsky, 1974)

Particle	Relative Probability
$\pi^+\pi^-$	$31 + 12\lambda + 3\lambda^2 + \kappa(\frac{16}{3} + 4\lambda + \frac{8}{3}\lambda^2)$
π^0	$34 + 12\lambda + 3\lambda^2 + \kappa(\frac{16}{3} + 4\lambda + \frac{8}{3}\lambda^2)$
K^+K^-	$12\lambda + 4\lambda^2$
$K^0\bar{K}^0$	$12\lambda + 3\lambda^2$
$p\,n\,\bar{p}\,\bar{n}$	5κ
$\Lambda\,\bar{\Lambda}$	$8\lambda\kappa$
$\Sigma^+\Sigma^-\bar{\Sigma}^+\bar{\Sigma}^-$	$\lambda\kappa$
$\Xi^0\Xi^-\bar{\Xi}^0\bar{\Xi}^-$	$3\lambda^2\kappa$
$\Omega^-\bar{\Omega}^+$	$3\lambda^3\kappa$

counting all the Λ^0's and all the protons this model predicts.

$$\frac{\Lambda_{all}}{p_{all}} = \frac{\Lambda_{pr} + \Lambda_{\Xi} + \Lambda_{\Omega}}{p_{pr} + p_{\Lambda} + p_{\Sigma} + p_{\Xi} + p_{\Omega}} = \frac{8\lambda + 6\lambda^2 + 3\lambda^3}{5 + (.64)8\lambda + (.51)\lambda + (.64)6\lambda^2 + (.64)3\lambda^3}$$

where Λ_{pr} is the number of prompt Λ's, p_{pr} is the number of prompt p's and Λ_i (p_i) is the contribution to the number of Λ's (p's) from particle type i. The numbers in parentheses take into account branching ratios.

For our ratio of all Λ^0's to all protons of 0.47 we obtain a value of λ=0.34 ± 0.05 in agreement with the value of 0.38 ± 0.06 found from UA5 data (Müller, 1983). Figure (5-11) shows λ plotted as a function of the center of mass energy. As a function of energy, λ seems to increase slowly.

For this model the ratio $(\Xi^0+\Xi^-)/\Lambda_{pr}$ is $6\lambda/8$ and using the value of λ found from Λ/proton in the previous section we obtain $(\Xi^0+\Xi^-)/\Lambda_{pr}$=0.25. This ratio was used to remove Λ's from Ξ decay from the sample. Since Σ^0's were included (due to the Σ^0's short decay length) in the Λ^0 sample at lower energies, they are included in our corrected sample as well.

The UA5 event generator was used to extrapolate our numbers, which are corrected (using the method discussed in the previous chapter) for -1.2<y<2.0, to all y. The corrected (i.e., after removing Ξ's and extrapolating to all y) $(\Lambda^0+\bar{\Lambda}^0)$ to N_{ac} ratio of 0.026 ± 0.002 ± 0.004 at 1.8 TeV can be compared to the value of 0.019 ± 0.004 (G. J. Alner et al. 1987) at 540 GeV (SPS) and 0.009 ± 0.001 (K. Alpgard et al. 1982) at 53 GeV (ISR). There is a clear increase in this ratio as a function of $\sqrt{s}$.

The $(\Lambda^0+\bar{\Lambda}^0)$/proton ratio from the first section was also extrapolated to all y after correcting for Λ^0's from decays. The corrected value was found to be 0.38 ± 0.03 ± 0.06. This can be compared to UA5's value of 0.366 ± 0.085 at 540 GeV (G. J. Alner et al. 1987a) and 0.33 ± 0.02 at 53 GeV (K. Alpgard et al. 1982). Unlike the ratio Λ/N_{ac}, there is no increase seen in the ratio $(\Lambda^0+\bar{\Lambda}^0)$/proton as a function of $\sqrt{s}$.

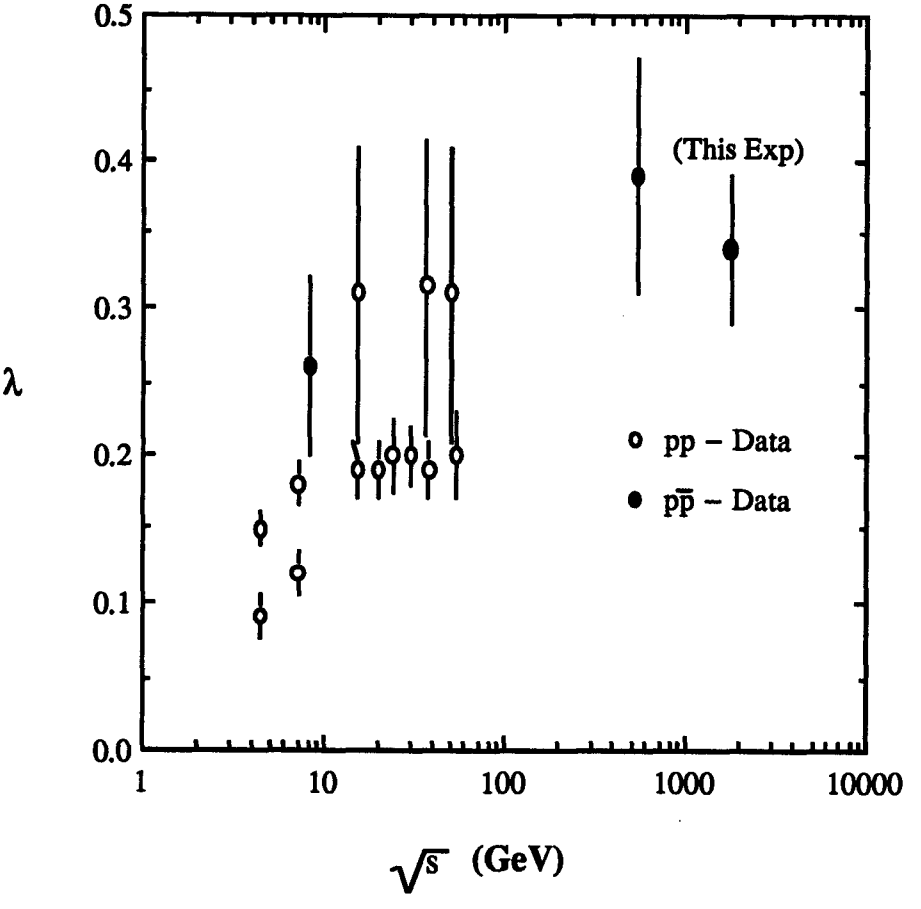

Figure 5-11. The strangeness suppression factor λ a function of center of mass energy in pp and $p\bar{p}$ interactions. (Müller 1983)

III. Comparison With the UA5 Monte Carlo Event Generator

The UA5 Monte Carlo event generator program (Alner et al. 1987b) was used for various purposes in this analysis. As mentioned in the last section it was used to extrapolate from the limited phase space of our detector to all phase space. Now we will use it for a comparison, as we contrast our results with the predictions of the UA5 Monte Carlo program in our limited rapidity range.

This Monte Carlo program is not based on any model of multiparticle production. It reproduces features of particle production at $\sqrt{s}$ =546 GeV using the principles of conservation of energy and momentum and the concepts of leading baryons and particle clustering. In the UA5 Monte Carlo, particles are produced in clusters. There are two leading clusters in each event, consisting of a nucleon or a Δ and its antiparticle. The rest of the particles in the event are generated in a varying number of central clusters. For each cluster, baryon number and strangeness are conserved. Each cluster contains about 2 charged particles on average. The Monte

Carlo was tuned to reproduce the multiplicity distribution, particle composition and other features of $\sqrt{s}$ =546 GeV $p\bar{p}$ interactions. Then, using results from lower energies, fits were performed to include the energy dependence of these quantities.

Using the UA5 Monte Carlo program we generated 500,000 $p\bar{p}$ events with a center of mass energy of 1800 GeV. The version of the UA5 Monte Carlo which was used had been slightly modified. The original version predicted a ratio of Ξ's to Λ's (not from Ξ's) of 0.52. Since this number is so much higher than any similar measurement or model prediction and because this number is based on a small sample of Ξ's, we used the prediction of the combinatoric quark model for this ratio. Therefore, the UA5 Monte Carlo was modified to give a value of 0.25 for this ratio. The Λ^0's, $\bar{\Lambda}^0$'s and the Ξ's from the Monte Carlo $p\bar{p}$ events were written to a file for analysis. The Ξ's were then allowed to decay and the Λ^0's, both from the Ξ's and from the original events, were then sent through our detector simulation in the same manner discussed in the previous chapter. After correcting for differences in charged particle multiplicity distribution between the generated events and the data, and running the analysis program on the generated events, we find 462 ± 21 Λ^0's+$\bar{\Lambda}^0$'s from the Monte Carlo as compared to $413 \pm 32 \pm 31$ in the data.

Next the predictions of the UA5 Monte Carlo concerning $\langle p_t \rangle$ for Λ^0's were studied. From the Monte Carlo, $\langle p_t \rangle$ for all Λ^0's is 0.760 ± 0.002. This number can be directly compared to our previously stated result of $\langle p_t \rangle = 0.77 \pm 0.06 \pm 0.07$ for all Λ^0's. The Monte Carlo was then used to look at $\langle p_t \rangle$ for prompt Λ^0's and Λ^0's from Ξ's separately. It was predicted that for Λ^0's from Ξ's $\langle p_t \rangle = 0.972 \pm 0.006$. For prompt Λ^0's the predicted $\langle p_t \rangle$ was 0.729 ± 0.002.

We compared the ratio $(\Lambda^0+\bar{\Lambda}^0)/N_{ac}$ to the predictions of the UA5 Monte Carlo. Figure (5-11a) shows the previously plotted $(\Lambda^0+\bar{\Lambda}^0)/N_{ac}$ versus p_t. Figure (5-11b) shows $(\Lambda^0+\bar{\Lambda}^0)/N_{ac}$ versus N_c using the assumption of a flat $<p_t>_\Lambda$ distribution versus N_c and figure (5-11c) uses the assumption of a $<p_t>_\Lambda$ distribution versus N_c which is the same as that for the protons. In each of these figures, the curve is from the UA5 Monte Carlo and represents the predicted ratio using all Λ^0's. Using Λ^0's which are not from Ξ's, the Monte Carlo predicts an average of 0.023 ± 0.002 for the ratio $(\Lambda^0+\bar{\Lambda}^0)/N_{ac}$. This can be compared to our corrected value of $0.027 \pm 0.002 \pm 0.004$.

Finally we compared the predictions of the Monte Carlo to our data for the ratio $(\Lambda^0+\bar{\Lambda}^0)/(p+\bar{p})$. Figure (5-12a) shows the ratio $(\Lambda^0+\bar{\Lambda}^0)/(p+\bar{p})$ versus p_t. In figure (5-12b), $(\Lambda^0+\bar{\Lambda}^0)/(p+\bar{p})$ versus N_c is plotted assuming the flat distribution for $<p_t>_\Lambda$ versus N_c. Figure (5-12c) shows the same plot assuming the $<p_t>_\Lambda$ versus N_c distribution which is similar to that for protons. In each of these plots, the predictions of the Monte Carlo for all Λ^0's are represented by the solid lines. To compare to our value of $0.38 \pm 0.03 \pm 0.06$ for Λ^0's not from Ξ decay, we obtain a prediction of 0.36 ± 0.005 from the event generator.

As shown from figures (5-11c) and (5-12c), the best agreement between the data and the Monte Carlo is obtained when the $<p_t>_\Lambda$ versus N_c is assumed to behave similarly to the $<p_t>$ for protons. However, as was mentioned previously the UA5 Monte Carlo is not based on any model of multiparticle production. In fact, one of the assumptions of the Monte Carlo is that the particle ratios are indepen-

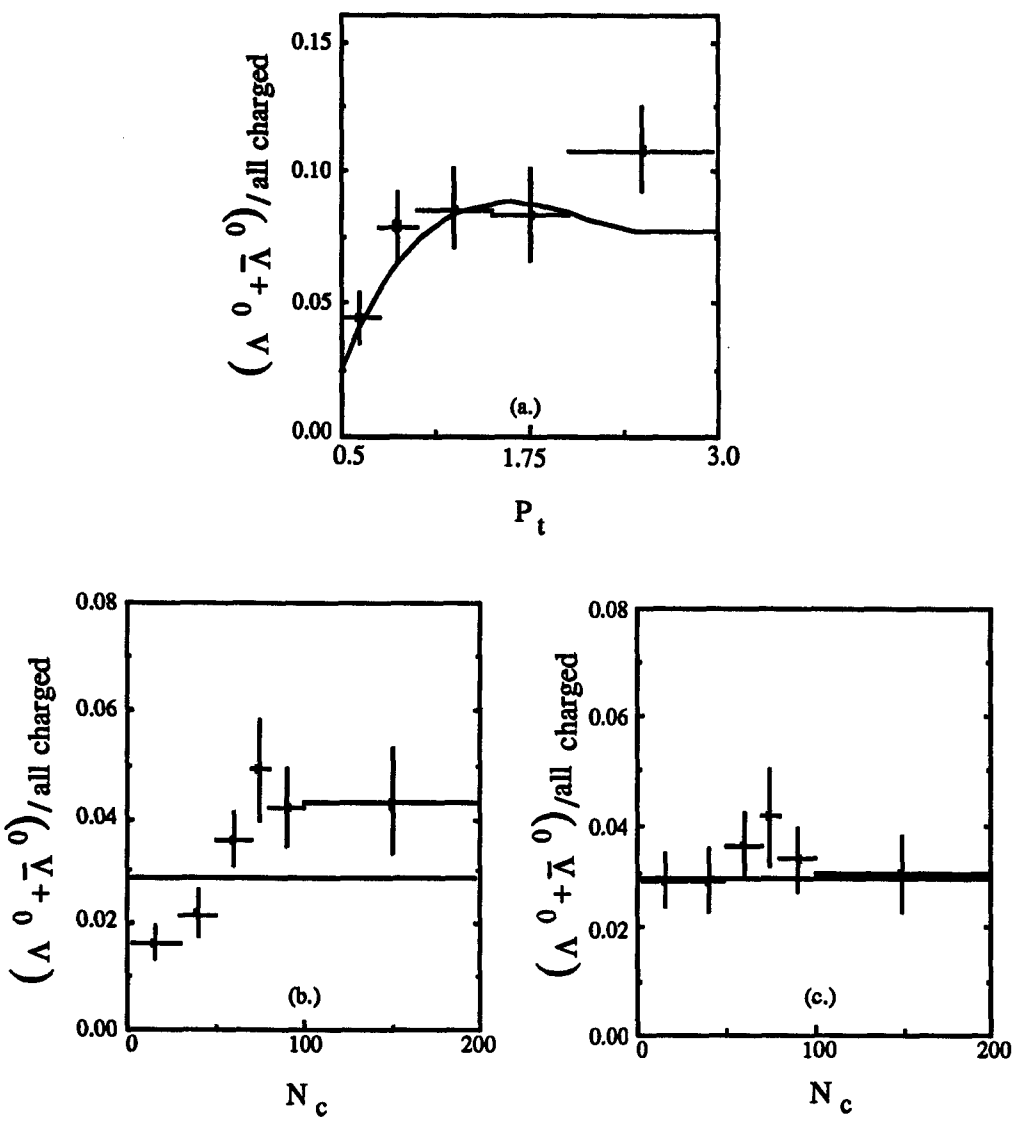

Figure 5-12. (a.) $(\Lambda^0+\bar{\Lambda}^0)$/all charged versus p_t. Also, $(\Lambda^0+\bar{\Lambda}^0)$/all charged versus N_c; using (b.) a flat $\langle p_t \rangle$ versus N_c spectrum for Λ^0's (c.) the $\bar{p}$ $\langle p_t \rangle$ versus N_c spectrum for Λ^0's . The solid line in each plot is a fit to the UA5 Monte Carlo (Alner et al. 1987b) prediction.

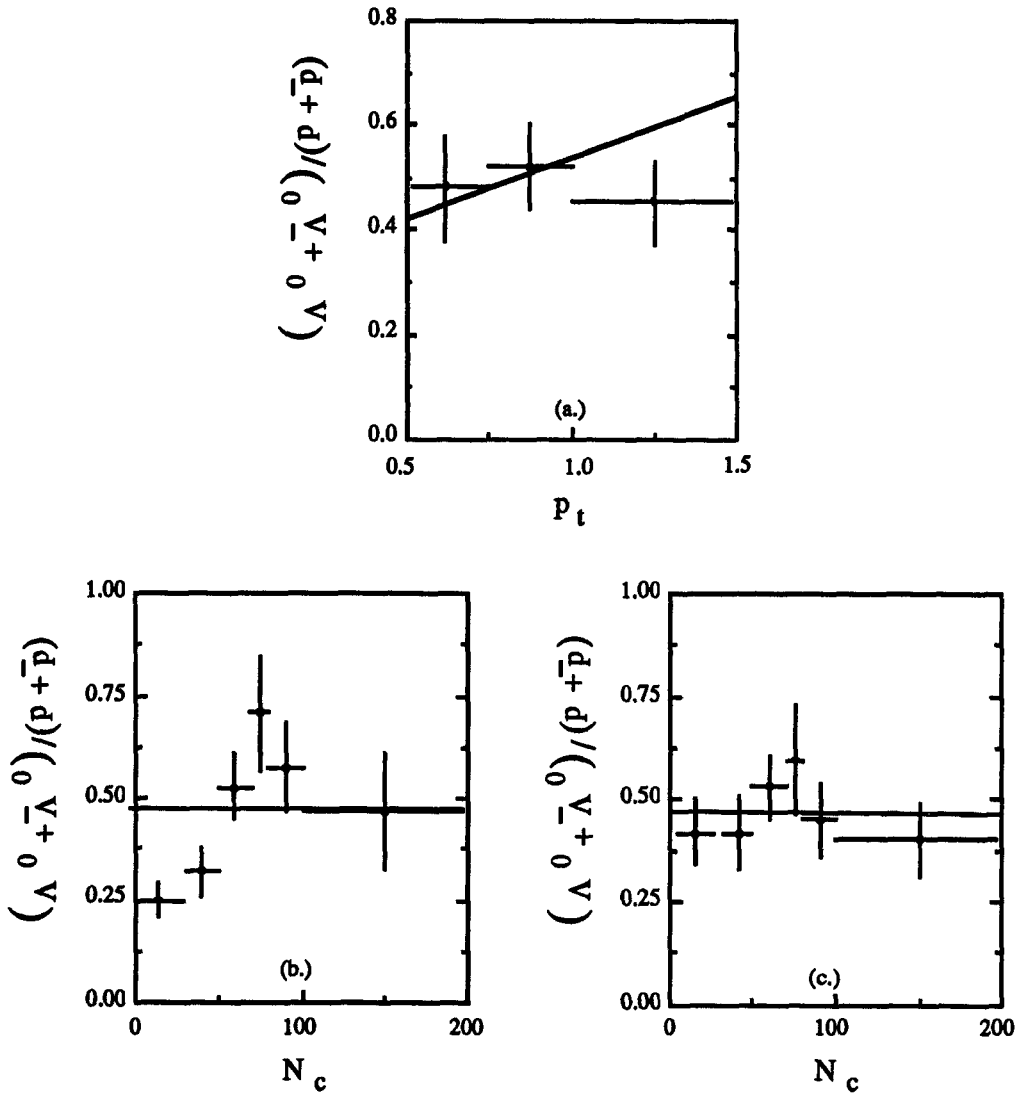

Figure 5-13. (a.) $(\Lambda^0+\bar{\Lambda}^0)/(p+\bar{p})$ versus p_t. Also, $(\Lambda^0+\bar{\Lambda}^0)/(p+\bar{p})$ versus N_c; using (b.) a flat $<p_t>$ versus N_c spectrum for Λ^0's (c.) the $\bar{p}$ $<p_t>$ versus N_c spectrum for Λ^0's . The solid line in each plot is a fit to the UA5 Monte Carlo (Alner et al. 1987b) prediction.

dent of N_c. So the flatness of the predictions for the ratios versus N_c is one of the inputs of the event generator and not a consequence of a model. In general, our data is consistent with the results of the UA5 Monte Carlo.

Chapter 6

Conclusions

This dissertation reports on results of experiment E735 on Λ and $\bar{\Lambda}$ production at center of mass energy, $\sqrt{s}$ =1.8 TeV. This experiment was carried out at the C0 intersection region of the Fermi National Laboratory's Tevatron $p\bar{p}$ collider. E735 used a magnetic spectrometer arm to sample the momentum spectra of charged particles, time of flight counters to identify these charged particles, and

hodoscope arrays to measure the charged particle multiplicity. The experiment was designed to search for signatures of quark-gluon plasma in the central rapidity region by looking at low transverse momentum particles.

Quark-gluon plasma is a localized volume of deconfined quarks and gluons which is thought to form in hadron-hadron or nucleus-nucleus collisions at sufficiently high energy densities. Since this state is supposed to be unstable, it must be detected through measurements of its decay products. One of the proposed signatures of plasma formation is enhanced strangeness production caused by increased interactions between gluon pairs.

In order to identify lambdas, we calculated an invariant mass using a mass identified proton or antiproton together with oppositely charged π's. To summarize, we found a sample of $413 \pm 32 \pm 31$ Λ's + $\bar{\Lambda}$'s, and found that the ratio of Λ's to $\bar{\Lambda}$'s was $1.24 \pm 0.19 \pm 0.18$.

After separating the Λ's and $\bar{\Lambda}$'s into transverse momentum bins, we plotted $1/N/p_t \; dn/dp_t$ for Λ's and $\bar{\Lambda}$'s separately and for the sum. We then fit an exponential of the form $\exp(-bp_t)$ to the data in order to calculate the average transverse momentum. We found a value of 2.6 ± 0.20 for b, which gives an average transverse momentum of $0.77 \pm 0.06 \pm 0.08$ GeV/c. This value of $\langle p_t \rangle$ is 24% higher than the value found at $\sqrt{s}$ =540 GeV and 55% higher than found at $\sqrt{s}$ =53 GeV. Over the same energy range (53 GeV to 1800 GeV), the $\langle p_t \rangle$ of all charged particles was found to increase by about 25%.

The value of the ratio $(\Lambda + \bar{\Lambda})$/all charged as a function of p_t reaches a plateau at $p_t \approx 1.0$ GeV/c. For all p_t, we find a value of $0.032 \pm 0.003 \pm 0.005$. When

corrected for Λ's from Ξ decays and extrapolated to all phase space, this ratio becomes $0.026 \pm 0.002 \pm 0.004$ as compared to 0.019 ± 0.004 at $\sqrt{s}$ =540 GeV and 0.009 ± 0.001 at $\sqrt{s}$ =53 GeV. We also studied this ratio as function of the charged particle multiplicity for two different assumptions about $<p_t>$ versus N_c for Λ's. Reasonable agreement between our data and the results from the UA5 Monte Carlo was found for the assumption that $<p_t>$ versus N_c for Λ's resembles $<p_t>$ versus N_c for protons. (In our rapidity range, again corrected for Λ's from Ξ decays, this Monte Carlo gives 0.023 ± 0.002 as compared to our value of $0.027 \pm 0.002 \pm 0.004$.)

Using the production ratios, we have studied the strangeness suppression factor (λ) for the data. The strangeness factor is from the combinatoric quark model and can be used to predict production ratios for stable particles. From our data, we find a value, λ=0.34 ± 0.05 which is in agreement with the UA5 value of λ=0.38 ± 0.06 and with the values found at lower energies.

Finally, we studied the ratio $(\Lambda + \bar{\Lambda})/(p+\bar{p})$. For this ratio, we obtain a value of $0.47 \pm 0.03 \pm 0.07$. Again correcting the data for cascade decay and extrapolating to all phase space gives a value of $0.38 \pm 0.03 \pm 0.06$ in reasonable agreement with the value of 0.366 ± 0.085 found at $\sqrt{s}$ =540 GeV and with the value of 0.33 ± 0.02 found at $\sqrt{s}$ =53 GeV . Once again, the assumption that $<p_t>$ versus N_c for Λ's is similar to that for protons gives agreement between the data and the UA5 Monte Carlo for $(\Lambda + \bar{\Lambda})/(p+\bar{p})$ versus N_c.

Now we shall examine our results in the context of QGP production. We do

see an increase in the production of Λ's as compared to all charged particles. However, we see no increase in the production of Λ's as compared to protons. Also, the increase in the ratio of Λ's to all charged particles is consistent with the predictions of the UA5 Monte Carlo which does not require the production of QGP. This is not to say that quark-gluon plasma is not produced. The theoretical understanding of the production, evolution and especially the decay of the quark-gluon plasma is not sufficient to determine if plasma production did or did not occur based on this one signature. Only by studying several possible signatures can that determination be made. However, in the production of Λ's at $\sqrt{s}$ =1.8 TeV, we find no clear evidence of quark-gluon plasma formation.

APPENDIX A

The C0 Coordinate System

The coordinate system for E735 is based on the direction the proton bunches travel in the Tevatron. The +z direction for E735 is defined as being in the direction of travel, at C0, of the proton bunches in the Tevatron. The +x direction is defined as being horizontally out from the beam pipe, toward the spectrometer, or, in other words, towards the center of the Tevatron ring. This leaves the +y direction to be defined as vertically up. The term "downstream" refers to the direction that the protons travel at C0, the +z direction and, of course, the term

"upstream" is opposite to that direction, the -z direction . The origin in C0 coordinates is defined as being the (nominal) average collision point for the C0 interaction region. In this coordinate system, the polar and azimuthal angles, theta and phi, are defined with z being the polar axis and $\varphi=0^{\circ}$ being along the x axis. Figure (A-1) shows the E735 detector layout with these conventions for the coordinate system labeled. In the figure, the +y direction is out of the page.

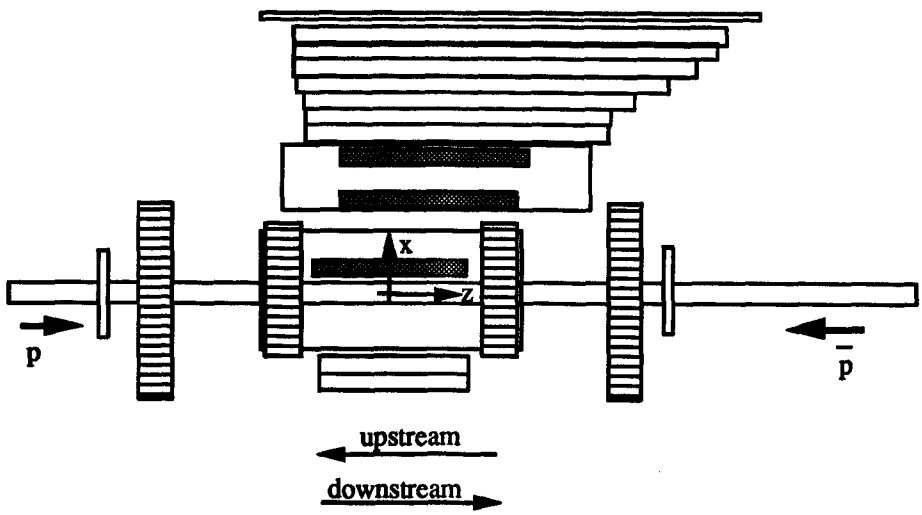

Figure A-1. Detector layout showing coordinate system (+y is out of the page) and direction terminology for E735. This system is based on the direction of the protons in the Tevatron.

Appendix B

The Cubic Spline Fit

When reconstructing good tracks, those which include hits in more than just the straw tube drift chambers, a cubic spline fit is used for the track. Only this type of track was used in this analysis, so we will now take a look at this fit. The cubic spline fit is continous and is also continous in the first and second derivatives. It is faster than Runge-Kutta and other step by step tracking methods, because it is a global fit which is consistent with a constant momentum and the magnetic field present (Wind, 1973).

Using a step by step method for a preliminary fit, an estimate of the momentum

of the particle and the coordinates of the hits associated with the track are obtained. This fit is also used to obtain estimates of the first derivatives at the hit positions. The second derivatives are obtained using the equations of motion of a charged particle in a magnetic field. For example, for the y component the equation is:

$$\frac{d^2y}{dx^2} = (\dot{z}B_x - \dot{x}B_z)/m$$

If we use:

$$\frac{dy}{dx} \equiv y' = \frac{\dot{y}}{\dot{x}} \quad \text{and} \quad \frac{d^2y}{dx^2} \equiv y'' = (\ddot{y}\,\dot{x} - \dot{y}\,\ddot{x})/\dot{x}^3,$$

and similar expressions for z' and z'', then the momentum can be written as:

$$p = m\dot{x}\left(1 + y'^2 + z'^2\right)^{1/2}$$

then the product of the momentum and the second derivitive, with respect to x, of the track can be written as:

$$py'' = \left(1 + y'^2 + z'^2\right)^{1/2}\left(\dot{x}(\dot{z}B_x - \dot{x}B_z) - \dot{y}(\dot{y}Bz - \dot{z}B_y)\right)/\dot{x}^2. \qquad \text{(B-1)}$$

Which, with a little bit of work becomes:

$$py'' = \left(1 + y'^2 + z'^2\right)^{1/2}\left(z'B_x + y'z'B_y - (1 + y'^2)B_z\right). \qquad \text{(B-2)}$$

Which is equation (4-1) and through the same procedure for z, equation (4-2) is obtained.

The second derivative, obtained in this manner is used to generate points on the track (and the first derivative at those points) in between the detector hits. Using these points, a least squares fit is preformed and from this the parameters of the fit, the y intercept, the y slope, the z intercept, the z slope and the momentum are obtained. This is an iterative process. The entire procedure is repeated using the new momentum and possibly deleting any bad hits associated with the track for four iterations or until the momentum changes by less than 5% between iterations.

References

Alexopoulos, T., *et al.*, Phys. Rev. Lett., **60**, 1622 (1988)

Alexopoulos, T., *et al.*, "Mass Identified Particle Yields in Antiproton-Proton Collisions at $\sqrt{s}$ =1.8 TeV", to be published in Phys. Rev. Lett.

Alner, G. J., *et al.*, Phys. Rep., **154**, 247 (1987a)

Alner, G. J., *et al.*, Nucl. Phys., **B294**, 445 (1987b)

Alpgard, K., et al., Phys. Lett., **115B**, 65 (1982)

Anishety, R., P. Koehler and L. McLerran, Phys. Rev. D, **22**, 2793 (1980)

Anisovich, V. V. and M. N. Kobrinsky, Phys. Lett., **52B**, 217 (1974)

Anisovich, V. V. and V. M. Shekhter, Nucl. Phys., **B55**, 455 (1972)

Arnison, G., *et al.*, Phys. Lett., **118B** 167 (1982)

Arnison, G., *et al.*, Phys. Lett., **122B** 103 (1983a)

Arnison, G., *et al.*, Phys. Lett., **126B** 398 (1983b)

Aubert, J. J., *et al.*, Phys. Rev. Lett., **33**, 1404 (1974)

Augustin, J. E., *et al.*, Phys. Rev. Lett., **33**, 1406 (1974)

Bagnaia, P., *et al.*, Phys. Lett., **129B**, 130 (1983)

Banerjee, S., *et al.*, Nucl. Instrum. and Methods, Phys. Res., Sect. A **269**, 121 (1988)

Banerjee, S., *et al.*, Phys. Rev. Lett., **62** 12 (1989)

Banner, M., *et al.*, Phys. Lett., **122B**, 476 (1983)

Barnes, W. S., *et al.*, Phys. Rev. Lett., **12**, 204, (1964)

Bartel, W., *et al.*, Phys. Lett., **28B**, 148 (1968)

Bjorken, J. D., Phys. Rev., **163**, 1767 (1967)

Bjorken, J. D., Phys. Rev. D, **27**, 140 (1983)

Cabibbo, N., Phys. Rev. Lett., **10**, 531 (1963)

CERN, "Geant3 Users Guide", CERN DD/EE/84-1 (1985)

Danos, Michael and Johann Rafelski, Phys. Rev. D, **27**, 671 (1983)

Dao, F. T., *et al.*, Phys. Rev. Lett. **30**, 1151 (1973)

Domokos, G. and J. I. Goldman, Phys. Rev D, **23**, 203 (1981)

Drijard, D., *et al.*, Zeitschrift fur Physik, **C12**, 217 (1982)

Engels, J., *et al.*, Phys. Lett., **101B**, 89, (1981a)

Engels, J., *et al.*, Phys. Lett., **102B**, 332, (1981b)

Feynman, R. P., Phys. Rev. Lett., **23**, 1415 (1969)

FNAL E735 Collaboration, Proceedings of the XVIIth Symposium on Multiparticle Dynamics, Seewinkel, Austria, 1986, ed. N. Markytan, W. Majoretto and J. MacNaughton, World Scientific, Singapore, p839 (1987)

Fowler, W. B. et al, Phys. Rev., **93**, 861 (1954)

Fowler, G. N. and R. M. Weiner, Phys. Lett., **70B**, 201 (1977)

Gell-Mann, M., Phys. Rev., **92**, 833 (1953)

Gell-Mann, M., Phys. Rev., **125**, 1067 (1962)

Gell-Mann, M., Phys. Lett., **8**, 214 (1964)

Glashow S. L., Nucl. Phys., **22**, 579 (1961)

Glashow, S. L., J. Iliopoulos and L. Maiani, Phys. Rev. D, **2**, 1285 (1970)

Greiner, W., P. Koch and J. Rafelski, Phys. Lett. **145B**, 142 (1984)

Halzen, F. and H. C. Liu, Phys. Rev. D, **25**, 1842 (1981)

Halzen, Francis and Alan D. Martin, Quarks & leptons: An introductory course in modern particle physics, John Wiley & Sons, New York, New York, 1984

Herb, S. W., *et al.*, Phys. Rev. Lett., **39**, 252 (1977)

Juricic, I., *et al.*, Phys. Rev. D, 39, **1**, (1989)

Kajante, K. and L. McLerran, Ann. Rev. Nucl. Part. Sci., **37**, 293 (1987)

Kajantie, K., C. Montontn and E. Pietarinen, Zeitschrift fur Physik, **C9**, 253 (1981)

Kapusta, J. and A. Mekjian, Phys. Rev. D, **33**, 1304 (1986)

Kobayashi M. and K. Maskawa, Prog. Theor. Phys., **49**, 282 (1972)

Koch P., B. Muller and J. Rafelski, Phys. Reports **142**, 162 (1986)

Kuti, J., J. Polonyi and K. Szlachanyi, Phys. Lett., **98B**, 199 (1981)

Lattes, C. M., *et al.*, Nature, **160**, 453 (1947)

Le Prince-Ringuet, L., and M. Lheritier, Compt. Rend., **219**, 618 (1944)

McLerran, L. and B. Svetitsky, Phys. Lett., **98B**, 199 (1981)

Montvay, I., and E. Pietarinen, Phys. Lett., **110B**, 148, (1982)

Müller, Thomas, Proceedings of the XIVth Symposium on Multiparticle Dynamics, Granlibakken, Lake Tahoe,California, USA, 1983, ed. P. Yager, and J. F. Gunion , World Scientific, Singapore, p528 (1984)

Ne'eman, Y., Nucl. Phys., **26**, 222 (1961)

Nishijima, K., Prog. Theor. Phys. **13**, 285 (1955)

Occhialini, G. P. S. and C. F. Powell, Nature, **159**, 186 (1947)

Oh, S., *et al.*, "Design and performance of straw tube drift chambers", to be published.

Pais, A., Phys. Rev., **86**, 663 (1952)

Perkins, D. H., Nature, **159**, 126, (1947)

Poiret, C., *et al.*,Zeitschrift fur Physik, **C11**, 1 (1981)

Rafelski, Johann and Berndt Muller, Phys. Rev. Lett., **48**, 1066 (1982)

Raja, R., *et al.*, Phys. Rev. D, **15**, 627, (1976)

Rochester, G. D. and C. C. Butler, Nature, **160**, 855 (1947)

Salam, A., Elementary particle theory (ed. N. Svartholm), Almquist and Wiksells, Stockholm, 1968

Sheng, A., *et al.*, Phys. Rev. D, **11**, 1733 (1975)

Weinberg, S., Phys. Rev. Lett., **19**, 1264 (1967)

Wind, H., Nucl. Instrum. and Methods, **115**, 431 (1973)

Wu, S. L., Phys. Rep., **107**, 59 (1984)

Zweig, G., CERN Report 8419/Th 412, 1964